Methods of targeting observations for the improvement of weather forecast skill

Thomas H. A. Frame

Departments of Mathematics/Meteorology

University of Reading

December 2006

’Declaration

I confirm that this is my own work and the use of all material from other sources has been properly and fully acknowledged’

Thomas H. A. Frame

Abstract

This thesis is a contribution to the subjects of midlatitude atmospheric dynamics and targeting observations for the improvement of weather forecasts. For the first time the full spectrum of singular vectors of the Eady model are considered. The importance and implications of the unshielding and modal unmasking mechanisms to the computed singular vectors are discussed. The computed singular vectors are used to analyse the vertical structure of the singular vector targeting function commonly used in observation targeting, in a vertical cross-section. Through comparison of this vertical cross-section to the dynamics of singular vectors, inferences about the scale and qualitative behaviour of the perturbations to which particular regions are 'sensitive' are made. In the final section of the thesis, a new targeting method is introduced. This new targeting method utilises a set of evolved singular vectors to approximate the background errors within the region identified by a set of targeted singular vectors as dynamically connected to the verification region. The two sets of singular vectors can then be used as a computationally inexpensive means of predicting the reduction of forecast error variance that will be obtained from a given deployment of observations. This method differs from previous targeting methods as it makes no use of stationary norms or Kalman filter theory. It allows for both a dynamically determined estimate of the initial condition errors and allows for the operational data assimilation to be taken into account. Another major difference between the new targeting method and existing methods, is that it explicitly predicts the reduction in forecast error variance as the difference between the forecast error variance with and without the targeted observations. This additional feature introduces the potential for the prediction of instances where adding observations is likely to lead to an *increase*

in the forecast error variance in the verification region.

Acknowledgements

First and foremost I would like to thank my supervisors Alan, Nancy and Andrew for their patience and support throughout the past few years, and for accepting my periodic absences. I would also like to thank my examiners for their helpful suggestions, and for not bringing my greatest fears to life. Further thanks go to everyone at the departments of mathematics and meteorology; in particular the DA and PWC groups for the chance to sound off on various subjects from time to time.

Special thanks goes to those who've shared their living and office space with me in Sherfield, Durley and 2u07 - too too many of you to name here - thank you! Thanks to my old friends from Gelligaer - Gareth, Tommy, Warren - who've always been able to find room for me - mostly in the pub.

To my family: Thank you for always being there for me throughout these past 28+ years.

To my beautiful wife Vivienne: Your infectious enthusiasm for life allows me to look at the simplest of things with a sense of wonder. Thank you for always being able to capture my full attention, and never knowing, caring, nor asking what a singular vector is.

Contents

CHAPTER 1

Introduction

Meteorology is the study of atmospheric phenomena, particularly as a means of forecasting future weather events. Weather forecasts are produced by evolving the estimated current atmospheric state forward in time using large non-linear numerical models of the physical and dynamical processes in the atmosphere. The ability to create accurate numerical forecasts is reliant on both the accuracy of these models and the accuracy of the initial conditions. The initial conditions used in weather forecasting are statistically based 'compromises' between observational data and a previous forecast, which are generated by a process known as data assimilation. Since Lorenz (1963) brought chaos theory to the attention of meteorologists, it has been understood that the non-linear nature of evolutionary process in the atmosphere causes errors (no matter how small) in initial conditions supplied to the forecast models to eventually grow into large errors in the forecast. This chaotic behaviour is referred to as sensitivity to initial conditions and is often summed up with the flippancy "if a butterfly flaps its wings in Brazil a tornado is set off in Texas". As a direct result of the work of Lorenz (1963), meteorologists began to speculate about the existence of a theoretical upper limits to the times-scales over which an accurate forecast can be made. Since the publication of Lorenz (1963), improvements in numerical models and observation density have lead to large improvements in forecast accuracy. With the continued development of numerical forecasting methods and new observation platforms, it is hoped that there is still room for improvement before any theoretical limit of predictability is reached.

Since the mid 1990s, there has been a move to make forecast generation methods more specific to the atmospheric flow on a particular day and the requirements of the end user. One part of this move has been the development of methods by which the observation distribution resulting in the most accurate forecast may be *objectively* determined. With the development of new 'movable' observation platforms, the possibility of day to day variations in the observation network based on the specific requirements of the forecast may present itself; Emanuel et al. (1995). Observations obtained in this manner have come to be known as 'targeted' or 'adaptive' observations; Lorenz and Emanuel (1998).

Several questions surround the use of an adaptive observation strategy. Most of these questions are summed up in the words of Thompson (1957):

"*What return in increased predictability can be expected from increasing the overall density of reporting stations, and how does this compare with the corresponding outlay of funds? Where is the point of rapidly diminishing return per outlay? How should the new stations be located in effecting the increase of overall station density?*"

Thompson (1957), however, was writing about the development of a larger network of *fixed* observations, and so for 'targeted' observations a further question exists: What methods can be used to identify the best observation locations on a day to day basis? Attempting to answer these questions several targeting methods have already been proposed and tested 'in the field'. This thesis is a further contribution to the answers to two of these questions, namely,

Where should the additional observations be located?

and

What method should be applied to identifying these locations?

Answers to a further 'sub-question',

Why should the observations be placed in these locations?,

are also sought. An outline of the findings of this thesis can be found at the end of this introductory chapter. Prior to this, we shall give a more detailed explanation of the subject of adaptive observations. To put the subject of adaptive observations in context, the following section discusses the properties of a 'generic' weather forecasting system. The available literature on the subject of adaptive observations is then discussed in Section 1.2. The final section of this chapter contains a summary of the main conclusions and chapter contents of the thesis.

1.1 Forecast-Analysis Systems

This section serves as an illustration of the generic properties of weather forecasting systems. It is not intended to give a full discussion of the specifics of topic but rather to introduce concepts and terminologies that will be relevant to subsequent discussions. The production of accurate weather forecasts requires the ability to perform two tasks: Firstly to propagate an estimate of the current atmospheric state forward in time; Secondly to make accurate estimates of the current atmospheric state. The first of these tasks is performed using large numerical weather prediction (NWP) models. The second is performed by combining observations of the current state of the atmosphere with an estimate of the atmospheric state from a previous forecast.

NWP models are a set of discrete non-linear equations that approximate the physical and dynamical processes in the atmosphere. The integration of a NWP model over a finite time interval τ from an initial state $\boldsymbol{\chi}^a(0)$ to a forecast state $\boldsymbol{\chi}^f(\tau)$ can be written as the non-linear operator

equation

$$\boldsymbol{\chi}^f(\tau) = \mathscr{M}\left[\boldsymbol{\chi}^a(0), \tau\right] \tag{1.1}$$

where $\boldsymbol{\chi}$ is a vector containing the model state variables (pressure, temperature, velocity at different grid points for example) and $\mathscr{M}$ is a non-linear operator containing the model equations.

The second task required for the successful production of a forecast needs slightly more explanation. Ideally the model would be initialised using a set of homogeneously distributed accurate observations, at least equal in number to the number of variables in the the model state vector $\boldsymbol{\chi}$. Unfortunately, due to the high dimension of the model state and the inaccessibility of many required observation locations, the observations are neither large enough in number nor homogeneous enough in their distribution to specify entirely the model state. In order to solve this problem the observational data are combined with a previous forecast to produce the estimated current atmospheric state, $\boldsymbol{\chi}^a$, based on the estimated statistics of the error in both the forecast and observations. This process is known as data assimilation. The forecast used in the data assimilation process is known as the background. The estimated state obtained through the data assimilation process is known as the analysis. The various data assimilation methods in use in weather forecasting centres derive from the minimisation of the quadratic cost function

$$\mathscr{J}(\boldsymbol{\chi}) = \frac{1}{2}\left(\boldsymbol{\chi} - \boldsymbol{\chi}^b\right)^T B^{-1}\left(\boldsymbol{\chi} - \boldsymbol{\chi}^b\right) + \frac{1}{2}\left(\boldsymbol{y} - \mathscr{H}\left[\boldsymbol{\chi}\right]\right)^T R^{-1}\left(\boldsymbol{y} - \mathscr{H}\left[\boldsymbol{\chi}\right]\right), \tag{1.2}$$

where the vector $\boldsymbol{\chi}$ is the control vector[1], $\boldsymbol{\chi}^b$ is a vector containing the background, $\boldsymbol{y}$ is a vector containing the observations, $\mathscr{H}$ is the forward model (or observation operator) which transforms

[1]Here we assume the control vector contains the same variables as the model state. In general any variables that are uniquely related to the model state can be used for the control vector.

the model variables to the observed variables, R is matrix containing an estimate of the covariance between observational errors, and B is a matrix containing an estimate of the covariance between the errors in the background. From this cost function the analysis $\boldsymbol{\chi}^a$ can be defined as the vector $\boldsymbol{\chi}$ for which $\mathscr{J}(\boldsymbol{\chi})$ is minimised. In order to formulate the cost function, certain assumptions have to be made about the background and observation errors. These assumptions are, that the observation and background errors are statistically independent, and that individually the assumed error statistics must lead to non-singular covariance matrices. The assumption of non-singular covariance matrices essentially implies that all possible states must have a reasonable probability of existing, even if in the current atmospheric flow they are so unlikely that their probability of existing is very close to zero. A useful property of the cost function is that if the approximation to the background and observation errors is 'good' and the forward model can be approximated by the linear operator H, the analysis error covariance matrix A is equal to the inverse of the Hessian (second derivative with respect to $\boldsymbol{\chi}$) of the cost function; i.e.

$$A \equiv \left[\frac{\partial^2 \mathscr{J}}{\partial \boldsymbol{\chi}^2}\right]^{-1} = \left[B^{-1} + H^T R^{-1} H\right]^{-1}. \tag{1.3}$$

Ideally the covariance matrices in the cost function would depend on the time of observation and the observations would be used to correct the model state corresponding to the time of observation. To make the background error covariance time specific one could in theory evolve the analysis error covariance matrix. In reality however the dimension of the model state vector is typically greater than 10^6 so that the background error covariance cannot be stored by current computers, let alone evolved or explicitly inverted. Due to the limitations in computational power and concerns that evolving covariance matrices may become singular, many methods of solving approximate cost functions have been developed. It is not our intention to give a detailed dis-

cussion of these methods but some of the more general properties will be highlighted. One such approximation to the cost function is the (extended) Kalman filter. The essential components of the (extended) Kalman filter are that the covariances are evolved using a linear approximation to Equation (1.1) and the observations are assimilated sequentially into the background field at the 'correct' time. The computational expense required to implement a Kalman Filter for NWP models is presently too great for the computers used at meteorological centres. 3D-Var and 4D-Var data assimilation schemes are commonly used operationally in meteorological centres. The essential components of 3D-Var are: the background error covariance matrix is assumed to be stationary in time; spatial correlations between errors in the background field are typically assumed to be separable in the vertical and horizontal directions and isotropic in the horizontal direction; the cost function is minimised (usually approximately) by an iterative algorithm. In 3D-Var the observations are assimilated into the background at predetermined discrete intervals (analysis cycles) and the time point in the background field evolution at which the observation are assimilated does not necessarily correspond to the observation time. 4D-Var is an extension to 3D-Var in which a linear dynamical model is incorporated into the forward model (observation operator), so that the distribution of the observations in time is taken into account in the assimilation process.

Due to the sensitivity of non-linear models to errors in the initial conditions, there has been a move by meteorological services in recent years towards 'ensemble forecasting'. In ensemble forecasting, rather then creating a single forecast, an ensemble of forecasts is created by adding small perturbations $\boldsymbol{\delta\chi}_i$ to the initial condition. The motivation behind ensemble forecasting is to make a probabilistic forecast rather than a single deterministic forecast. The most likely forecast

can then be given by the ensemble mean

$$\bar{\boldsymbol{\chi}}_i^f(\tau) = \sum_{i=1}^{N_e} \frac{\boldsymbol{\chi}_i^f(\tau)}{N_e} = \sum_{i=1}^{N_e} \frac{\mathscr{M}\left[\boldsymbol{\chi}^a(0) + \boldsymbol{\delta\chi}_i, \tau\right]}{N_e}, \tag{1.4}$$

where N_e is the number of ensemble members. One immediate question that arises from the ensemble method is what form should the perturbations to the initial conditions take. Two methods for generating initial perturbations exist. These are the breeding method and the singular vector method. The singular vector method is motivated by the assumption that the effect of the data assimilation process is to randomise the initial condition errors; Palmer et al. (1998). Since the initial condition errors are assumed to be random, it is assumed that by perturbing the initial conditions with the perturbations that grow the most over the forecast integration, the most relevant information about the forecast error is obtained; Palmer et al. (1998). It is the desire to get the greatest spread in the ensemble that motivates the use of singular vectors to define perturbations for ensemble forecasting; Molteni et al. (1996). In meteorological applications, singular vectors are used as estimates of the phase space directions which amplify the most over a finite time period. Singular vectors will be discussed in more depth in the next section. Like the singular vector method, the breeding method aims to maximise the spread of the ensemble, but with the qualification that the growth be sustainable; Toth and Kalnay (1997). In the breeding method a small perturbation is added to the initial conditions. Both initial conditions are evolved with the non-linear model over one analysis cycle. The resultant fields are then subtracted from each other to obtain the evolved perturbation. This evolved perturbation is then reduced in amplitude, added to the new initial conditions and the process is repeated. This continual evolution and amplitude reduction is designed to replicate the evolutionary behaviour of the errors over multiple analysis cycles; Toth and Kalnay (1997).

1.2 Adaptive Observations

1.2.1 Summary of Adaptive Observations

The question as to the best deployment of observational resources has long been of interest to meteorologists; e.g. Thompson (1957). In recent years the development of practical methods for identifying the best locations for additional observations based on the day to day variations of the atmosphere has become an active area of research. This subject area has been referred to variously as adaptive or targeted observations. One immediate question which arises from adaptive observations is how to define what is meant by the best location. Generally speaking, adaptive observations can be motivated by the desire to achieve two different, but interrelated, goals. The first possible aim of targeting is to obtain the best analysis achievable with the limited observational resources. Lorenz and Emanuel (1998) and Morss et al. (2001) have proposed methods which utilise estimates of the initial condition errors from ensemble forecasts to identify regions where the initial condition errors are large. By targeting observations to areas with large initial condition errors it is hoped that the maximum improvement in the *analysis* can be obtained. Whilst maximally reducing the initial condition error *may* reduce the subsequent forecast error, this is not explicitly the aim of the targeting methods proposed by Lorenz and Emanuel (1998) and Morss et al. (2001). The other possible goal of adaptive observations is that of reducing forecast error. For the work in this thesis we are concerned only with this second goal; i.e. that of maximally reducing forecast error. For current targeting techniques the aim of targeting is usually defined as finding the observations that will maximally improve the forecast within a geographically localised verification region at a specific verification time.

Several targeting methods which seek to identify the observation locations that maximally reduce

forecast error have been proposed. These targeting methods have been loosely classified into two types: those which rely on non-linearly evolved ensembles to incorporate information about small error dynamics, such as Ensemble Transform [Bishop and Toth (1999)] and the ensemble transform Kalman filter [Bishop et al. (2001)]; and those which rely on linear approximations to inform the target selection about the error dynamics, such as gradient sensitivity [Bergot et al. (1999), Pu et al. (1998)], quasi-inverse linear method [Pu et al. (1997)] and singular vector targeting methods [Buizza and Montani (1999), Montani (1998)]. Of these methods, two in particular have come to the fore and were used in determining the observation locations during the 'Atlantic Thorpex Regional Campaign' (AtREC) field test of targeted observations in 2003. These two methods are the singular vector method [Buizza and Montani (1999)] and the ensemble transform Kalman filter method [Bishop et al. (2001)].

Berliner et al. (1999) set out a simplified but 'well posed' statistical framework for the targeting problem. This statistical framework may be summarised as follows: Given an estimate of the atmospheric state at time t_0 and the error statistics associated with that estimate, identify the observations at a later time t_1 that will optimise by some measure the expected errors in the subsequent forecast at t_2. Berliner et al. (1999) suggest several measures which may be used to define an optimality criterion. Of these measures, the *expected* forecast error variance is of most direct relevance to the targeting methods in the current literature. Berliner et al. (1999) refer to criteria for observation selection that minimise the expected forecast error variance as A-optimal criteria. We may summarise the essential components of an A-optimal targeting method as: an estimate of the error statistics at t_1, an estimate of the effect of observations on those statistics and an estimate of the evolution of the statistics up to t_2. All the targeting methods discussed in this section (with appropriate assumptions) can be viewed as roughly falling into this description.

Additionally, all the targeting methods discussed in this section rely on the assumption that the evolution of the error statistics is linear. This is equally true of methods which make explicit use of linear operators and those that rely on non-linearly evolved ensembles. The accuracy of the linear approximation is dependent on the amplitude of the perturbation, since for small perturbations the amplitude of non-linear terms in a series expansion of the dynamical equations are smaller than the linear terms. However, since atmospheric dynamics leads to perturbation amplification, it is expected that the accuracy of the linear approximation deteriorates over time. The time period over which the linear approximation is valid is referred to as 'the linear regime'. Several investigations into the duration of the linear regime for perturbations with initial amplitude consistant with the estimated amplitude of initial condition/analysis errors have determined the maximum duration of the linear regime to be roughly two to three days; see for example Errico et al. (1993), Rabier and Courtier (1992) and Vukicevic (1991). The validity of this linearity assumption is questioned by Gilmour et al. (2001).

1.2.2 The singular vector method for observations targeting

The first of the two targeting methods that were used in the AtREC field experiment is the singular vector method. In simplistic terms the essential components of the singular vector method can be summarised thus: A small set of perturbations (the singular vectors) that maximise the amplification of small perturbations to the initial conditions over the finite forecast integration period are calculated; the observations are then targeted to regions in which this set of perturbations weighted by their amplification over the forecast period have large amplitude. The finer details of this method are somewhat more complex than this simplistic explanation so we shall break it down into three sections. Firstly we shall describe the mathematical properties and computation

of the singular vectors. Secondly we shall describe the implementation of the targeting method using the singular vectors. Finally we shall identify some assumptions that may be used to link the method to the generic description of 'A-optimal' targeting methods.

To compute the singular vectors, it must first be assumed that the dynamical behaviour of the perturbations (or errors) we are interested in is well approximated by a linearisation of the dynamical equations about a time varying background state. For targeting applications, this background state is the portion of the forecast started at t_0 which lies between t_1 and t_2. This linearisation gives rise to the linear operator

$$M\left[\boldsymbol{\chi}(t_1), t_2\right] = \frac{\partial \mathscr{M}}{\partial \boldsymbol{\chi}}\left[\boldsymbol{\chi}(t_1), t_2\right] \tag{1.5}$$

which approximates the evolution of perturbations $\boldsymbol{\delta\chi}(t_1)$ to the state $\boldsymbol{\chi}(t_1)$ over the interval t_1 to t_2. The evolution of perturbations over this finite time interval is then described by

$$\boldsymbol{\delta\chi}(t_2) = M\left[\boldsymbol{\chi}(t_1), t_2\right]\boldsymbol{\delta\chi}(t_1) + \mathscr{O}(\delta\chi^2). \tag{1.6}$$

The $\mathscr{O}(\delta\chi^2)$ terms are assumed to be much smaller than $M\left[\boldsymbol{\chi}(t_1), t_2\right]\boldsymbol{\delta\chi}(t_1)$ and neglected, yielding a linear evolution equation. The use of a linear approximation to the non-linear evolution of perturbations to the state of atmospheric models is usually justified on the grounds that the amplitude of the perturbations are assumed to be initially small, and the time periods over which the approximation is applied does not exceed two to three days. Hereafter $M\left[\boldsymbol{\chi}(t_1), t_2\right]$ will be donated simply as M.

The singular vectors used in targeting are obtained by computing the singular value decomposition of the matrix $K = E_2^{\frac{1}{2}} T_2 M E_1^{-\frac{1}{2}}$ (Buizza and Montani (1999)); where $E_1^{-\frac{1}{2}}$ and $E_2^{\frac{1}{2}}$ are

matrices which normalise the initial and final perturbations respectively, and T_2 is a local projection operator. Here we use the subscripts 1 and 2 to refer to the time at which each operator is applied; e.g. those applied to the perturbation at t_1 are subscripted 1. The local projection operator is an operator that sets the amplitude of the perturbation to zero outside the verification region and is usually defined as a symmetric matrix; e.g. Buizza (1994). Several definitions of the terms singular value decomposition, singular vector and singular value appear in the meteorological literature. For clarity we shall restrict our definition of these three terms to that given in linear algebra texts such as Golub and Van Loan (1983) and Strang (1988). The singular value decomposition (expansion) is defined

$$K = \sum_{i=1}^{rank(K)} \sigma_i \boldsymbol{u}_i \boldsymbol{v}_i^T; \tag{1.7}$$

where σ_i, $\boldsymbol{u}_i$ and $\boldsymbol{v}_i$ are the singular values, left singular vectors and right singular vectors respectively. By convention the singular values are ordered such that

$$\sigma_1 \geq \sigma_2 \geq \ldots \sigma_{rank(K)} > 0. \tag{1.8}$$

The left and right singular vectors satisfy the orthonormality relationships

$$\boldsymbol{v}_i^T \boldsymbol{v}_j = \begin{cases} 1, & i = j \\ 0, & i \neq j \end{cases}, \tag{1.9}$$

$$\boldsymbol{u}_i^T \boldsymbol{u}_j = \begin{cases} 1, & i = j \\ 0, & i \neq j \end{cases}, \tag{1.10}$$

and the equations

$$K\boldsymbol{v}_i = \sigma_i \boldsymbol{u}_i, \tag{1.11}$$

and

$$K^T \boldsymbol{u}_i = \sigma_i \boldsymbol{v}_i. \tag{1.12}$$

Due to the high dimension of the numerical models used in atmospheric modelling, the matrix K is too large to allow for direct computation of the singular value decomposition. In practice only a few of the leading right singular vectors are computed via the Lanczos algorithm; Golub and Van Loan (1983). By the term 'leading' singular vector we refer to those associated with large singular values. From the indexing convention given in Equation (1.8) the leading N singular vectors are those corresponding to $i = 1$ to $i = N$.

The left and right singular vectors are related to model state perturbations at t_1 and t_2 via

$$\boldsymbol{\delta\chi}_i(t_1) = E_1^{-\frac{1}{2}} \boldsymbol{v}_i \tag{1.13}$$

and

$$T_2 \boldsymbol{\delta\chi}_i(t_2) = \sigma_i E_2^{-\frac{1}{2}} \boldsymbol{u}_i; \tag{1.14}$$

where

$$\boldsymbol{\delta\chi}_i(t_2) = M \boldsymbol{\delta\chi}_i(t_1). \tag{1.15}$$

Each right singular vector can be transformed to a corresponding perturbation of the state vari-

ables at time t_1. Each left singular vector can be transformed to a local perturbation of the state variables at time t_2. This local perturbation is the localisation of the perturbation evolved from $\boldsymbol{\delta\chi}_i(t_1)$ over the finite time interval t_1 to t_2. From the orthogonality relationships given in Equations (1.9) and (1.10) it is evident that $\boldsymbol{\delta\chi}_i(t_1)$ and $T_2\boldsymbol{\delta\chi}_i(t_2)$ are orthogonal with respect to the inner products defined by the matrices E_1 and E_2 respectively; i.e.

$$\boldsymbol{\delta\chi}_i^T(t_1)E_1\boldsymbol{\delta\chi}_i(t_1) = \begin{cases} 1, & i = j \\ 0, & i \neq j \end{cases}, \tag{1.16}$$

$$\boldsymbol{\delta\chi}_i^T(t_2)T_2E_2T_2\boldsymbol{\delta\chi}_i(t_2) = \begin{cases} 1, & i = j \\ 0, & i \neq j \end{cases}. \tag{1.17}$$

The singular value decomposition of the matrix K can therefore be used to define a set of dynamical perturbations $\boldsymbol{\delta\chi}_i(t_1)$ which are orthonormal with respect to the 'E_1 inner product'. These perturbations evolve over the finite time interval to the corresponding evolved perturbations $\boldsymbol{\delta\chi}_i(t_2)$. These evolved perturbations are orthonormal within the local region defined by the local projection operator T_2.

A very important aspect of the singular value decomposition is that the singular vectors form a complete set. This means that any state perturbation $\boldsymbol{\delta\chi}$ may be written as a linear combination of either the right or left singular vectors. If K is not full rank then some of these singular vectors will be associated with zero singular values. The real power of singular vectors is seen when a perturbation to the state at t_1 is written as the linear combination

$$\boldsymbol{\delta\chi}_i(t_1) = \sum_{i=1}^{N_s} \gamma_i E_1^{-\frac{1}{2}} \boldsymbol{v}_i, \tag{1.18}$$

where $\gamma_i = \boldsymbol{v}_i^T E_1^{\frac{1}{2}} \boldsymbol{\delta\chi}_i(t_1)$ is the 'E_1' projection coefficient of $\boldsymbol{\delta\chi}_i(t_1)$ onto the i^{th} singular vector and N_s is the number of elements in the vector $\boldsymbol{\delta\chi}$. When the perturbation at t_1 is written in this form then the amplitude within the verification region of the evolved perturbation measured in the norm defined by the 'E_2' inner product is given by

$$\|T_2\boldsymbol{\delta\chi}_i(t_2)\|_{E_2}^2 = \boldsymbol{\delta\chi}_i^T(t_2)T_2E_2T_2\boldsymbol{\delta\chi}_i(t_2) = \sum_{i=1}^{N_s}\gamma_i\sigma_i^2. \tag{1.19}$$

Furthermore, if the initial condition errors at t_1 are 'white' with respect to the E_1 inner product then the expected value of γ_i is equal to a constant γ for all i; Palmer et al. (1998). If the initial condition error is white with respect to the E_1 inner product and the approximation of the error evolution by M is valid then the expected error variance in the verification region at t_2 as measured in the E_2 norm is given by

$$\mathcal{E}\left[\|T_2\boldsymbol{\delta\chi}_i(t_2)\|_{E_2}^2\right] = \frac{\gamma}{N_s}\sum_{i=1}^{N_s}\sigma_i^2. \tag{1.20}$$

Due to the high dimension of the numerical models used in meteorological centres exact calculation of Equation (1.20) is computationally expensive and time consuming. Since the Lanczos algorithm allows the computation of the leading singular vectors without the expense of computing all the singular vectors, Equation (1.20) can be approximated using the first N singular vectors.

In singular vector targeting the observations are directed towards regions in which the amplitudes of the right singular vectors weighted by their singular values are 'large'; e.g. Buizza and Montani (1999). The idea being that by reducing the errors in regions where the singular vector amplitude is large one reduces the amplitude of the projection γ_i of the error at time t_1 onto the leading right singular vectors. From Equation (1.19) it is evident that reducing the magnitude of γ_i for the

leading right singular vectors will reduce the forecast error. Furthermore if the initial condition errors at t_1 are 'white' with respect to the E_1 inner product and the *expected* effect of placing observations in region defined by a local projection T_1 is to uniformly reduce the amplitude of the error in that region it can be shown that the reduction in expected forecast error variance obtained by observing in T_1 is

$$\mathcal{E}\left[\|T_2\boldsymbol{\delta\chi}_i(t_2)\|^2_{E_2} - \|T_2\boldsymbol{\delta\chi}_i(t_2,T_1)\|^2_{E_2}\right] = \frac{\gamma}{N_s}\sum_{i=1}^{N_s}\sigma_i^2\boldsymbol{v}_i^T T_1\boldsymbol{v}_i, \tag{1.21}$$

where $\boldsymbol{\delta\chi}_i(t_2,T_1)$ is written as a function of T_1 to distinguish it from the forecast without additional observations. From this expression it is evident that the singular vector method is in some ways A-optimal. Equation (1.21) will be discussed in more detail in Chapter 4 however it is introduced here to motivate singular vector targeting as an A-optimal targeting method. A significant difference between the singular vector method and the A-optimal design of Berliner et al. (1999) is that in the singular vector method the observations are not explicitly taken into account.

Whilst the use of singular vectors in targeting can be motivated as an A-optimal targeting method, several other interpretations of their use exist. The specific interpretation of the singular vectors depends on the choice of the matrices E_1 and E_2; Palmer et al. (1998). We have already noted that the A-optimal interpretation of singular vector targeting requires that the matrix E_1 is chosen as the covariance matrix of the initial condition errors at t_1. In theory, the matrix E_2 can be chosen to measure the aspects of the forecast errors that are considered most vital to remove, however in practice, E_2 is almost universally chosen such that the associated inner product is a measure of the total energy (kinetic energy plus potential energy) of the perturbation. If E_1 is chosen to be the same as E_2, then the singular vector calculation yields the perturbations that amplify the most over the forecast interval t_1 to t_2. In this case the use of singular vector targeting can be motivated by

the desire to prevent the errors from growing over the forecast interval. Typically for this optimal amplification motivation both E_1 and E_2 are chosen such that their associated inner products give the total energy of the perturbation. Palmer et al. (1998) test the consistency of the several potential metrics with estimates of the analysis error covariance metric. The tested metrics are total energy, streamfunction, kinetic energy and enstrophy. Of the four metrics that Palmer et al. (1998) test, it is found the total energy is the least inconsistent with the analysis error covariance metric. The use of total energy to define the metrics at both the start and end of the forecast interval can therefore be seen as an attempt to both target the growing errors and to achieve the A-optimal goal of minimising the expected forecast error variance. However, since the total energy metric takes neither the observation network nor the atmospheric dynamics prior to t_1 into account, it can be at best weakly related to the analysis error covariance metric. The use of total energy singular vectors in targeting is therefore more easily justified on the grounds of preventing error growth. Barkmeijer et al. (1998) demonstrate the computation of singular vectors using the Hessian of the 3D-Var[2] cost function to define the metric at t_1. These 'Hessian singular vectors' are computed using the total energy metric at t_2 and the Hessian metric at t_1. Since the metrics differ at t_2 and t_1 the Hessian singular vectors cannot be interpreted as optimally *growing* perturbations. However since the inverse of the Hessian matrix is in theory equal to the analysis error covariance matrix the use of Hessian singular vectors for targeting is more consistent with the A-optimal design outlined by Berliner et al. (1999). However the background error covariance matrix used in operational data assimilation systems are not (at present) dependent on the day to day variations of the atmospheric flow. The background error covariance matrices used in 3D-Var and 4D-Var are modelled to reflect the climatological statistics of the analysis errors so that they can be applicable to multiple forecast analysis cycles. These background error covariance matrices often

[2]more recently the Hessian of the (incremental) 4D-Var cost function has been used; Leutbecher (2003)

contain many simplifications designed to reduce computational expense. The Hessian metric does however take explicit account of the location and estimated accuracy of routine observations.

In summary, singular vector targeting identifies a region in which it is determined that observations are expected to be most beneficial. This type of targeting can be motivated to a certain extent by the A-optimal design of Berliner et al. (1999) and/or by the desire to prevent error growth between t_1 and t_2. The exact interpretation of the method depends on the specific choices of the matrices E_1 and E_2, which define the metrics at t_1 and t_2 respectively. In the case where E_1 and E_2 are identical, the computed singular vectors can be interpreted as the perturbations which amplify the most with respect to the inner product associated with E_1 and E_2 over the finite time interval t_1 to t_2. In the case of the identical E_1 and E_2 therefore targeting with singular vectors can be thought of as an attempt to prevent the amplification of errors. Preventing errors from amplifying however is not necessarily consistent with reducing the forecast error since for example non-amplifying errors which have large amplitude at t_1 may have a significant impact on the forecast error at t_2. If however the metric at t_1 is chosen to represent the statistics of the analysis errors at t_1 then the singular vector targeting method can be related to the A-optimality motivation of Berliner et al. (1999). Since the singular vector targeting method does not explicitly take into account the character and deployment of the adaptive observations it can arguably only be A-optimal 'in spirit' rather than in actuality. Singular vector targeting is more easily thought of as means of identifying 'sensitive regions'; i.e. regions in which small variations in the initial conditions are likely to lead to large variations in the forecast.

1.2.3 The ensemble transform Kalman filter method of observation targeting

The second of the two targeting methods which have were used during the AtREC experiments is the ensemble transform Kalman filter; Bishop et al. (2001). The ensemble transform Kalman Filter has its root in the Ensemble transform technique devised by Bishop and Toth (1999). Both Ensemble transform and ensemble transform Kalman filters fit comfortably within the A-optimal framework of Berliner et al. (1999). The essential aim of both these methods is to predict the forecast error variance at t_2 associated with a particular deployment of observations at t_1. In ensemble transformation, the analysis error covariance matrix associated with a particular deployment of observations at t_1 is estimated, using linear transformation ensemble forecast initialised at t_0. The approximate analysis error covariance matrix is defined

$$A_1 \approx D_1 C C^T D_1^T \tag{1.22}$$

where the columns of the matrix D_1 are given by the normalised departures $\boldsymbol{d}_i(t_1)$ of the ensemble members $\bar{\boldsymbol{\chi}}^f$ at t_1 from the ensemble mean and C is a linear transformation to be determined. The normalise departures are defined

$$\boldsymbol{d}_i(t_1) = \frac{\boldsymbol{\chi}_i^f(t_1) - \bar{\boldsymbol{\chi}}_i^f(t_1)}{(N_e - 1)^{\frac{1}{2}}}; \tag{1.23}$$

where $\boldsymbol{\chi}_i^f(t_1)$ is the i^{th} ensemble member at t_1, $\bar{\boldsymbol{\chi}}_i^f(t_1)$ is the ensemble mean at t_1 and N_e is the number of ensemble members. The method for determining C will be discussed a little later. We shall first concentrate on how C is used to estimate the forecast error for a given deployment of observations. Once the transformation matrix C associated with a particular observation deployment has been determined, the resultant forecast/background error covariance matrix at t_2 is then

approximated by

$$B_2 \approx D_2 C C^T D_2^T \tag{1.24}$$

where D_2 is the matrix of normalised departures $\boldsymbol{d}_i(t_2)$ at t_2. The essential assumption in determining the relationship between A_1 and B_2 is that the forecast errors evolve linearly about the forecast trajectory defined by the ensemble mean. This linear assumption implies that

$$B_2 = M\left[\bar{\boldsymbol{\chi}}^f(t_1), t_2\right] A_1 M^T \left[\bar{\boldsymbol{\chi}}^f(t_1), t_2\right] \tag{1.25}$$

and

$$D_2 = M\left[\bar{\boldsymbol{\chi}}^f(t_1), t_2\right] D_1. \tag{1.26}$$

Combining Equations (1.22), (1.25) and (1.26) one readily obtains Equation (1.24).

In the ensemble transform technique, the transformation matrix C is computed by specifying the form of A_1 associated with a given observational deployment and solving Equation (1.22) for C. The ensemble transform Kalman filter is an extension to the ensemble transform technique, in which the matrix A_1 is (theoretically) determined by substituting the approximate background error covariance

$$B_1 \approx D_1 D_1^T \tag{1.27}$$

at t_1 into the Hessian of the cost function (Equation (1.3)) and inverting. The transformation matrix, C, associated with this estimated analysis error covariance matrix is then obtainable as before from Equation (1.22). The actual calculations used in the ensemble transform Kalman

filter are significantly more efficient than these described here. For a full discussion on these calculations, see Bishop et al. (2001).

To implement the ensemble transform Kalman filter for adaptive observations, the method can be applied to multiple possible deployments of observations and the most favourable deployment selected. The favourability of the targeted observations is quantified from the 'signal variance' at t_2

$$s(t_2) = trace\left\{E_2^{\frac{1}{2}} T_2 D_2 (I - C_1 C_1^T) D^T T_2 E^{\frac{1}{2}}\right\}, \tag{1.28}$$

where E_2 and T_2 are the "inner product defining" and local projection matrices respectively used in singular vector targeting; Bishop et al. (2001). As with singular vector targeting total energy is usually used to define E_2. If the assumption of linear error evolution is valid and the approximated covariance matrices B_1, A_1 and R are accurate and consistent with the data assimilation system used in the weather forecasting centre, then the signal variance is equivalent to the expected reduction in forecast error variance induced by the observations; Bishop et al. (2001). This equivalency is also reliant on the accuracy with which the forecast model can evolve a given initial condition. In practice the matrices B_1 and A_1 are not consistent with those used in operational data assimilation systems and the ensemble transform Kalman filter has a tendency to over estimate the effects of observations on the forecast; Majumdar et al. (2001).

Unlike singular vector targeting, the Ensemble Transform Kalman Filter explicitly takes the assimilation process into account, although this assimilation process does not correspond to the actuality of operational assimilation systems. Also, the singular vector method makes no attempt to identify the optimal observational deployment, and only defines a region to be observed. It must be noted however that the Ensemble Transform Kalman Filter is often used only to generate

'summary maps' of the signal variance, which are then used to identify target regions, and not specific observation locations; Majumdar et al. (2002). A second difference between the Ensemble Transform Kalman Filter and singular vector targeting is that, for the singular vector method, the covariance matrix of the initial condition errors is modelled by the flow-independent matrix E_1, whereas for the ensemble transform Kalman filter the initial condition covariance matrix is modelled by the flow dependent ensemble perturbations.

1.2.4 Variations of the singular vector and Ensemble Transform Kalman filter observation targeting methods

Several 'variants' of the singular vector and ensemble transform Kalman filter targeting methods have been proposed. Leutbecher (2003) applies the methodology of the ensemble transform Kalman filter to the Hessian singular vectors used in singular vector targeting. This method arguably has several advantages over both singular vector targeting and the ensemble transform Kalman filter. In the former case the Hessian reduced rank, as the method of Leutbecher (2003) has come to be known, has advantages over the 'regular' singular vector targeting method in that it explicitly takes the assimilation process into account in determining the target region. The Hessian reduced rank has two advantages over the ensemble transform Kalman filter method. The first of these two advantages is that the assimilation scheme assumed by the Hessian reduced rank is consistent with the operational data assimilation scheme; Leutbecher (2003). A second less obvious advantage is that the use of the local projection operator T_2 in the singular vector calculation means that by design the Hessian singular vectors used in the Hessian reduced rank contain only information relevant to the verification region. By contrast the ensemble members used in the ensemble transform Kalman filter are designed to maximise the amount of information about the

'global' error statistics. It may be inferred therefore that a greater number of ensemble members than Hessian singular vectors are required to accurately assess the effects of observations on the forecast error in the verification region. However the ensemble used in the ensemble transform Kalman filter is available 'for free' from the ensemble forecast Majumdar et al. (2001) whereas the computationally expensive targeting Hessian singular vectors are an added expense to the routine forecasting system. A very significant difference between the ensemble transform Kalman filter and the Hessian reduced rank is that while the former takes into account the dynamical evolution of the errors between t_0 and t_1 the latter does not since the Hessian of the 3D/incremental 4D VAR cost function is not flow dependent. Kim et al. (2004) propose targeting observations to locations where non-linearly evolved singular vectors have large amplitude. In the method of Kim et al. (2004) the singular vectors are computed for the interval t_0 to t_2 and the target locations specified using the right singular vector non-linearly evolved to t_1. Hamill and Snyder (2002a) consider the use of background error covariance estimates obtained from an ensemble Kalman filter to specify the location of observations required to optimally improve the analysis at t_1. This method uses the flow dependent background errors to specify the error statistics at t_1 but takes into account that these error statistics may not correspond to the error statistics assumed by the operational data assimilation system. Although, it must be stressed that the method of Hamill and Snyder (2002a) is designed to improve the analysis at t_1 and not the forecast at t_2. Hamill and Snyder (2002a) *do* define a method for determining the forecast improvement at t_2, but this additional method is only applicable if an ensemble Kalman filter is used operationally.

1.3 Thesis Summary

This thesis covers topics in two areas. In the first half of the thesis, the dynamics of singular vectors in the Eady model are discussed. In the second half of the thesis, this discussion is then extended to adaptive observations. In this thesis the role of dynamically evolved background errors on the efficacy of targeted observations is examined. In particular the effect of using evolved singular vectors to specify the dynamically organised component of the background error is investigated. In the first half of the thesis the dynamics of singular vectors in the Eady model are investigated. In the second half the use of singular vectors in targeting is investigated. Firstly the effect of singular vector dynamics on the location of targets identified using singular vectors is investigated, by considering the singular vector targeting function (e.g. Buizza and Montani (1999)), which is usually a vertical integral, in the height-zonal plane. Following this a new targeting method, that utilises these evolved singular vectors to approximate the leading eigenvectors of the flow dependent background errors, is introduced. The evolved singular vectors are combined with the singular vectors used in current singular vector targeting schemes (e.g. Buizza and Montani (1999)) to estimate the reduction in forecast error variance which will be obtained from a given deployment of observations. Although this targeting method uses a flow dependent background error covariance model, it does not rely on the assumption that the operational data assimilation system is a Kalman filter, as is the case of the ensemble transform Kalman filter (ETKF) method; Bishop and Toth (1999).

The thesis is divided into chapters as follows:

Chapter 2 contains a description of the Eady model used in this thesis.

Chapter 3 contains an analysis of the singular vectors of the Eady model.

Chapter 4 contains a examination of the sensitivity based singular vector targeting, in the context of the Eady model singular vectors.

Chapter 5 contains the description of a new singular vector based targeting method, and the analysis of the method in the context of the Eady model singular vectors.

Chapter 6 contains a summary of the main conclusions of this thesis.

CHAPTER 2

The Eady model

2.1 Introduction

This chapter contains a summary of dynamical properties of the two dimensional Eady Equations. Discrete versions of the two-dimensional Eady equations are used to define the numerical model used for experiments in this thesis. The present chapter focuses on the properties of the continuous equations. The properties of the discrete equations are discussed briefly in the next chapter and in detail in Appendix A.

The purpose of the present chapter is three-fold. Firstly, the physical motivations of the quasi-geostrophic equations, upon which the Eady Equations are based, are explained in Section 2.2. The aim of the discussion of the quasi-geostrophic equations is to motivate the Eady model as a model of the 'dynamic atmosphere', and set it in the context of a 'more complete' model of the atmosphere. The second purpose for the present chapter is to define the Eady Equations. Section 2.3 contains the formulation of the Eady Equations. The third purpose of the present chapter is to introduce the properties of the solutions and dynamical growth mechanisms of the Eady model which will prove relevant to later discussions. These solutions and growth mechanisms are described in Section 2.4.

2.2 The Inviscid, Adiabatic, quasi-geostrophic equations for incompressible flow on a Mid-latitude f-plane.

The quasi-geostrophic equations approximate the dynamics of synoptic scale (horizontal scales of $\sim 10^3 km$) depressions in the mid-latitude region (30 to 70 degrees north/south of the Equator). It is from these equations that the Eady model is obtained. In this section, we will introduce the quasi-geostrophic equations. The intention here is to highlight the underlying physics and dynamics that motivate the equations, rather than to give a fully fledged derivation. A more detailed treatment of this topic can be found in many fluid dynamics texts such as Pedlosky (1979) or Holton (1992).

We shall define the quasi-geostrophic equations in Cartesian coordinates and neglect the effects of the curvature of the Earth. The x coordinate shall point eastwards, the y coordinate northwards and the z coordinate upwards. Due to the assumed orientation we shall refer to the x, y, and z coordinates as the zonal, meridional and vertical coordinates respectively. We will use $\boldsymbol{i}$, $\boldsymbol{j}$, $\boldsymbol{k}$ to denote unit vectors in the x, y and z directions respectively. All parameters will be chosen to be consistent with the Mid-latitudes.

Many assumptions about, and approximations of, the nature of fluid flow in the atmosphere have to be made, to obtain the Quasi-geostrophic equations. For concision, we shall list some of the more basic ones here. Firstly, the atmosphere is assumed to obey the ideal gas law

$$\rho = \frac{p}{RT} \tag{2.1}$$

where ρ, p and T are the air density, pressure and temperature respectively and R is the gas con-

stant. Secondly, the effects of internal and external frictional forces on the atmosphere have been neglected. Without these viscous effects, deceleration of the winds, by the conversion of kinetic energy associated with air flow, to thermal energy does not occur within the equations. Thirdly, diabatic effects due to the presence of water vapour in the atmosphere have been neglected. This third assumption means that the transfer of thermal energy by evaporation and condensation does not occur within the Quasi-Geostrophic equations. Fourthly, due to the rotation of the Earth all fluid elements experience a centripetal acceleration pointing towards the axis of rotation. The effects of this centripetal acceleration are small and are omitted from the equations. Also due to the fact that the coordinates are defined in a rotating frame of reference all fluid elements experience an 'apparent' acceleration known as the Coriolis acceleration. For the Quasi-geostrophic equations only the vector component of the Coriolis acceleration pointing in the vertical direction is retained. The horizontal vector components of the Coriolis acceleration are assumed to be negligible away from the Equator. A further simplification to the Coriolis acceleration can be made by assuming the magnitude of vector component pointing in the vertical direction has the constant value f_0 at all latitudes. Assuming a constant Coriolis acceleration is referred to as the f-plane approximation[1]. The 'β effect' accounts for accelerations due to increased (decreased) planetary vorticity, when moving in a northwards (southwards) direction, and is important in defining the planetary scale wave (Rossby wave) motion. Making the f-plane approximation removes the 'β effect' and therefore planetary scale motion is poorly represented in the equations of motion. Finally, the gravitational acceleration is assumed to take the constant value g at all locations.

We have already made several general simplifying assumptions about the properties of atmospheric motion in the Mid-latitudes. A large number of further simplifying assumptions can be

[1]The f-plane approximation is an extension to the 'standard' Quasi-Geostrophic Equations

made based on observations of the weather systems they are designed to describe. As Eady (1949) puts it, the dynamical equations can be simplified by 'the omission of all those terms which do not make a major contribution to the particular type and scale of motion envisaged'. For the quasi-geostrophic equations the type of motions envisaged are mid-latitude depressions. Observations of these cyclonic disturbances reveal that: they are convectively stable; they have typical length and height $\mathscr{L} =\sim 10^3 km$ and $\mathscr{H} =\sim 10 km$ respectively; and they have typical velocities $\mathscr{U} =\sim 10 ms^{-1}$. With these properties in mind we shall now demonstrate the further simplifications that lead to the quasi-geostrophic equations.

Firstly for convectively stable systems we may (in almost all cases) neglect vertical accelerations and use hydrostatic balance to describe the vertical structure of the atmosphere; Eady (1949). Hydrostatic balance is a balance between the force due to vertical pressure gradients and the gravitational force; i.e.

$$\frac{\partial p}{\partial z} = -\rho g; \tag{2.2}$$

where p is the pressure and ρ is the density. The mid-latitude cyclones we wish to describe appear as small time dependent eddies in a largely hydrostatic atmosphere; the thermodynamic state of the atmosphere can be expressed as a sum of the stationary component depending on height alone and an eddy component depending on all spatial coordinates and time thus

$$p(x, y, z, t) = p_s(z) + p_e(x, y, z, t), \tag{2.3}$$

$$\rho(x, y, z, t) = \rho_s(z) + \rho_e(x, y, z, t), \tag{2.4}$$

$$\theta(x, y, z, t) = \theta_s(z) + \theta_e(x, y, z, t), \tag{2.5}$$

where the subscripts s and e denote the stationary and eddy components respectively and θ is the potential temperature. The potential temperature is related to the actual temperature by

$$\theta = T\left(\frac{p_0}{p}\right)^{\frac{R}{C_p}} \tag{2.6}$$

where C_p is the specific heat at constant pressure and p_0 is a constant reference pressure, commonly chosen to be mean sea-level pressure. It is worth noting here that by definition the wind velocity makes no contribution to the stationary state and is associated solely with the eddy components of the atmosphere. With the cancellation of small terms and the approximation of the stationary state density and potential temperature by mean values, we can 'subtract out' the stationary state and define the quasi-geostrophic hydrostatic equation

$$f_0\frac{\partial\psi}{\partial z} = b, \tag{2.7}$$

where

$$b = g\frac{\theta_e}{\theta_0} \tag{2.8}$$

is a buoyancy parameter, the stream-function $\psi = p/f_0\rho_0$ is a scaled pressure perturbation and ρ_0 and θ_0 are the mean values of the stationary state density and buoyancy. The quasi-geostrophic hydrostatic equation, describes the balance of gravitational and vertical pressure gradient forces for the eddy components of the atmospheric state. Taking mean values of the stationary state density and potential temperature is justifiable in this equation on the grounds that observations of the atmosphere indicate that the magnitude of variations in these quantities are small by comparison to the absolute magnitude.

Whilst deviations in the magnitude of the stationary state density and potential temperature are dynamically unimportant, the gradient of these deviations *does* play an important role in the dynamical evolution of the eddy components of the state. It is the nature of the vertical stratification of the stationary state that defines the restoring force experienced by air masses displaced in the vertical direction; i.e. prevents the appearance of convective instability by enforcing the condition that density is a decreasing function of height. For the quasi-geostrophic equations this stability property is contained in the static stability parameter

$$N^2 = \frac{g}{\theta_s}\frac{\partial \theta_s}{\partial z}, \tag{2.9}$$

which we shall take to have the constant value N_0^2.

The observed propagation speed of the mid-latitude cyclones we wish to represent are much smaller than the speed of sound ($\sim 330 ms^{-1}$). Since we do not require to represent disturbances which travel close to the speed of sound we may neglect the dynamical effects of density gradients and assume that the atmosphere is incompressible; i.e. the density is constant in space and time. It should be pointed out here that in the quasi-geostrophic equations the effect of the vertical stratification of the stationary state density is retained implicitly in the static stability parameter and the effect of the vertical density gradients in the eddy components of the state are retained implicitly in the definition of the Quasi-Geostrophic hydrostatic equation. Since mass is conserved in the atmosphere, incompressibility enforces the condition that the net flow of mass into a volume must be zero and therefore the wind must be non-divergent. Zero divergence can be expressed mathematically as

$$\nabla_h \cdot \boldsymbol{v} + \frac{\partial w}{\partial z} = 0, \tag{2.10}$$

where $\boldsymbol{v} = u\boldsymbol{i} + v\boldsymbol{j}$ is the horizontal wind velocity, w is the magnitude of the vertical wind velocity and

$$\nabla_h = \frac{\partial}{\partial x}\boldsymbol{i} + \frac{\partial}{\partial y}\boldsymbol{j}$$

is the horizontal gradient operator.

In the atmosphere, the acceleration of air masses due to horizontal pressure gradients is balanced by two accelerations. Firstly, by the Lagrangian acceleration; i.e. the change in wind velocity. Secondly, by the Coriolis acceleration which occurs due to the use of a rotating frame of reference in the equations. The flow is said to be in geostrophic balance if the pressure gradient acceleration is equal and opposite to the Coriolis acceleration. The horizontal wind can be separated into a geostrophically balanced component, the geostrophic wind $\boldsymbol{v}_g$, and an unbalanced component, the ageostrophic wind $\boldsymbol{v}_{ag}$. The geostrophic wind is purely horizontal and is defined by

$$\boldsymbol{v}_g = \boldsymbol{k} \times \nabla_h \psi. \tag{2.11}$$

The geostrophic wind is non-divergent. Since the total wind field is non-divergent (Equation (2.10)) the sum of the ageostrophic and vertical wind must also form a non-divergent circulation.

For geostrophically and hydrostatically balanced flows, there exists a thermal wind balance relationship

$$\frac{\partial \boldsymbol{v}_g}{\partial z} = \frac{1}{f_0}\boldsymbol{k} \times \nabla_h b, \tag{2.12}$$

which relates horizontal gradients of potential temperature[2], b, to vertical gradients of the

[2]N.B. the buoyancy parameter is a scaled potential temperature

geostrophic wind. For example a negative meridional gradient of potential temperature induces a positive vertical variation in the zonal geostrophic wind. As we shall see the flow in the mid-latitudes is dominated by the geostrophic wind. Due to the large meridional temperature gradient (warm at the equator, cold at the poles) the flow in mid-latitudes is dominated by a zonal wind component which increases in magnitude with height.

The Rossby number

$$R_o = \frac{\mathscr{U}}{f_0 \mathscr{L}} \tag{2.13}$$

gives an estimate of the typical ratio of the magnitude of the Lagrangian acceleration to the Coriolis acceleration. When the Rossby number is small the flow is close to geostrophic balance. For the mid-latitudes the Coriolis parameter has a value $f_0 = 10^{-4} s^{-1}$. The typical velocity and length scales of the cyclones we wish to depict are $\mathscr{U} \sim 10 m s^{-1}$ and $\mathscr{L} \sim 10^3 km$. With these values $Ro \sim 0.1$ and the flow is nearly in geostrophic balance and the geostrophic wind dominates. Since the flow is dominated by the geostrophic wind we can ignore advection of the eddy components of the state by the ageostrophic and vertical winds; therefore the application of the Lagrangian time derivative to the eddy components of the state can be approximated by the geostrophic Lagrangian time derivative

$$D_g = \frac{\partial}{\partial t} + \boldsymbol{v}_g \cdot \nabla_h. \tag{2.14}$$

For adiabatic motion, the internal energy of the system remains constant, and entropy is conserved. For the atmosphere, this is equivalent to assuming that potential temperature is conserved following the flow. Using the approximation of the Lagrangian time derivative by the quasi-

geostrophic Lagrangian time derivative, potential energy is only approximately conserved. This approximate conservation is enforced by the thermodynamic equation

$$D_g b + N_0^2 w = 0. \tag{2.15}$$

The second term ($N_0^2 w$) of this conservation law stems from the advection of the stationary state potential temperature by the vertical wind. It is assumed that the magnitude of this vertical advection is too small to significantly alter the properties of the stationary state.

On an $f - plane$ the quasi-geostrophic horizontal momentum Equation is defined

$$D_g \boldsymbol{v}_g + f_0 \boldsymbol{k} \times \boldsymbol{v}_{ag} = 0. \tag{2.16}$$

Several terms have been neglected in this equation, most notably the time derivative of the ageostrophic wind. The 'neglect' of these terms is only valid if the Rossby number is small.

Applying $\nabla_h \times$ to the quasi-geostrophic horizontal momentum Equation (2.16) and taking the vertical derivative of the Thermodynamic Equation (2.15), we can combine these two equations to form

$$D_g \left(\frac{1}{f_0} \nabla_h \times \boldsymbol{v}_g + \frac{1}{N_0^2} \frac{\partial b}{\partial z} \right) = -\nabla \cdot \left(\boldsymbol{v}_{ag} + w \boldsymbol{k} \right). \tag{2.17}$$

Since the divergence of the combined ageostrophic and vertical wind is zero we may define a quasi-geostrophic potential vorticity

$$q = \nabla_h \times \boldsymbol{v}_g + \frac{f_0}{N_0^2} \frac{\partial b}{\partial z} \tag{2.18}$$

which is conserved following the geostrophic flow. The first term on the right hand side of Equa-

tion (2.18) is the vertical component of the vorticity of the geostrophic wind. The second term on the right is the vertical gradient of the potential temperature, b. The conservation of potential vorticity expresses the fact that positive tendencies of vorticity (i.e. deepening of low pressure systems) are associated with negative tendencies in potential temperature gradient (i.e. warming at upper levels and cooling at the surface). For negative tendencies in vorticity the opposite is true so that the development of high pressure systems is associated with cooling above and heating at the surface. From a physical point of view this heating and cooling is induced by the transport of warm air from the surface (for low pressure systems) and cold air from upper levels (for high pressure systems) via the circulation of combined ageostrophic and vertical winds.

From a mathematical point of view the ageostrophic-vertical circulation plays only a diagnostic role in the quasi-geostrophic equations and the evolution of the flow is determined by the conservative advection of Quasi-Geostrophic potential vorticity by the geostrophic wind. i.e.

$$D_g q = 0. \tag{2.19}$$

The quasi-geostrophic potential vorticity can be written as a Laplacian function of the quasi-geostrophic stream-function

$$q = \nabla_h^2 \psi + \frac{f_0^2}{N_0^2} \frac{\partial^2 \psi}{\partial z^2}. \tag{2.20}$$

With suitable boundary conditions, the potential vorticity can be inverted to obtain the stream-function field; Hoskins et al. (1985). Once the stream-function is known, every aspect of the flow can be determined. The quasi-geostrophic equations therefore comprise a simple prognostic Equation (2.19) which along with suitable (usually time evolving) boundary conditions and the Laplacian Equation (2.20) can be used to integrate a chosen initial condition forward in time.

Despite the apparent simplicity of the equations non-linearities associated with the advection of potential vorticity by the geostrophic wind (which depends on the potential vorticity) have so far prevented the discovery of an analytical solution. To make the Quasi-Geostrophic Equations solvable by analysis requires further simplifications. Eady (1949) defined a linearised formulation of the Quasi-Geostrophic equations which allowed both analytical solutions and the retention of the essential dynamics of cyclogenesis. In the next section we shall introduce the two dimensional formulation of Eady's original equations.

2.3 The Two-dimensional Eady Model

In this section, the formulation of the 'Two-Dimensional Eady Equations' will be described. The 2D Eady Equations are based on a linearisation of the quasi-geostrophic equations about the time-invariant background state first proposed by Eady (1949). The background state consists of constant (in space and time) meridional potential temperature gradient

$$\frac{\partial \bar{b}}{\partial y} = -f_0 \Lambda, \tag{2.21}$$

where Λ is a constant. The over-bar is used to denote a time-invariant background state variable. It must be stressed that this time-invariant background state is connected with the eddy components of the quasi-geostrophic equations and is not part of the stationary hydrostatic state discussed in the previous section. This time invariant temperature gradient is an approximation to the sustained differential solar heating which supplies the atmosphere with its thermal energy. Through the thermal wind balance relationship (Equation (2.12)) a vertically sheared zonally orientated

geostrophic flow

$$\bar{u}_g = \Lambda z, \tag{2.22}$$

is induced. Since the constant Λ defines the vertical wind-shear it is referred to as the wind-shear parameter. This background state is shown schematically in Figure 2.1.

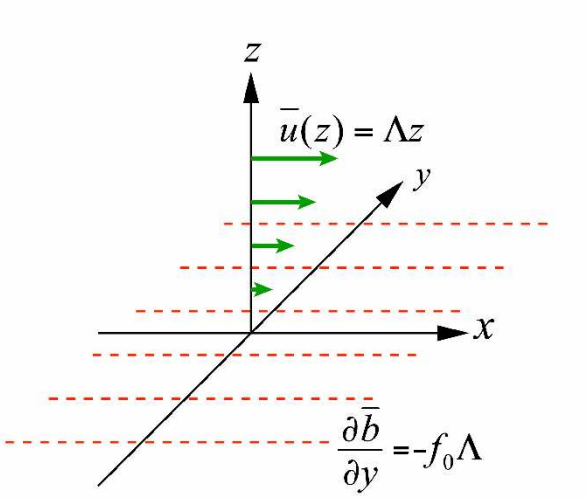

Figure 2.1 *The Eady background state*

To obtain the 2D-Eady Equations the following boundary conditions are applied. Rigid surfaces are assumed to exist on the upper and lower boundaries, $z = Z$ and $z = 0$ respectively. The assumption of rigid upper and lower surfaces implies that the vertical velocity w vanishes at $z = 0$ and $z = Z$. Periodic boundary conditions are assumed in the zonal direction, such that $x = 0 \equiv x = X$. The meridional coordinate is effectively removed from the dynamical equations

by assuming that the meridional wavelength of perturbations to the background flow is zero; i.e.

$$\frac{\partial \psi'}{\partial y} \equiv 0, \quad \begin{cases} x \in [0, X] \\ y \in (-\infty, \infty) \\ z \in (0, Z) \\ t \in [0, \infty) \end{cases}, \tag{2.23}$$

where the dash denotes a perturbation to the background state. Making this assumption is roughly equivalent to assuming the zonal scale of perturbations to the background flow is much larger than the meridional scale and means that solutions to the 2D Eady model are 'technically' solutions to the full non-linear Quasi-Geostrophic Equations (Green (1960)). One effect of this assumption is that flow of wind associated with perturbations to the Eady background state exists only in the meridional direction.

With the above boundary conditions the evolution via Equation (2.19) of potential vorticity perturbations to the background flow can be written as

$$\left\{ \frac{\partial}{\partial t} + \Lambda z \frac{\partial}{\partial x} \right\} q' = 0, \quad \begin{cases} x \in [0, X] \\ y \in (-\infty, \infty) \\ z \in (0, Z) \\ t \in [0, \infty) \end{cases}, \tag{2.24}$$

where the dash denotes a perturbation perturbation to the Eady background state. The definition

of potential vorticity given in Equation (2.20) becomes

$$q' = \frac{\partial^2 \psi'}{\partial x^2} + \frac{f_0^2}{N_0^2}\frac{\partial^2 \psi'}{\partial z^2} \quad \begin{cases} x \in [0, X] \\ y \in (-\infty, \infty) \\ z \in (0, Z) \\ t \in [0, \infty) \end{cases} . \tag{2.25}$$

Once the potential vorticity can be inverted to obtain the stream-function the model state can be fully determined.

With the vanishing of vertical velocity w at $z = 0$ and $z = Z$ the thermodynamic Equation (2.15) becomes

$$\left\{ \frac{\partial}{\partial t} + \Lambda z \frac{\partial}{\partial x} \right\} \frac{\partial \psi'}{\partial z} - \Lambda \frac{\partial \psi'}{\partial x} = 0 \quad \begin{cases} x \in [0, X] \\ y \in (-\infty, \infty) \\ z = 0, z = Z \\ t \in [0, \infty) \end{cases} , \tag{2.26}$$

on the upper and lower boundaries. This new thermodynamic equation defines the evolution of normal derivative upper and lower boundary conditions required for the inversion of potential vorticity.

To ensure that the inversion of potential vorticity subject to periodic and derivative boundary

conditions is unique, a further integral constraint

$$\int_0^X \psi' dx = 0, \quad \begin{cases} x \in [0, X] \\ y \in (-\infty, \infty) \\ z \in (0, Z) \\ t \in [0, \infty) \end{cases}, \tag{2.27}$$

is used. This constraint is equivalent to imposing the condition that all non-zero solutions must be composed of zonal waves.

Equations (2.23) to (2.27) form a complete set which can be used to determine the evolution of 'quasi-two-dimensional' perturbations to the Eady background state. In all that follows primes will be dropped from perturbation quantities and all 'un-barred' variables will be assumed perturbations to the Eady background state. The subscript g will be dropped from the geostrophic wind, since the ageostrophic wind makes no explicit appearance in the Eady Equations. Also since the solutions to Equations (2.23) to (2.27) are identical at all meridional locations, the meridional coordinate y will be removed from the domain of dependence and solutions will be treated as two-dimensional.

2.4 Dynamical behaviour of solutions to the 2D Eady Equations

2.4.1 Form of the general solution to the Eady Equations

The 2D Eady Equations outlined form an initial boundary value problem to which the solution is fully determined if the initial stream-function field is known at every point in space. As was noted in the previous section solutions to the equations are wave-like in the zonal direction. We shall

use $k_n = 2n\pi/X$ to denote the zonal wavenumber of solutions where X is the zonal extent of the domain and $n > 0$ is an integer which we shall call the wave index. Since at each time point the stream-function field must be a solution to the inversion of potential vorticity the total solution to the equations comprises a particular (non-zero potential vorticity) solution of the form

$$\psi_p(x, z, t) = \mathscr{F}(z, t)e^{ik_n x} \tag{2.28}$$

where $\mathscr{F}$ is a function of height and time, and a homogeneous (zero potential vorticity) solution of the form

$$\psi_h(x, z, t) = \{\mathscr{A}(t)cosh(k_n z) + \mathscr{B}(t)sinh(k_n z)\}\, e^{ik_n x} \tag{2.29}$$

where $\mathscr{A}$ and $\mathscr{B}$ are functions of time only.

The original solutions of Eady (1949) consisted of only the zero potential vorticity component of the solution, which depends only on the potential temperature structure on the upper and lower boundaries. The zero potential vorticity solutions form a discrete set of normal modes (two for each wavenumber) the behaviour of which shall be discussed in more detail later. Pedlosky (1964) noted that the normal modes did not form a full set and therefore the contribution from the 'continuum of modes' associated with a non-zero potential vorticity field must be taken into account, in order to fully describe the behaviour of an arbitrary initial disturbance. A full general solution to the Eady Equations can be found in Pedlosky (1964), but it is not our intention to give any formal mathematical discussion of this solution other than noting its dependence on both normal modes and 'continuum modes'. In the following sections we shall discuss the structure and behaviour of the normal modes; then give a a brief explanation of the structure and behaviour of the continuum modes; we shall then discuss the behaviour of the untilting plane-wave particular

solution found in Farrell (1984); and finally we will discuss the effect of resonance between the normal modes and the interior potential vorticity structure.

2.4.2 The Normal Modes of the 2D Eady Equations

The original solutions of Eady (1949) to the Eady Equations contained only the homogeneous zero potential vorticity component of the solution defined by Equation (2.29). The solutions of Eady (1949) are of the form

$$\psi_h(x,z,t) = \left\{ \sinh\left(\frac{N_0}{f_0}k_n z\right) - \frac{N_0}{f_0\Lambda}k_n c \cosh\left(\frac{N_0}{f_0}k_n z\right) \right\} e^{ik_n(x-ct)} \tag{2.30}$$

where the *complex* phase speed is given by

$$c = \frac{Z\Lambda}{2} \pm \frac{f_0\Lambda}{Nk_n}\sqrt{\left\{\frac{NZ}{2f_0}k_n - \coth\left(\frac{NZ}{2f_0}k_n\right)\right\}\left\{\frac{NZ}{2f_0}k_n - \tanh\left(\frac{NZ}{2f_0}k_n\right)\right\}}. \tag{2.31}$$

The real component of solutions of this type are the normal modes of the Eady model. Since the second term of Equation (2.31) can be positive or negative there are two normal modes for each zonal wavenumber. The vertical structure of the normal mode depends on the zonal wavenumber but is independent of time. The phase speed of the normal modes is given by the real component c_r of c and an exponential amplification factor is given by $k_n c_i$ where c_i is the imaginary component of c.

The real and imaginary parts of the phase speed (normalised by ΛZ) are shown in Figures 2.2A and 2.2B respectively. For wavenumbers greater than the critical 'short-wave cutoff' value $k_c = 2.4 f_0/N_0 Z$, c is entirely real and there are two distinct real phase speeds for each wavenumber and the normal modes are non-amplifying. Since their amplitude does not change with time

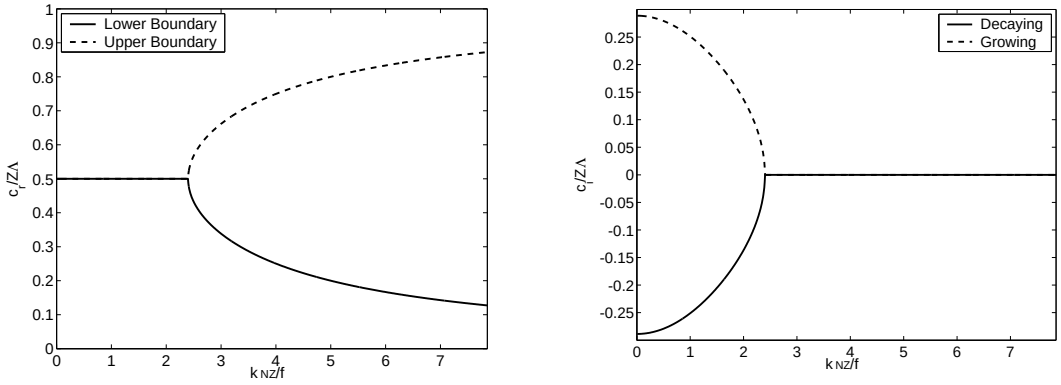

A B

Figure 2.2 *A: Real Normal mode phase speed. B: Imaginary Normal mode phase speed.*

these short-wave normal modes are referred to as the neutral modes of the Eady model. For wavenumbers smaller than the 'short-wave cutoff' c is complex and both normal modes have real phase speed $c_r = H\Lambda/2$ and are exponential growing or decaying in time depending on the sign of the imaginary phase speed. Since the background zonal wind varies in height as $u(z) = \Lambda z$, the real phase speed of the normal modes corresponds to the background zonal wind-speed at the height c_r/Λ. The height at which the background zonal wind-speed is equal to the normal mode phase speed is called the 'steering level' of the normal mode. From Equation (2.31) it can easily be verified that the phase speed tends to background zonal wind speed on the upper and lower boundaries as k_n tends to infinity; hence the steering levels tend to $z = 0$ and $z = Z$.

Figures 2.3A and 2.3B show the height variation of the mean squared stream-function amplitude

$$\bar{\psi^2}(z, k_n) = \int_0^X \psi_{k_n}^2(z, x)dx \Big/ \int_0^Z \int_0^X \psi_{k_n}^2(z, x)dxdz \ , \tag{2.32}$$

of the normal modes as a function of wavenumber; the dashed and solid lines show the normal mode steering level. For the neutral modes, the amplitude is concentrated on the boundary nearest to the steering level height; Therefore the neutral modes may be thought of as being either the

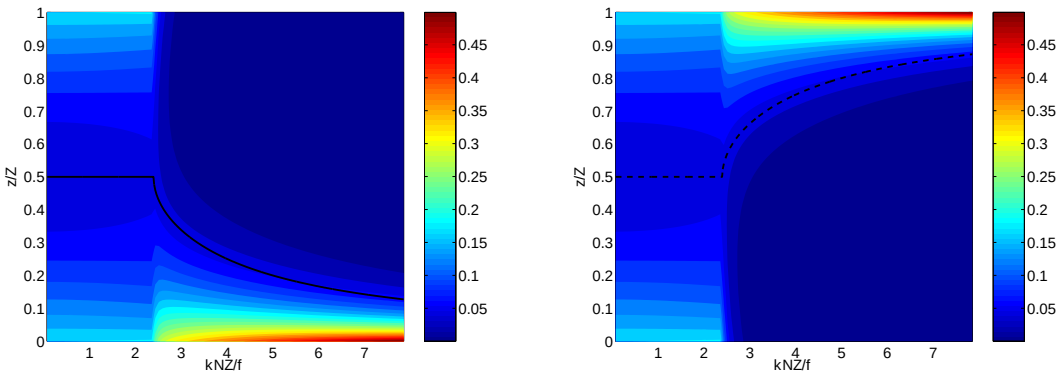

A B

Figure 2.3 *Normal mode mean squared amplitude (Equation (2.32)) as a function of height and zonal wavenumber. A: Decaying mode/lower boundary neutral mode. B: Growing mode/upper boundary neutral mode. Figures are plotted from vertically discretised continuous normal modes.*

upper or the lower boundary neutral mode. One noticeable feature of the neutral modes is that the amplitude resides predominantly between the steering level and the boundary. As the wavenumber increases the steering level moves closer to the boundary and the normal mode amplitude is contained in an increasingly shallow region at the boundary.

Unlike the neutral modes, the unstable/stable mode's amplitude is evenly distributed between both boundaries. Rather than referring to the upper or lower boundary mode, the two components of the phase speed refer to the growing and decaying modes. For reference examples of the stream-function structure of the growing ($k_n = \pi NZ/2f_0$), decaying ($k_n = \pi NZ/2f_0$) and lower boundary neutral ($k_n = 7\pi NZ/8f_0$) modes are shown in Figures 2.4A, 2.4B, 2.4C respectively. The upper boundary neutral mode is not shown as this is merely a reflection of the lower boundary neutral mode about the line $z = Z/2$. The growing neutral modes have a westward phase tilt with height and the decaying modes have a eastward tilt with height. The magnitude of these phase tilts decreases with increasing wavenumber.

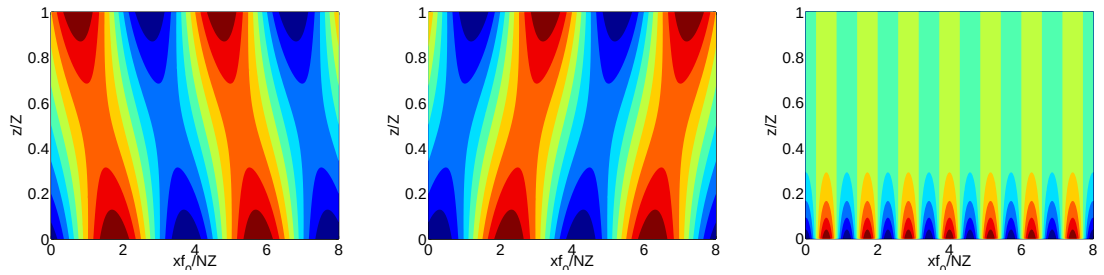

A B C

Figure 2.4 *The streamfunction fields associated with A: Growing mode. B: Decaying mode. C: Neutral mode. The figures are generated by discretising the continuous normal mode.*

2.4.3 The 'Continuum Modes' of the Eady Equations

The normal modes of the Eady model form a discrete set of perturbations associated with the potential temperature structure on the upper and lower boundaries. Pedlosky (1964) noted that since there are only two normal modes for each zonal wavenumber, the normal modes do not form a full set and therefore cannot be used to represent an arbitrary initial disturbance. In order to be able to represent an arbitrary initial disturbance the contribution from the potential vorticity structure in the interior must be taken into account. Using interior potential vorticity perturbations of the form

$$q(x,z,t) = \mathscr{Q}\delta(z-z_0)e^{ik_n(x-\Lambda z_0 t)}, \tag{2.33}$$

where $\mathscr{Q}$ is a constant wave-amplitude,

$$\delta(z-z_0) = \begin{cases} 0, & z \neq z_0, \\ 1, & z = z_0, \end{cases} \tag{2.34}$$

is the Dirac delta function and $z_0 \in (0, Z)$ is a constant, Pedlosky (1964) solved the 2D Eady equations in generality. The solution given by Pedlosky (1964) is an unwieldy equation and is not repeated here; however we shall discuss the some of the qualitative features.

Equation (2.33) defines a zonally orientated potential vorticity travelling wave residing solely at height z_0. The phase speed of the potential vorticity wave is equal to the background zonal wind speed $u(z_0) = \lambda z_0$ at the height z_0. The stream-function field associated with the potential vorticity wave must satisfy the boundary conditions. For a single potential vorticity wave Pedlosky (1964) found that he could write the solution as a summation of three separate time dependent components. The first two of these components are constant multiples of the Eady normal modes defined by Equations (2.30) and (2.31); where the constant is defined by the projection of the initial condition onto the respective normal mode. The third term is the particular solution associated with the potential vorticity wave. This particular solution comprises a vertically distributed stream-function field travelling with the phase speed of the potential vorticity wave. The full solution to the problem is formed from an infinite sum of the potential vorticity wave solutions. The stream-function fields associated with potential vorticity waves of the form of Equation (2.33) are collectively known as the continuum modes of the Eady model. The phase of the continuum modes is constant in height. The phase speed of each continuum mode is equal to the phase speed of the potential vorticity wave with which it is associated.

A notable feature of the continuum modes is the difference in structure of the low and high wavenumber modes. To demonstrate this difference Figures 2.5A and 2.5B show the variation of mean squared stream-function amplitude (Equation (2.32)) with height (y-axis) as a function of zonal wavenumber (x-axis) for single potential vorticity waves located at $z_0 = Z/2$ and $z_0 = 3Z/4$ respectively. For reference the dashed and solid black lines show the steering level

height and the dotted black line shows the location of the potential vorticity wave. When the potential vorticity wave is located in the centre of the domain (Figure 2.5A) the low wavenumber continuum modes have equal amplitude maxima on the upper and lower boundaries, whereas the high wavenumber modes have a single amplitude maxima at the location of the potential vorticity wave. The 'intermediate' wavenumbers have three maxima one located in the centre and one on each boundary. When the location of the potential vorticity wave is moved to $z_0 = 3Z/4$ (Figure 2.5B) those wavenumbers for which the potential vorticity wave remains sufficiently below the steering level still have amplitude maxima located at the position of the potential vorticity wave; whereas those wavenumbers for which the potential vorticity wave is close to or above the upper boundary steering level have maximum amplitude on the upper boundary.

It is interesting to note that at the high wavenumber end of the zonal spectrum the continuum modes associated with a potential vorticity wave located near the centre of the domain have negligible amplitude above (below) the upper (lower) boundary steering level; whereas the amplitude of normal modes (Figure 2.3) resides almost exclusively above (below) the upper (lower) boundary steering level. The result of this disparity of structure is that for high wavenumbers the potential vorticity waves located near the centre of the domain are 'dynamically isolated' from the normal modes. By contrast at the low wavenumber end of the zonal spectrum the amplitude of both the normal modes and the continuum modes is concentrated on the boundaries. This is a point that we shall return to in our analysis of the singular vector structure of the Eady model.

With the inclusion of the continuum modes in the solution to the 2D Eady Equations there exist several growth mechanisms additional to the exponential growth associated with the unstable normal modes. These mechanisms are growth by unshielding/untilting of potential vorticity, growth by the unmasking of normal modes which are initially masked by continuum modes and growth

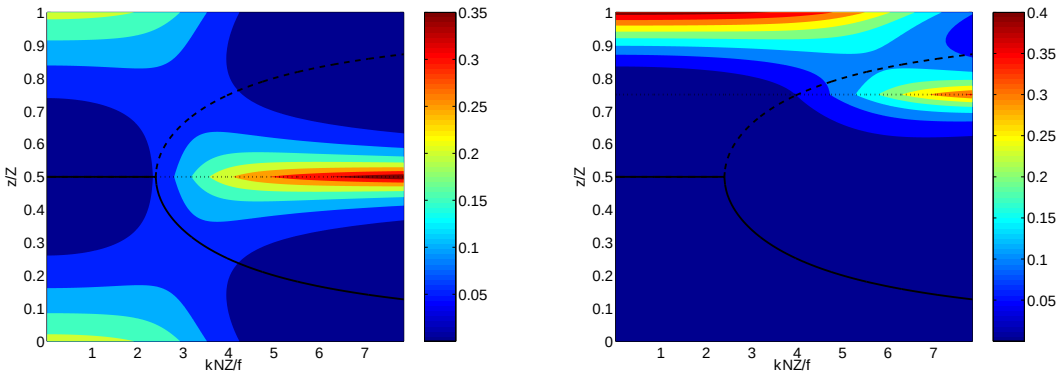

A B

Figure 2.5 *Continuum mode streamfunction-squared amplitude as a function of height and wavenumber. A: For a potential vorticity wave residing at $z/Z = 0.5$. B: For a potential vorticity wave residing at $z/Z = 0.75$. Figures are plotted using discretised continuous continuum modes taken from the solution given in Pedlosky (1964).*

by the resonance of the normal modes with the continuum mode located close to the steering level. Starting with potential vorticity untilting/unshielding the properties of these three amplification mechanisms will be outlined in the subsequent three sections of this chapter.

2.4.4 Potential Vorticity Untilting/Unshielding

Streamfunction amplification via untilting/unshielding relies on the principle of constructive and destructive superposition of streamfunction waves. For example two superposed streamfunction waves with the same wavenumber will sum to give a larger amplitude wave if they are in phase. By contrast the two waves will cancel to give a lower amplitude wave if they are out of phase. As we have seen in our analysis of the continuum modes of the Eady model, a potential vorticity wave located at a particular height induces a stream-function field throughout the domain. The phase speed of this stream-function field is equal to that of the potential vorticity wave. Since

the phase speed of the potential vorticity waves varies with height, the phase speed of superposed streamfunction fields associated with potential vorticity waves on different levels differs. Due to this difference in phase speed, initially out of phase streamfunction fields can be brought into phase by the advection of the potential vorticity. As the streamfunction fields are brought into phase they become increasingly constructively superposed, leading to amplification. This growth by superposition is encapsulated in the untilting solution of Farrell (1984).

Farrell (1984) solved the Eady equations for the particular initial condition[3]

$$\psi(x,z,0) = e^{i(kx+m_0 z)} = e^{ik(x+a_0 z)}, \tag{2.35}$$

where k is the zonal wavenumber, m_0 is the initial vertical wavenumber and $a_0 = m/k$. The initial condition given in Equation (2.35) describes uniform amplitude wave-field in which the phase of the zonal waves is constant along planes which tilt with an angle $\phi_0 = -\tan^{-1} a_0$ to the vertical. Since the parameter $a_0 = m/k$ defines the initial tilt angle of the planes of constant phase we shall call this the *initial tilt*. Following Orr (1907), Farrell (1984) found a particular solution to the interior potential vorticity equation of the form

$$\psi_p(x,z,t) = \frac{(1+a_0^2/S)}{[1+(a_0-\Lambda t)^2/S]} e^{ik(x+[a_0-\Lambda t]z)} = \frac{(1+a_0^2/S)}{[1+a^2(t)/S]} e^{ik(x+a(t)z)}, \tag{2.36}$$

where $S = N_0^2/f_0^2$ and $a(t) = a_0 - \Lambda t$. We shall call $a(t)$ the *tilt*. For a positive initial tilt the evolution described by Equation (2.36) may be summarised as follows: The initial plane wave structure has a westward tilt with height; over time the tilt reduces due to differential advection

[3]Since we are dealing with the 2D Eady model the meridional coordinate has been omitted from Farrell (1984)'s solution.

by the shear flow; along with this reduction in tilt the amplitude increases as per

$$|\psi| = \frac{(1 + a_0^2/S)}{[1 + (a_0 - \Lambda t)^2/S]} = \frac{(1 + a_0^2/S)}{[1 + a^2(t)/S]}; \tag{2.37}$$

the amplitude reaches a maximum value of $1 + a_0^2/S$ at time $t = a_0 S/\Lambda$; at $t = a_0 S/\Lambda$ the planes of constant phase are parallel to the vertical; beyond $t = a_0 S/\Lambda$ the plane waves begin to tilt eastwards and the amplitude decays with time.

The reason for the amplification of the untilting plane-wave can be interpreted by considering the associated potential vorticity field. The particular solution (2.36) is associated with a tilted potential vorticity plane-wave field of the form

$$q_p(x, z, t) = -k^2(1 + \frac{a_0^2}{S})e^{ik(x+a(t)z)}. \tag{2.38}$$

This potential vorticity field can be viewed as the infinite sum of potential vorticity waves of the form Equation (2.33). Each of these potential vorticity waves induces a vertically distributed streamfunction field with uniform phase. When the potential vorticity waves on different levels are out of phase (i.e. the plane-waves are tilted) the streamfunction fields associated with these potential vorticity waves are also out of phase leading to destructive superposition. As the potential vorticity waves are brought into phase by the shear-flow the streamfunction function fields are also brought into phase leading to constructive superposition. On a domain of infinite vertical extent the amplitude of a streamfunction field associated with a potential vorticity wave would decay with vertical distance from the potential vorticity 'source'; Bishop and Thorpe (1994). In this infinite domain case the behaviour of the solution in time could be entirely characterised by the untilting potential vorticity plane-waves and the local interactions between the streamfunction fields associated with the potential vorticity structure on adjacent vertical levels. However

the structure of the continuum modes is not in general consistent with that of potential vorticity waves on an infinite domain and the effect of the upper and lower boundaries on the behaviour of the solution must be taken into account. In order to satisfy the boundary conditions a contribution from the homogeneous component of the solution is required. The full solution takes the form

$$\psi(x,z,t) = \psi_p(x,z,t) + (\mathscr{A}(t)cosh(k/z) + \mathscr{B}(t)sinh(kz))\, e^{ikx}, \tag{2.39}$$

where $\mathscr{A}(t)$ and $\mathscr{B}(t)$ are chosen to satisfy the particular initial condition; Farrell (1984). As we shall see in the following chapter, the presence of this homogeneous solution plays an important role in determining the structure of the singular vectors of the Eady model. It is worth noting that unlike the continuum mode solutions of Pedlosky (1964), the behaviour of the homogeneous component of the plane-wave streamfunction solution is not trivially related to that of Eady's normal mode solutions.

2.4.5 Modal Unmasking

Modal unmasking (Morgan and Chen (2002)) is similar to potential vorticity unshielding in that it relies on the constructive and destructive superposition of the streamfunction fields associated with different modes. In modal masking the streamfunction field associated with a normal mode is 'masked' by the superposed streamfunction fields associated with the continuum modes. Due to the difference in phase speed between the continuum modes and normal modes, the normal mode is 'revealed'. This revealing can be caused either because the net streamfunction field of the continuum modes decays away due to potential vorticity untilting or because the difference in phase speed of the normal and continuum modes means that the, initially out of phase, normal and continuum modes are brought into phase.

2.4.6 Neutral Mode Resonance

Neutral mode resonance is somewhat akin to the exponentially amplifying resonance of the long-wave normal modes. Neutral mode resonance occurs, however, for wavenumbers greater than the short-wave cutoff. The essential component of neutral mode resonance is that a potential vorticity wave resides at the steering level of the neutral normal mode. When this occurs the interaction between the continuum and normal mode leads to linear amplification of the potential temperature wave which is sustained indefinitely; Thorncroft and Hoskins (1990). For discrete numerical models exact neutral mode resonance can only occur if the steering level height for a particular wavenumber is co-located with one of the models vertical levels and in practice only approximate resonances are likely; Chang (1992). Unlike the potential vorticity unshielding and modal unmasking mechanisms, neutral mode resonance (and normal mode resonance) lead to indefinite growth.

CHAPTER 3

The Singular Vectors of The 2D Eady model

3.1 Introduction

The use of singular vector decompositions of linearised dynamical models has become common in meteorological centres; for example in the generation of perturbations for ensemble forecasts Molteni et al. (1996). Singular vectors have come to be associated with the notion of 'optimal growth' over finite time intervals; e.g. Buizza et al. (1993). The use of singular vectors to obtain optimally amplifying perturbations, rather than considering normal modes/eigenvectors, lies in the fact that since the linear operator associated with small perturbation dynamics in the atmosphere are not symmetric, their eigenvectors are not orthogonal and therefore a linear combination of eigenvectors may achieve finite time amplification greater than that implied by the largest eigenvalue; Farrell and Ioannou (1996). The rapid, but transient amplification of singular vectors has lead them to be associated with rapidly growing forecast errors [e.g. Farrell (1990), Lorenz (1965)] and the initial stages of rapid cyclogenesis [e.g. Farrell (1989)].

In this chapter the singular vector structure of the 2D Eady model will be described. The work presented in this chapter follows on from that found in Frame et al. (2005). The singular vectors of the Eady model with rigid upper and lower boundaries have been presented previously by Mukougawa and Ikeda (1994), Morgan (2001), Morgan and Chen (2002) and Kim and Morgan (2002). Several further related studies on the subject of optimal perturbations/singular vectors

exist. Fischer (1998) discusses the optimally growing *modal* structures of the Eady model with uniform potential vorticity. De Vries and Opsteegh (2005) discuss the singular vectors of the Eady model without rigid upper boundaries. The motivation behind the present discussion of this subject is twofold. Firstly this chapter serves to illustrate properties of the Eady singular vectors which will prove relevant to later discussions of adaptive observations. Secondly all previous published discussions have approached the problem from a purely optimal growth perspective, limiting their discussions to the growth mechanism of the first singular vector. In our treatment of the subject we take a predictability standpoint, analysing the effect of the dynamical growth mechanisms on the structure of the full spectrum of singular vectors.

To be concise, we shall focus our discussions on the singular vectors computed for a short and intermediate integration length. For the short integration a integration length of $\tau = 1.73N_0/f_0\Lambda$ is used. This integration length is approximately $12h$ with the parameters assumed in the model. For the intermediate integration a time-scale $\tau = 6.91N_0/f_0\Lambda$, corresponding to an integration of approximately $48h$, is used. The choice to focus on these two particular integration lengths is made as they are characterised by distinct dynamical processes. For the short forecast untilting is the dominant amplification mechanism and explains much of the structure and behaviour of the singular vectors. For the intermediate integration length modal masking is significant and the singular structure deviates from that expected from the untilting mechanism although untilting is still important to the singular vector. In a sense we can identify two amplification regimes: the untilting/unshielding regime which exists for short integration times; and the modal unmasking regime which exists at longer integration times.

The concept of two dynamical regimes for leading singular vector growth in the European Centre for Medium-Range Weather Forecasting model has been proposed previously by Hoskins et al.

(2000). Hoskins et al. (2000) attribute the second regime to long term normal mode-like growth due to coupling of potential vorticity with the surface, rather than to transient growth, which can be interpreted as a modal unmasking effect. Hoskins et al. (2000) propose the transition point between the two regimes be defined using 'the two dimensional quasi-geostrophic expression for the vertical group velocity of Rossby waves', with the second regime occuring when the singular vector energy has propagated to the upper boundary. For the 2D Eady model, in which the meridional potential vorticity gradient is zero, there is no Rossby wave motion and such a definition is not applicable. In contrast to Hoskins et al. (2000) we find that the transition from the unshielding regime occurs roughly when the integration length is sufficient for a potential vorticity wave located near the steering level to achieve a π phase transition relative to the normal mode. As we shall see, a further implication of this requirement that short wavelength perturbations will enter the modal unmasking regime at shorter integration lengths than long wavelength perturbations. Whilst it would be interesting to investigate further the links/contradictions between these two interpretations of the 'regimes of singular vector growth', such an investigation will not be included in this thesis.

The chapter is divided into three sections. In the first section, we outline the singular vector computation. In the second section we examine the implications of plane-wave untilting and modal unmasking growth mechanisms for singular vector growth, by considering the properties of continuous solutions to the Eady model. In the third section, we examine the singular vectors of the Eady model themselves and seek to relate these to the properties discussed in the first section.

By examining the functional form of the plane-wave solution of Farrell (1984), several properties of the untilting mechanism related to singular vectors are identified. Firstly, the optimal initial tilt for streamfunction amplification over a given finite time interval is identified. It is noted that,

for short time intervals, this optimal tilt is larger than that which would render the plane waves completely vertical within that time interval. By determining the necessary condition for orthogonality between plane-waves, it is found that the difference in tilt between orthogonal plane waves is smaller for high wavenumbers than for low wavenumbers. The similarity of the initial tilts of orthogonal planes at high wavenumbers implies that the finite time amplification of orthogonal plane waves is more similar at high wavenumbers than low wavenumbers. This means that, when the amplification of singular vectors other than the first is taken into account, the high wavenumbers will be dominant. Although they are not of exact plane-wave form it is found that the $12h$ singular vectors share the properties of the plane-waves outlined above. It is found that the properties of the singular vectors are more similar to that of plane-waves at high wavenumbers. This increased similarity is attributed to the fact that the normal modes have shallower structure at high wavenumbers and therefore do not 'interfere' as much in the potential vorticity dynamics at high wavenumbers.

By extending the concept of an optimal height for modal unmasking of a potential vorticity wave, that was proposed by De Vries and Opsteegh (2005), the requirement for modal unmasking to lead to large amplification is inferred. This requirement is that the optimal unmasking height coincide with the region just above (below) the lower (upper) boundary steering level, where the projection of the continuum modes onto the normal mode is potentially large. Through this connection it is implied that the transition from the untilting to modal masking regime will occur at shorter integrations for small zonal scales, than for large zonal scales. Furthermore it is hypothesised that unlike untilting, modal unmasking cannot characterise the growth of large numbers of singular vectors. This is because modal masking requires the continuum modes to conceal two specific normal modes, whereas untilting requires that a multiplicity of continuum modes conceal each

other.

3.2 Definition and Computation of the Eady Model Singular Vectors

3.2.1 Definition of the singular vectors

The singular value decomposition was introduced in Chapter 1. For convenience we shall reiterate the basic points again here. We shall also make definitions of the matrices used in the singular vector computation which are specific to Eady model singular vectors computed in this thesis. We shall use the matrix $L \in \mathbb{R}^{N_g \times N_g}$ to denote an integration of a numerical version of the Eady model over a finite time interval τ. The operation of the matrix L is summarised by the matrix vector equation

$$\boldsymbol{\psi}(\tau) = L\boldsymbol{\psi}(0) \tag{3.1}$$

where $\boldsymbol{\psi} \in \mathbb{R}^{N_g}$ is vector of grid-point streamfunction values and N_g is the number of grid-points. It is worth noting here that the matrix L will be used only for the Eady model. For discussions of general linearised dynamical models the matrix M will be used.

As was discussed in the previous chapter, the quasi-geostrophic approximations from which the Eady model is derived are only applicable to scales of order $10^3 km$. However for reasons of numerical accuracy, which will be discussed in the next section, the numerical model resolves zonal wavelengths much smaller than $10^3 km$. To filter these smaller zonal wavelengths from the initial conditions we define a reduced rank discrete Fourier transform matrix $F \in \mathbb{R}^{2N_k \times N_g}$. The matrix F transforms the grid-point streamfunction vector $\boldsymbol{\psi} \in \mathbb{R}^{N_g}$ to the lower dimensional

vector of streamfunction Fourier coefficients $\hat{\boldsymbol{\psi}} \in \mathbb{R}^{2N_k}$, where N_k is the number of resolved wavelengths greater than a chosen truncation. For the experiments presented in this thesis the wave-spectrum is truncated at $0.8N_0Z/f_0$ which corresponds to $800km$ with the parameters used in the Eady model. The reverse Fourier transformation is performed by the matrix F^T. Since the rows of F are orthonormal [Golub and Van Loan (1983)], F^T is the pseudo-inverse [Golub and Van Loan (1983)] of F. For grid-point streamfunction vectors $\boldsymbol{\psi}$ which do not contain zonal wavelengths shorter than $0.8N_0Z/f_0$, the following relationships are satisfied:

$$\|\boldsymbol{\psi}\|_2 = \|F\boldsymbol{\psi}\|_2, \tag{3.2}$$

$$F^T F\boldsymbol{\psi} = \boldsymbol{\psi}; \tag{3.3}$$

however these relationships are not satisfied if $\boldsymbol{\psi}$ contains wavelengths smaller than the cutoff wavelength. For grid-point streamfunction vectors which do contain wavelengths shorter than $0.8N_0Z/f_0$ multiplication by the matrix F^TF removes these smaller wavelengths, leaving the wavelengths longer than $0.8N_0Z/f_0$ unchanged. The matrix F^TF is a discrete Fourier filter.

The Eady model singular vectors are computed from the matrix $LF^TF \in \mathbb{R}^{N_g \times N_g}$. The use of an initial time Fourier filter is consistent with the singular vector computation methods employed using more complex models in meteorological centres; e.g. Buizza (1997), LI et al. (2005). The mathematical properties of the singular vectors are summarised thus. The singular vectors consist of two complete orthonormal bases. One basis is formed from the right singular vectors $\boldsymbol{v}_i \in \mathbb{R}^{N_g}$, and the other from the left singular vectors $\boldsymbol{u}_i \in \mathbb{R}^{N_g}$. Since they form orthonormal

bases the singular vectors satisfy the relationships

$$\boldsymbol{v}_i^T \boldsymbol{v}_j = \begin{cases} 1, & i = j \\ 0, & i \neq j \end{cases}, \tag{3.4}$$

and

$$\boldsymbol{u}_i^T \boldsymbol{u}_j = \begin{cases} 1, & i = j \\ 0, & i \neq j \end{cases}. \tag{3.5}$$

The left and right singular vectors are linked by the equation

$$LF^T F \boldsymbol{v}_i = \sigma_i \boldsymbol{u}_i, \;\; i \in [1, 2, \ldots N_g]. \tag{3.6}$$

where $\sigma_i \in \mathbb{R}$ is the corresponding singular value. By convention the singular values and vectors are ordered such that

$$\sigma_1 \geq \sigma_2 \geq \ldots \sigma_{N_g} \geq 0. \tag{3.7}$$

The right singular vectors can be interpreted as a set of orthogonal initial states. Each of these initial states evolves over the finite time interval to the corresponding left singular vector multiplied by the singular value. Since the left singular vectors are orthogonal to each-other, each of the final states are also orthogonal to each-other. The singular vectors can be viewed as a set dynamical perturbations for which each perturbation is orthogonal to every other perturbation in the set at the beginning and at the end of a finite integration. It is this orthogonality property in combination with the ordering of the singular vectors that guarantees that a linear combination of singular vectors cannot amplify more than the first singular vector over the integration period [Farrell and Ioannou (1996)].

An important aspect of singular vectors is that, since they form a complete basis for the model phase space, there are the same number of singular vectors as there are degrees of freedom in the model. It is worth noting here that, due to the presence of the Fourier filter matrix $F^T F$, degrees of freedom corresponding to zonal wavelengths shorter than $0.8N_0 Z/f_0$ are associated with zero singular values. The set of the first $\mathfrak{m}$ right singular vectors contains the maximum information containable in $\mathfrak{m}$ vectors about the effect of initial random perturbations on the final state. Here the term 'random perturbations' refers to perturbations which are random with respect to the initial inner product and 'the effect on the final state' is measured in terms of the norm deriving from the final inner product. For the Eady model singular vectors computed in this thesis the 2-norm of the streamfunction field is used as both the initial and final norm. The choice of norm will be discussed more thoroughly in Section 3.2.3.

3.2.2 Computation of the singular vectors

The singular vectors are computed from the matrix $LF^T F$ corresponding to a finite integration of a numerical version of the Eady model. The details of the discrete equations can be found in Appendix A but we shall note some of the basic points here. The model is formulated on a numerical grid with $N_x = 120$ grid points zonally and $N_z = 51$ grid points vertically. The discrete streamfunction field is defined on all grid-points. The potential vorticity is defined on all grid-points except the upper-most and lower-most vertical levels. The boundary potential temperature is defined on the upper-most and lower-most level. The streamfunction is related to potential vorticity using a $5-$point approximation to the Laplacian operator and to the upper and lower boundary potential temperature using a one-sided difference approximation to the vertical derivative. The use of one-sided approximations to the vertical derivative is motivated by the

fact it allows the numerical model state to be determined by knowledge of the streamfunction at all grid-points. The zonal derivative is approximated using the 'leapfrog' scheme. The zonal advection equations are solved using a centred-time centred-space scheme.

All calculations are performed on a physical domain of dimension $X = 8 \times 10^3 km$ and $Z = 10km$ corresponding to spatial steps $\Delta_x = 66.\dot{6}km$ and $\Delta_z = 0.2km$ respectively. A time-step $\Delta_t = 11.0min$ is used. Parameter values $f_0 = 10^{-4}s^{-1}$, $N_0 = 10^{-2}s^{-1}$ and $\Lambda = 4 \times 10^{-3}s^{-1}$ are used. For numerical accuracy, the time, zonal and vertical coordinates are non-dimensionalised by factors $N_0/f_0\Lambda$, $N_0 Z/f_0$ and Z respectively.

Due to the use of the centred time centred-space advection scheme, the advection speed of the background zonal wind is under-estimated by a factor which depends upon the wavenumber. As long as the Courant number is kept below a certain threshold value, this factor is the same for a given wavenumber on every vertical level. It is important that the factorial phase error for a given wavenumber is the same on every level, as it guarantees that, although each zonal wavenumber experiences a slightly different zonal wind-field, the wind-field experienced by each wavenumber increases linearly with height. Ensuring that the zonal wind-field experienced by each zonal wavenumber is linearly increasing is important for consistency between the numerical and continuous Eady equations and facilitates the comparison of numerical and continuous solutions to the Eady model. From a physical point of view the phase errors are equivalent to an underestimation of the wind-shear parameter. The numerical wind-shear parameter can be written as the wind-shear parameter assumed in the continuous equations multiplied by a constant. Table 3.1 gives the numerical phase speed as a fraction of the continuous phase speed for the first ten zonal wavenumbers ($k_n = 2n\pi/X, \;\; n = 1, 2, \ldots 10$) supported by the domain. The values in Table 3.1 were computed via Equation A.25 given in Appendix A. For reasons of numerical accuracy, and

n	1	2	3	4	5	6	7	8	9	10
Λ_{num}/Λ	1.0	1.0	1.0	0.99	0.99	0.98	0.98	0.97	0.96	0.95

Table 3.1 *Fractional phase errors.*

because the Quasi-Geostrophic approximation applies only to horizontal scales of $\sim 10^3 km$ and above, we shall restrict the computed singular vectors to the region of phase space spanned by the first ten zonal wavenumbers. The Fourier transform matrix F is therefore defined to compute only the Fourier coefficients of first ten zonal wavenumbers. For the advection of the potential vorticity field, the numerical phase speed is characterised by the values in Table 3.1. The normal modes, however, do not travel with the advection speed of the background flow, therefore the numerical normal mode phase speed is not obtained directly from the values given in Table 3.1. The numerical phase speed of the normal modes is estimated empirically, by evolving discretised continuous normal modes using the numerical model. For the exponentially unstable long-wave normal modes, the real phase speed is found to be equal to the phase speed in the centre of the domain. For the neutral short-wave normal modes, the phase speed is found to correspond to the numerical phase speeds of potential vorticity waves located slightly below the theoretical steering level height. For reference, Figure 3.1 shows the theoretical steering level (continuous black dashed line) and the empirically determined discrete numerical steering level (blue dashed line).

The singular value decomposition is computed from matrix operator $LF^T \in \mathbb{R}^{N_g \times 2N_k}$, corresponding to an integration of the numerical model over a finite time interval. This matrix operator is obtained by systematically evolving and storing columns of the identity matrix $I \in \mathbb{R}^{2N_k \times 2N_k}$. The singular value decomposition is then performed on the stored matrix. It should be noted here that, although the right singular vectors are computed in Fourier space, the Fourier space singular

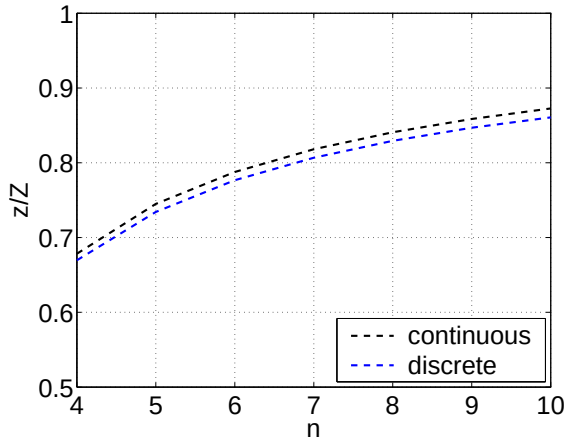

Figure 3.1 *Continuous (black line) and discrete numerical (blue line) steering levels*

vectors $\hat{\boldsymbol{v}}_i$ are trivially related to the grid-point singular vectors of LF^TF via $\boldsymbol{v}_i = F^T\hat{\boldsymbol{v}}_i$.

3.2.3 On the choice of norm

The singular value decomposition of atmospheric models has been found to be highly sensitive to the particular choice of inner product used in the computation; Palmer et al. (1998). For the singular vectors to be able to completely span the model phase space the norm must be defined using a non-singular transformation of the model state variables. In quasi-geostrophic theory the entire state of a model is uniquely determined by knowledge of the stream-function field at all points in the model domain; Pedlosky (1979). Therefore the requirement of a norm in the Eady model is that it be uniquely related to the stream-function field. Three such uniquely determinable norms have been used to compute singular vectors in the Eady model. These three norms are the stream-function norm, the quasi-geostrophic total energy norm [Ehrendorfer (2000)] and the potential enstrophy norm. The potential enstrophy norm is the $2-$norm of the boundary potential temperature perturbations and interior potential vorticity perturbation. Since the perturbation potential vorticity is conserved in the Eady model, the potential enstrophy norm measures the amplification

of the boundary potential temperature perturbations weighted by a constant contribution from the potential vorticity. The use of potential temperature throughout the domain as a norm is prohibited because the transformation from stream-function to potential temperature is singular. Ehrendorfer (2000) showed that by adding the transformation matrices for potential temperature and velocity, a non-singular transformation could be defined that allows the use of total energy as a norm in quasi-geostrophic models.

The norm dependence is of particular importance to predictability problems, because, in singular vector based targeting, it is the choice of initial time norm that reflects what is known about the initial condition errors. For predictability problems, total energy has commonly been used to define the norm. The choice of total energy stems from tests performed by Palmer et al. (1998) which indicate that for total energy singular vectors the distribution of energy in wave-space is most similar to estimates of the distribution of analysis error energy in wave-space. Interestingly Palmer et al. (1998) find that diagnostics of singular vectors computed using the kinetic energy norm yield results which are 'qualitatively similar' to those of total energy singular vectors. The similarity of kinetic and total energy singular vectors implies that the kinetic energy plays a significantly greater role in determining the structure of total energy singular vectors than potential energy.

For perturbations in the Eady model consisting of a single zonal wavelength, stream-function and velocity amplification are equivalent. Kinetic energy amplification is trivially found from velocity amplification squared. Since the singular vectors of the Eady model are found to be single zonal wavelength perturbations the structure of the singular value decomposition is identical whether the initial and final norms are stream-function or the initial and final norms are kinetic energy; Kim and Morgan (2002). The qualitative similarity between kinetic energy and total energy singular

vectors highlighted by Palmer et al. (1998) has been noted in the Eady model by Kim and Morgan (2002). Also, Kim and Morgan (2002) note that in contrast to the potential enstrophy singular vectors, the leading stream-function (a proxy for kinetic energy) and total energy singular vectors both rely heavily on the untilting of initially up-shear tilted potential vorticity anomalies. Further evidence for the similarity between kinetic and total energy amplification in the Eady model comes from Badger and Hoskins (2001), who demonstrate that, for the untilting mechanism, the variation of amplitude and growth rates measured by the kinetic and total energy norms are qualitatively very similar.

For simplicity in the work presented here we will consistently use the stream-function norm at both initial and final time for all singular value calculations. It can be fairly well assumed that in the Eady model at least the singular vectors computed using the stream-function norm are consistent with those computed using the total energy norm and therefore consistent with the type of singular vectors commonly used in singular vector targeting methods.

3.3 Implications of the dynamical mechanism of the Eady model for singular vectors

3.3.1 Comparison of continuous and discrete perturbations

Since the Lanczos algorithm allows accurate computation of the leading singular vectors without the expense of computing the full spectrum [Golub and Van Loan (1983)], the singular value decomposition has become a useful tool in analysing the stability properties of high dimensional (linearised) non-linear numerical models. The leading right singular vectors are interpreted as

the most unstable initial phase space directions for a finite time integration; Palmer et al. (1998). In this context instability is defined as instability of the flow to perturbations which are random with respect to the initial time norm used in the singular vector computation. The orthogonality properties of the singular vectors guarantee that they contain the maximum possible information about the instability of the linearised model over a finite time interval within a limited number of vectors. However, since the singular vectors are computed from numerical models they do not possess a continuous functional form and generalisations about the relationship between the background flow and the singular vectors are not easily made.

For simple models such as the Eady model the existence of analytical solutions to the continuous equations facilitates the comparison of singular vectors to continuous functions. Several publications exist in this area: Mukougawa and Ikeda (1994) interpret the properties of the first singular vector in terms of the untilting mechanism of Farrell (1984); Morgan and Chen (2002) diagnose the first singular vector structure in terms of continuum and normal modes to investigate the effect of modal masking; De Vries and Opsteegh (2005) investigate the effect of neutral mode resonance on the first singular vector of the Eady model without rigid upper boundary. All these studies concentrate on the dynamical properties of the first singular vector and do not consider its relationship to the other 'lower order' singular vectors. By lower order singular vectors we mean the second, third, fourth, etc singular vectors.

In this section we consider the implications of the growth mechanisms described in Chapter 2 to the properties of singular vectors. The aim here is not to characterise and explain the structure of particular singular vectors, but rather to make inferences about more general properties of the singular vector structure as a whole. Properties such as the optimal growth of the first singular vector, the orthogonality between the vectors and the number of orthogonal phase space directions

which can be characterised by a certain behaviour will be considered. We present this material prior to discussion of the computed singular vectors, because whilst it will prove relevant to our discussion of the singular vectors, it does not derive from analysis of the singular vectors themselves. This section is divided into two subsections. In the first subsection we consider the plane-wave solution of Farrell (1984) and in the second we consider the modal masking and to a lesser extent resonance growth mechanisms.

3.3.2 Plane-Wave untilting

Mukougawa and Ikeda (1994) draw an analogy between Farrell (1984)'s plane-wave particular solution to the Eady equations and the dynamical growth mechanism of the first singular of the Eady model. Here we shall extend this analogy and consider the implications of untilting to the plane-waves orthogonal to the optimally growing plane-wave. Firstly it must be noted that the plane-wave particular solution in itself cannot be used to specify every phase space direction, because the upper and lower boundary conditions give rise to a 'non-plane-wave' homogeneous solution. However, for the moment we shall ignore the effect of the homogeneous solution and discuss the plane-waves in isolation. Ignoring the homogeneous solution may be considered equivalent to applying the upper boundary condition from De Vries and Opsteegh (2005) (for example) to both boundaries; i.e. the streamfunction vanishes at $z = \pm\infty$ and we are only interested in the behaviour of the solution within a finite region $[z_1, z_2]$ which lies far from the upper and lower boundaries.

The continuous equivalent of the streamfunction norm is defined by the square-root of the integral

of the streamfunction-squared amplitude over the domain; i.e.

$$\|\psi\|_c = \left(\int_{z_1}^{z_2} \int_0^X \psi^2 dx dz \right)^{\frac{1}{2}}, \tag{3.8}$$

where the subscript c denotes the continuous norm. The continuous streamfunction norm amplification over a finite time interval, τ, is then defined as the ratio $\|\psi(\tau)\|_c / \|\psi(0)\|_c$. By substituting the plane-wave Equation (2.36) into this ratio, we define the continuous streamfunction norm amplification over a finite time interval τ of a plane with initial tilt a_0 as

$$\|\psi(\tau)\|_c / \|\psi(0)\|_c = \frac{1 + a_0^2 f_0^2 / N_0^2}{1 + (a_0 - \Lambda\tau)^2 f_0^2 / N_0^2}. \tag{3.9}$$

From this expression it is noted that the amplitude depends only on the initial tilt and the integration length. Since it depends on initial tilt and not zonal wavenumber the amplification achieved over a finite time interval by plane-waves with the same initial tilt but different zonal wavenumbers is the same. For a fixed finite integration length, τ, the plane-wave initial condition that gives rise to maximum amplification will be the one whose initial tilt maximises Equation (3.9). We shall call the tilt which maximises the amplification over a finite time period the optimal tilt a_0^{opt}. By equating the differential of Equation (3.9) with respect to a_0 to zero and rearranging we obtain

$$a_0^{\pm} = \frac{\Lambda\tau \pm \sqrt{\Lambda^2\tau^2 + 4\frac{N_0^2}{f_0^2}}}{2}. \tag{3.10}$$

The optimal tilt is obtained when the square-root term is positive; i.e. $a_0^{opt} = a_0^{+}$. When the square-root term is negative the tilt a_0^{-} is that which maximises decay over the finite time interval. The optimal initial tilt is plotted in Figure 3.2 (black dashed line) as a function of integration length τ. For reference the dotted line shows the initial tilt $a_0^{Orr} = \Lambda\tau$ for which the potential vorticity is rendered vertical at the end of the integration period and the untilting plane-wave has

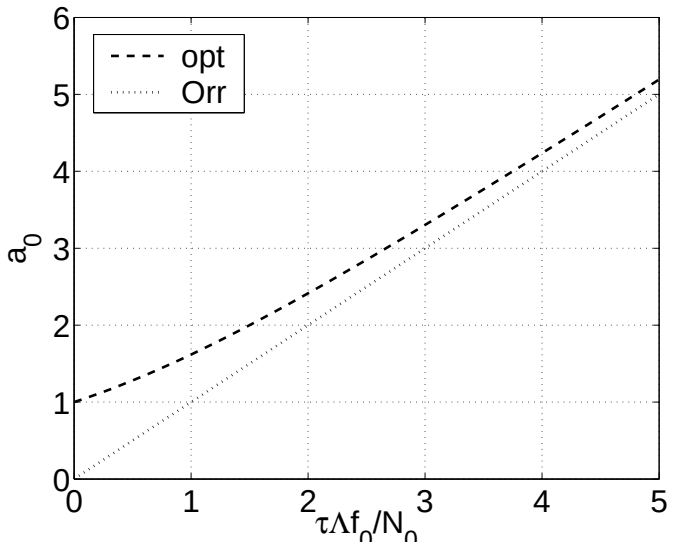

Figure 3.2 The variation of optimal initial tilt (dashed) and Orr tilt (dotted).

reached its maximum amplitude. Following the naming convention of Mukougawa and Ikeda (1994) we call $a_0^{Orr} = \Lambda\tau$ the Orr initial tilt. From Figure 3.2 it is evident that the initial tilt that maximises growth over a finite time interval is always greater than the Orr tilt, but that as the integration length increases these two values converge. The fact the optimal tilt is larger than the Orr tilt is a correction to the plane-wave singular vector analogy of Mukougawa and Ikeda (1994) who model singular vector growth using the Orr tilt rather than the optimal tilt. By substituting a_0^{opt} into Equation (3.9) an upper bound on the amplification achievable by the untilting mechanism is obtained.

Having identified the maximally amplifying plane-wave we now consider the condition for orthogonality between two plane-waves. For two plane waves with the same zonal wavenumber k_n but differing tilts $a(t)$ and $a(t) + \delta a$ the criteria for orthogonality can be shown to be

$$\delta a = \pm \frac{2\phi\pi}{k_n(z_2 - z_1)}, \tag{3.11}$$

where $\phi \neq 0$ is an integer. Proof of this relationship is given in Appendix B. Perturbations of differing zonal wavenumbers are orthogonal to each-other due to the periodicity of the domain in the zonal direction. Since the evolution of the tilt between two time-points t_1 and t_2 is given by $a(t_2) = a(t_1) - \Lambda(t_2 - t_1)$, it can easily be verified that two plane-waves that satisfy the condition for orthogonality given in Equation (3.11) at a given time point t_1, will still satisfy the orthogonality condition at a subsequent time point t_2. To see this one simply need consider two tilts at t_1, a and $a'(t_1) = a(t_1) \pm \delta a$ respectively. Over the time interval t_1 to t_2 both tilts change by $-\Lambda(t_2 - t_1)$, therefore at t_2 we may write $a(t_2) = a(t_1) - \Lambda(t_2 - t_1)$ and $a'(t_1) = a(t_1) \pm \delta a - \Lambda(t_2 - t_1) = a(t_2) \pm \delta a$; i.e. the difference between the two tilts remains fixed at $\pm\delta a$.

Several points may be inferred from the orthogonality and optimal growth/decay conditions defined by Equations (3.10) and (3.11) respectively. Firstly, it is noted that, as is the case for singular vectors, a set of orthogonal plane-waves will be orthogonal at both the beginning and end of a finite time interval. Secondly we are free to choose one plane-wave in the set to be that which maximises growth over the finite time interval, and using Equation (3.11) we may chose all subsequent plane-waves to be orthogonal to it. In this way, we can define a discrete set of continuous functions which share some of the properties of the singular vectors of a discrete set of equations. From Equation (3.10) we can deduce that the difference in tilt between the optimally growing and decaying plane-wave is given by $a_0^+ - a_0^- = \sqrt{\Lambda^2\tau^2 + 4\frac{N_0^2}{f_0^2}}$. If the difference in the tilt of optimally amplifying and decaying plane-waves satisfies the orthogonality criteria given in Equation (3.11), then both the optimally amplifying and decaying plane-waves will be contained in the discrete set of orthogonal plane-waves. This condition can only be satisfied for a discrete set of values of τ, since the orthogonality criteria yields a discrete set of tilts. It is worth noting that

for this discrete set of finite time intervals the orthogonal plane-waves (if normalised) appear to share several of the mathematical properties of the singular vectors of a discrete matrix; however it must be stressed that we are not attempting to suggest that this set of orthogonal plane-waves is analogous to singular vectors; we are rather motivating the contrived question: 'if the singular vectors structure and evolution were described entirely by the plane-wave untilting Equation (2.36), what would we expect the properties of the singular vector spectrum to be?'. As we shall see in Section 3.4, and as is evident in the work of other authors (Morgan (2001) for example), the singular vectors are not of purely plane-wave. In answering this question we shall however shed some light on the properties of singular vectors.

We have identified the optimal tilts for amplification and decay, but we have not yet considered the amplification of the plane-waves orthogonal to the maximally amplifying/decaying plane-wave. To shed some light on this topic Figure 3.3 (after Badger and Hoskins (2001)) shows the variation of the stream-function amplification rate (y-axis) with tilt (x-axis). From Figure 3.3 it can be seen that the maximum amplification and decay rates occur near $a = 0$ and that as $|a|$ tends to infinity the amplification rate tends to zero. Since the amplification *rate* tends to zero as the tilt tends to infinity the amplification over a finite time interval tends to unity as the *initial* tilt tends to infinity; Therefore for a finite time interval all the growing and decaying plane-waves will have tilts 'near' to $a_0 = 0$. Mukougawa and Ikeda (1994) make the point that for discrete models when the integration length increases beyond a certain level the Orr initial tilt will require a vertical wavelength smaller than the discrete model's resolution. We may also make the point that for a fixed integration if the vertical resolution is increased (relative to a fixed zonal resolution) beyond a certain value then the newly resolved perturbations will not be able to grow via the untilting mechanism. From a singular vector perspective this implies that if untilting accounts for the

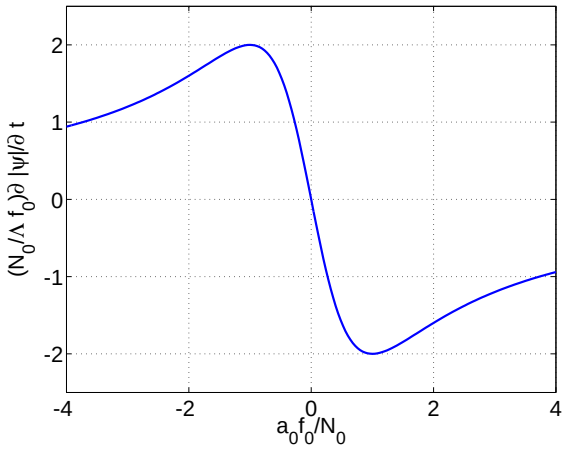

Figure 3.3 *Untilting streamfunction/kinetic energy amplification rate; after Badger and Hoskins (2001)*

growth of singular vectors, then increasing vertical resolution will eventually lead only to the addition of a large number of arbitrary (except in their orthogonality to the growing/decaying singular vectors), 'essentially' neutral singular vectors.

An important implication of Equation (3.11) for the amplification of plane-waves orthogonal to the optimally amplifying plane-wave is that, since δa depends on $1/k_n$, the difference in tilt between two orthogonal plane-waves is smaller for high zonal wavenumbers. Since the difference between the tilts of orthogonal plane-waves is smaller for high zonal wavenumbers than for low zonal wavenumbers, the difference in growth rates between orthogonal plane-waves is also smaller for high zonal wavenumbers than for low zonal wavenumbers. The increasing similarity in the finite time amplification of orthogonal plane-waves with increasing wavenumber implies that the amplification of the nearest (in terms of initial tilt) orthogonal plane-waves to the optimally growing plane-wave will tend to the amplification of the optimally growing plane-wave, as the zonal wavenumber tends to infinity. From a singular vector perspective one might expect that, if plane-wave untilting explains much of singular vector growth, then the singular values associ-

ated with singular vectors (other than the optimal vector) of small zonal scale will be larger. For orthogonal plane-waves, it has been seen that, whilst the amplification of the optimal plane-wave is the same for all zonal scales, the amplification of the plane-waves orthogonal to the optimal is larger for smaller zonal scales. In fact as the zonal scale tends to infinity, the finite time amplification of plane-waves orthogonal to the optimally amplification plane-wave tends to that of the optimally growing plane-wave, and hence a set of orthogonal plane-waves ordered by amplification will be dominated by the smallest scales. However, the quasi-geostrophic equations which define the Eady model only apply to small Rossby number flows. The need of small Rossby number limits the applicability of the Eady equations, for typical mid-latitude stability and Coriolis parameters, to zonal scales greater than $\sim 10^3 km$.

In our discussion so far, we have ignored the effect of the homogeneous component of the plane-wave solution of Farrell (1984). Ignoring the homogeneous solution is essentially equivalent to changing the boundary conditions. We shall now consider the relationship between the untilting plane-waves and the homogeneous solution; i.e. we shall re-introduce the rigid upper and lower boundaries. Firstly, it is noted that plane-waves are not orthogonal (with respect to streamfunction) to their corresponding homogeneous solution; Farrell (1984). This lack of orthogonality means that, even if the homogeneous component of the solution is zero at the start of a finite time interval, it will not be by the end of the time interval. Since the homogeneous solution does not remain zero, the orthogonality condition for plane-waves given in Equation (3.11) cannot be applied to a set of perturbations in the region $z_1 = 0$ and $z_2 = Z$ at both the start and end of a finite time interval. However, it is still possible that, for a region $0 < z_1 < z_2 < Z$, the plane-waves are orthogonal to the homogeneous solution, and the orthogonality Equation (3.11) may be applied to a set of perturbations at initial and final time.

By considering the vertical structure of the normal modes, we can gain some insight into the relationship between plane-waves and the corresponding homogeneous solution. First, we shall remind the reader that the homogeneous component of the plane-wave solution of Farrell (1984) has the same vertical structure as the normal modes, but differing temporal behaviour. It is reasonable to assume that the effect of the homogeneous solution on the untilting mechanism will be weak at heights where the normal modes have small amplitude. As was seen in Figures 2.3A and 2.3B, the amplitude of normal modes associated with wavelengths below the short-wave cutoff resides primarily above (below) the upper (lower) boundary steering level, with some amplitude extending into a region just below (above) the upper (lower) boundary steering level. Since the amplitude of the normal modes is small between the upper and lower boundary steering levels, we can infer that the effect of the homogeneous solution will be relatively weak in this region. Since the steering levels are further apart for the smallest zonal scales, we can further infer that the size of the region in which the homogeneous solution has only weak effect is larger for smaller scales. We may therefore expect the behaviour of small zonal scales to be closer to that of the plane-wave particular solution given in Equation (2.36), than the large scales. For the longer wavelengths, the normal modes have significant amplitude throughout the domain, so it would be expected that the homogeneous component of the solution has large effect throughout the domain.

3.3.3 Modal unmasking

We have so far considered the implications of the plane-wave untilting to singular vectors. In this section we shall consider the implications of modal unmasking. A significant difference between potential vorticity unshielding and modal masking/neutral mode resonance is that whilst the former depends on the relative positions of an infinite number of potential vorticity waves

to one-another the later depends on the relative position of the potential vorticity waves to two specific normal modes. The limitation to dependency on the two particular modes means that perturbations which amplify via the neutral mode resonance and modal masking growth mechanisms can only account for a small fraction of the model phase space. The same can be said of the exponentially growing normal modes which account for only one phase-space direction for every zonal wavenumber.

Morgan and Chen (2002) consider the effects of modal masking on the first singular vector for a representative wavelength above the short-wave cutoff and a representative wavelength below the short-wave cutoff. For the leading singular vectors presented by Morgan and Chen (2002), the effect of modal masking is found to be very significant. In the case of the singular vector below the short-wave cutoff, Morgan and Chen (2002) point out that the amplitude of the normal mode is masked by a relatively small number of the continuum modes. For this short-wave singular vector, the potential vorticity associated with these continuum modes is a found to be plane-wave perturbation located in a small region either side of the steering level. In the unmasking mechanism described by Morgan and Chen (2002) the normal mode is revealed because of the net cancellation of the continuum mode boundary potential temperature anomalies associated with the potential vorticity anomalies above and below the steering level. Interestingly, despite the fact that the largest amplitude potential vorticity waves reside on nearest discrete vertical levels to the steering level, no linear amplification due to resonance is apparent, when the singular vector is evolved far beyond the integration length used in the singular vector computation.

De Vries and Opsteegh (2005) note that, for a single potential vorticity wave, the modal masking effect is maximised if the potential vorticity wave resides at a distance

$$\delta z = \frac{\pi}{k_n \Lambda \tau} \tag{3.12}$$

below (above) the upper (lower) boundary steering level. The motivation for the definition of this expression lies in the fact that, if the potential vorticity resides at this height, the difference in phase speeds between the normal mode and the continuum mode will lead to a change in the relative phase of the continuum and normal mode of magnitude π. We shall call this the optimal (modal) masking height. De Vries and Opsteegh (2005), however, do not consider the implications for different zonal scales of this expression. From Equation (3.12) it is evident that the distance of the optimal masking height from the steering level is inversely proportional to the integration length *and* to the wavenumber. The results of this inverse proportionality are three-fold; firstly the distance from the steering level is smaller for higher wavenumbers; secondly the optimal masking height tends to the steering level height as the integration length increases; thirdly the optimal masking height approaches the steering level with increasing τ at a faster rate at small zonal scales than large zonal scales. De Vries and Opsteegh (2005) find that the optimal location of the single potential vorticity wave resides nearer to the steering level than this optimal height for all integration lengths and conclude that resonance plays a greater role than modal masking in the perturbation amplification. However, the findings of De Vries and Opsteegh (2005) must be qualified by the fact that the perturbation is limited to initially have zero potential temperature at the boundary.

Another point that is not discussed by De Vries and Opsteegh (2005) is that the amplification achievable via modal masking by a potential vorticity wave residing at the optimal masking height

will only lead to large amplification if the optimal masking height coincides with a height at which the continuum mode can have large projection onto the normal mode. We can gain some insight into the locations at which this may occur by considering the analysis of Morgan and Chen (2002). Morgan and Chen (2002) find that for small zonal scales 'only a limited number of (continuum) modes (located near the steering level) are needed to mask the large amplitude of the neutral edge modes'; whereas for large scales a 'broad distribution of continuum modes and the decaying normal mode are required to mask the initially large amplitude of the growing normal mode. This statement does not however preclude the possibility that a 'broad spectrum of continuum modes' may also be used to mask an initially large amplitude normal mode.

Further insight can be gained by considering the structure of the continuum modes. Figures 3.4A to 3.4C show, for three representative wavelengths, the vertical profile (y-axis) of the streamfunction-squared amplitude [Equation (2.32)] as a function of the height of the associated potential vorticity wave (x-axis). These figures were obtained from vertically discretising the continuous continuum modes defined in Pedlosky (1964). For low wavenumbers (Figure 3.4A) the continuum modes always have large amplitude on the upper and/or lower boundaries so modal masking can potentially occur if the optimal masking height is located anywhere in the domain. For small scales (Figure 3.4C) the amplitude is large on the boundaries only if the potential vorticity wave is located close to or above (below) the upper (lower) boundary steering level. For intermediate scales (Figure 3.4B) the behaviour lies somewhere between that of large and small scales. From this we may infer that modal masking can be an effective streamfunction amplification mechanism for small zonal scales only when the optimal masking height lies in this region near the steering level. As we shall see later, in our analysis of the singular vectors, the requirement that the optimal masking height coincides with this near steering level region defines

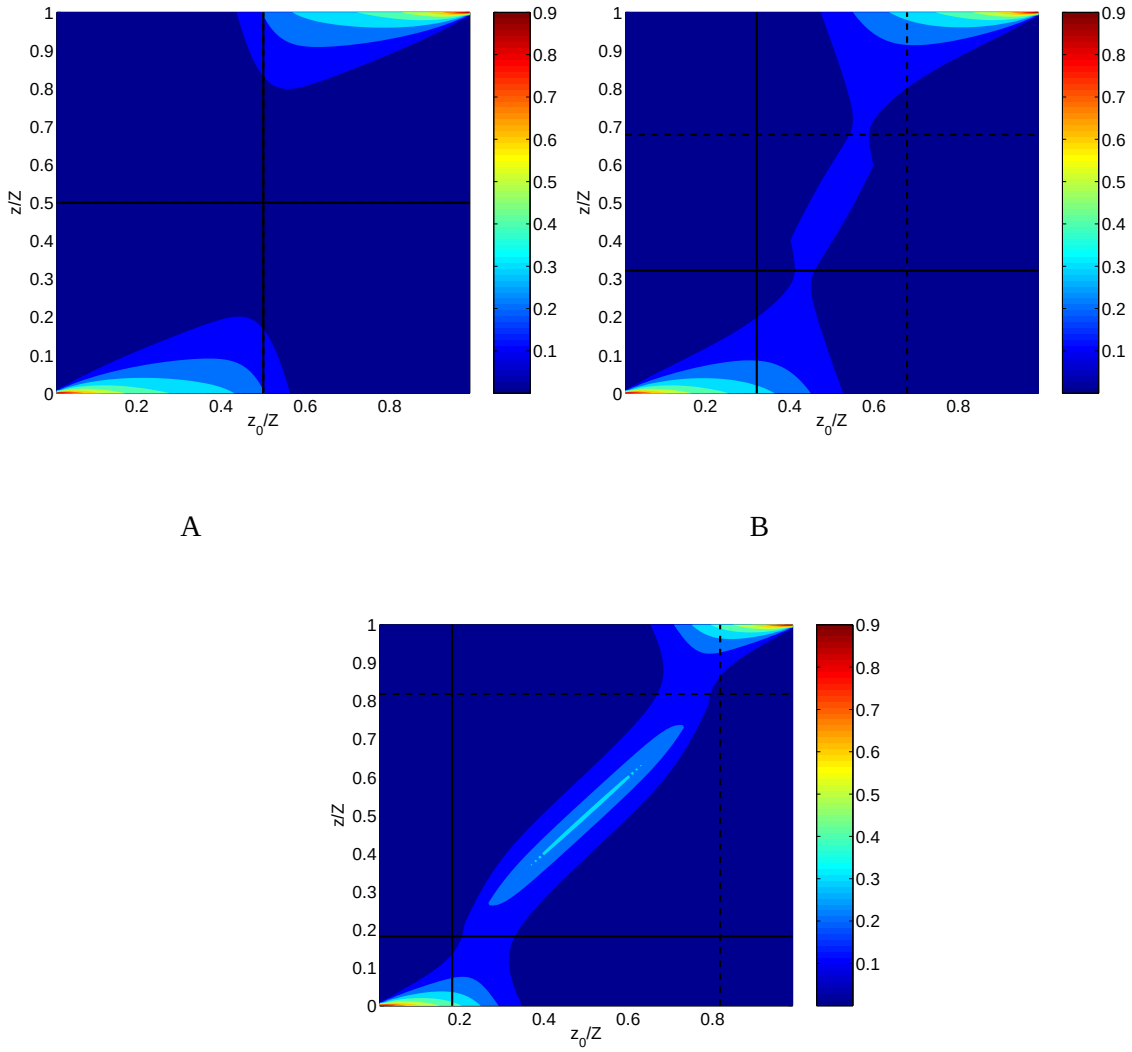

Figure 3.4 *Vertical profile (y-axis) of the streamfunction-squared amplitude [Equation (2.32)] of continuum modes, as a function of the height of the associated potential vorticity wave (x-axis). A: For wavenumber $n = 2$. B: For wavenumber $n = 4$. C: For wavenumber $n = 7$.*

the finite time integrations over which the modal masking mechanism is significant. Furthermore we shall see that due to the inverse proportionality of the optimal masking height to the zonal wavenumber, the modal masking mechanism becomes significant at shorter integration lengths for small zonal scales whereas the integration length must be longer for the same effects to be seen at large zonal scales.

3.3.4 Summary

In this section we have considered the implications of the plane-wave untilting solution of Farrell (1984), and the modal unmasking growth mechanism to singular vectors.

The main points of the discussion of the plane-wave solution of Farrell (1984) can be summarised thus. As in Mukougawa and Ikeda (1994) we consider the plane-waves in the absence of the homogeneous boundary wave component of the solution; i.e considering only Equation (2.36). Many things can be inferred from the functional form of the plane-wave solution. Firstly, considering the optimally amplifying plane-wave, it is noted that the maximum amplification depends only on the initial tilt of the plane-wave and is independent of the zonal wavenumber. This interpretation is contrary to that of Mukougawa and Ikeda (1994) who attribute the variation of the amplification of singular vectors in the $3-$dimensional Eady model to a zonal wavenumber dependence inherent in the plane-wave untilting mechanism. We shall see later, in our investigation of the singular vectors themselves, that variations in the amplification of plane-wave-like perturbations with zonal wavenumber are more likely caused by differences in the interaction between the homogeneous boundary waves and plane-waves at different zonal scales. A second point that is brought out by examination of the plane-wave particular solution given in Equation (2.36) is that the initial tilt of the optimally amplifying plane-wave is always greater than the 'Orr

initial tilt'. The fact that the optimal initial tilt is greater than the Orr tilt means that the optimally amplifying plane-wave will continue to grow via untilting for a longer period of time than the integration length. The difference between the optimal initial tilt and Orr tilt is found to be greater for short integrations than for long integrations.

The plane-wave particular solution of Farrell (1984) can be used to define a set of orthogonal perturbations which remain orthogonal when evolved in time. For high zonal wavenumbers the difference in tilt between orthogonal plane-waves is smaller than is the case for low zonal wavenumbers. The similarity of the tilt of orthogonal high wavenumber plane-waves means that the difference in finite time amplification between orthogonal plane waves is smaller for high wavenumbers than small wavenumbers. However the plane-waves (unlike singular vectors) do not form a complete set as the contribution to the phase space from the homogeneous component of the solution of Farrell (1984) must be taken into account. For high wavenumbers the structure of the continuum modes associated with potential vorticity waves in the region of the domain between the upper and lower boundary steering levels is similar to that which would be expected on an infinite domain and it is inferred that plane-wave untilting can be used to entirely characterise the stability properties of this region.

Whilst plane waves can account for a large number of phase space directions, perturbations that lead to growth by modal unmasking are constrained to point only in phase space directions for which the streamfunction field associated with the continuum modes can mask the streamfunction field associated with the normal modes. It might be expected, therefore that modal unmasking will be present in only as small number of the singular vectors.

It is hypothesised, that for the modal unmasking mechanism to lead to significant amplification,

the optimal masking height [De Vries and Opsteegh (2005)] must reside in the region near to the steering level. It is further hypothesised that, since this optimal masking height is inversely proportional to the zonal wavenumber, modal unmasking will lead to significant growth in small zonal scales at shorter integration lengths than is the case for large zonal scales.

3.4 The singular vectors of the Eady model

3.4.1 A note on the indexing convention of the singular vectors

In the previous section, we examined the potential implications of different amplification mechanisms to the singular vectors of the Eady model. In this section we shall apply the information outlined in the previous section to the singular vectors of the Eady model. We shall focus our attention on the singular vectors computed for a $12h$ and a $48h$ integration.

Before this, to avoid confusion, we shall outline the singular vector indexing conventions that we shall adopt throughout this section. In our discussions of the singular vectors, we shall adopt the following conventions: we shall index the singular vectors of different zonal wavelengths separately; each zonal wavelength/wavenumber shall be labelled by the wavenumber index n, where the wavenumber is given by $k_n = 2n\pi/X$; we shall label the singular vectors with i, with $i = 1$ referring to the singular vector associated with largest singular value, $i = 2$ the second largest; as an example, the first $n = 7$ singular vector is the singular vector with wavenumber index $n = 7$ that is associated with the largest singular value.

3.4.2 $12h$ integration

Figures 3.5A to 3.5F show the right and left singular vectors for the first three wavenumber-index seven singular vectors; i.e. the three largest amplifying singular vectors with zonal wavelength $X/7$. These singular vectors form a regular structural pattern. The first singular vector is a tilted plane wave structure with amplitude concentrated in the centre of the domain. The second comprises two tilted structures one on top of each-other and approximately $\pi/2$ out of phase. The third has three tilted structures one on top of the other; the top and bottom structures are anti-phased and the central structure is $\sim \pi/4$ out of phase. All the leading right singular vectors have amplitude minima at the upper and lower boundaries. The fourth, fifth etc singular vectors (not shown) continue this pattern; the fourth having four plane wave structures, the fifth five plane-wave structures etc. The corresponding left singular vectors follow this pattern but the tilt is reduced and the amplitude on the upper and lower boundaries has increased relative to the rest of the domain. This pattern qualitatively describes the structure of the leading singular vectors at all wavelengths. There are, however, quantitative differences between the tilts and the vertical structures. In what follows we shall outline these difference and how they are reflected in the growth rates of the singular vectors.

Firstly, we consider the tilt of the potential vorticity field associated with the singular vectors. Figure 3.6A (blue line) shows the tilt of the leading singular vector for each zonal wavenumber. For reference the black dotted line shows the Orr initial tilt and the black dashed line shows the optimal initial tilt. The slight reduction in the optimal and Orr at high wavenumbers occurs because the numerical phase speed (see Section 3.2.2) was used to calculate these tilts. At low wavenumbers, the initial tilt of the singular vectors is much larger than the optimal tilt, but asymptotes to the optimal tilt as the wavenumber increases. To understand the effect of the initial tilt on the

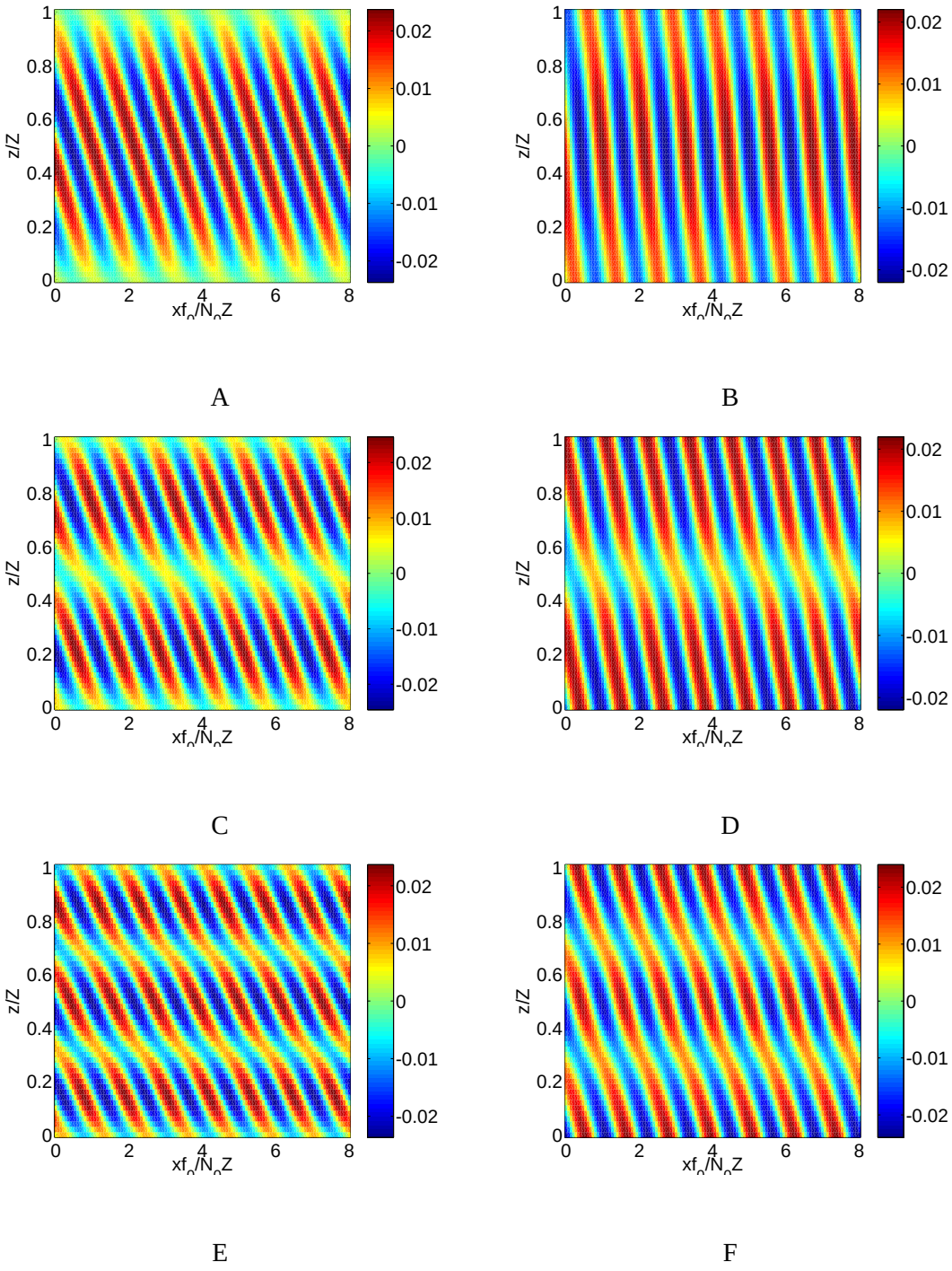

Figure 3.5 *The leading three right and left* $12h$ *singular vectors, for wavenumber index* $n = 7$*. A and B first right and left singular vector respectively. C and D second right and left singular vector respectively. E and F third right and left singular vector respectively.*

amplification, Figure 3.6B shows the amplification of the singular vectors (singular values, black line) and the theoretical amplification of a plane-wave (neglecting the effect of the homogeneous solution, blue line) with the same initial tilt as the singular vector. For reference the black dashed and dotted lines show the theoretical plane-wave amplification for the optimal and Orr initial tilts respectively. Several things are noticeable from in Figure 3.6B. Firstly, the amplification of all the singular vectors (solid black line) is less than the maximum amplification implied by the optimal initial tilt (dashed black line). Since the singular vector amplification is less than that of the optimal plane-wave it may be inferred that untilting is a less effective growth mechanism in the presence of rigid upper and lower boundaries than in an infinite domain. Furthermore, since the discrepancy is greater for small wavenumbers than high wavenumbers, it is possible that the reduction in plane-wave amplification due to the homogeneous solution gets smaller as the space between the steering level increases and the interaction between the interior potential vorticity and the homogeneous components of the solution decreases. This hypothesis is partially born out by the fact that the initial tilt of the singular vectors tends to that of the optimal plane-wave as the wavenumber increases, suggesting that untilting is major factor in the amplification.

Further evidence can be gained by considering the distribution of streamfunction amplitude in the vertical at initial (right singular vector) and final (left singular vector) time. Figures 3.7A and 3.7B show the vertical distribution of streamfunction mean-squared amplitude (y-axis) for the leading singular vectors of wave-indices one to ten (x-axis). Noticeably, at initial time, the amplitude is largest in the central region of the domain for all wavenumbers. At final time, however, the long wave singular vectors have amplitude distributed fairly evenly throughout the domain, whereas for the shortest wavelengths the final time amplitude is still concentrated in the centre of the domain. Figure 3.7C shows the potential vorticity squared amplitude for the leading singular

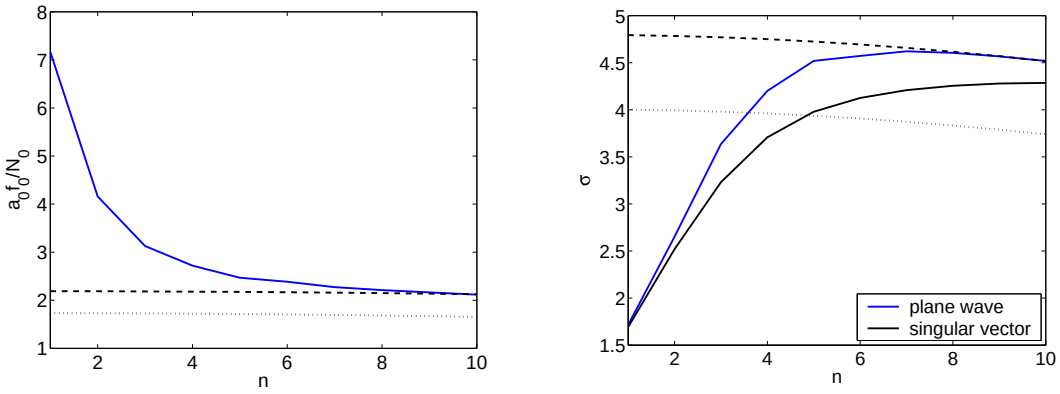

A B

Figure 3.6 *A: blue line shows the initial tilt (y-axis) of the potential vorticity field associated with the first singular vectors against zonal wavenumber index (x-axis). B: black solid line shows the leading singular values (y-axis) as a function of zonal wave-index (x-axis); the blue solid line shows the values obtained by substituting the singular vector initial tilt into the plane-wave amplification Equation (3.9). In both A and B, the dashed and dotted lines indicate values associated with the optimal and Orr initial tilts, respectively.*

vector as a function of height and zonal wavenumber. For reference the blue dashed and solid lines show the optimal masking height for the upper and lower boundaries respectively. The optimal masking height is calculated using Equation (3.12). As with the initial streamfunction field, the potential vorticity field has maximum amplitude in the centre of the domain. For all wavenumbers the optimal masking height does not lie in regions where it is expected that the masking of the normal modes by continuum modes will be large; in fact for the lowest wavenumbers the optimal masking height lies outside of the domain. Since the optimal masking height does not lie in regions associated with potentially large masking of the normal modes by the continuum modes, it may be inferred that modal masking is not the dominant amplification mechanism; that is not to say that modal masking does not occur, but merely that its effect has not reached its full potential. The fact that for small wavelengths the initial and final amplitude are both concentrated in the centre in the domain indicates that the amplification is dominated by untilting of plane-waves with high zonal wavenumbers; i.e. the amplification occurs in the locality of the of the potential vorticity waves rather than on the boundaries.

We have already seen that for 'pure' untilting plane-waves, the condition for orthogonality implies that the plane-waves orthogonal to the optimally amplifying plane-wave will achieve larger amplification for small zonal wavelengths than for large. To see if this property is also reflected in the singular vectors we shall now consider the tilt of the singular vectors other than the first singular vector. Figure 3.8A shows the initial tilts (y axis) of the first ten (right) singular vectors (x axis) for different zonal wavenumbers. For ease of viewing only wave-indices $n = 1, 3, 5, 7, 9$ (purple, light blue, red, green, dark blue respectively) are shown. As would be expected from the orthogonality condition for plane-waves the tilt of the singular vectors varies more rapidly with singular vector index for low wavenumbers than for high wavenumbers. Figure 3.8B (blue

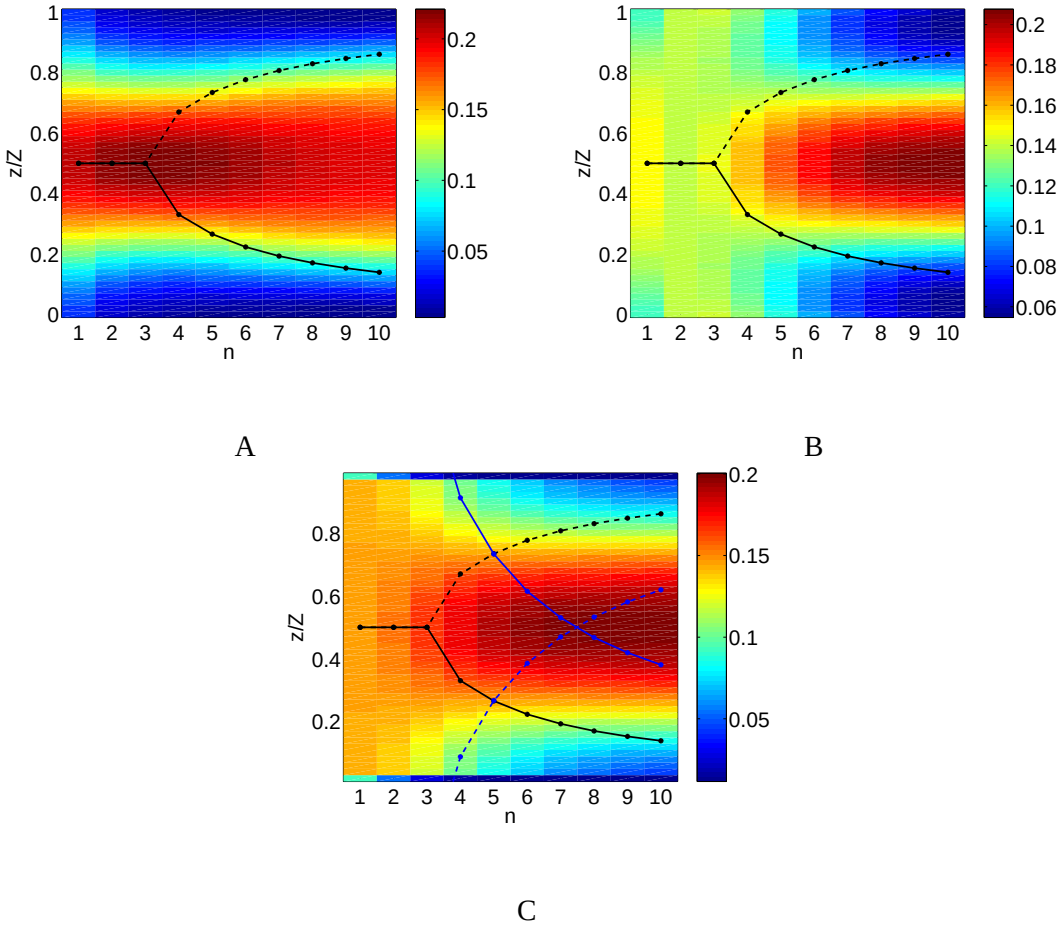

Figure 3.7 *A: Streamfunction squared amplitude as a function of height (y-axis), for the first right singular vectors of differing wavenumbers (x-axis shows wavenumber index); The black solid and dashed lines show the lower and upper boundary steering levels respectively. B: Same as A, but for left singular vectors. C: Same as A, but for potential vorticity, blue solid and dashed lines show the optimal masking height for the lower and upper boundary steering levels respectively.*

line) shows the mean rate of increase in the initial tilt with singular vector index as a function of wavenumber. For reference the black line in Figure 3.8B shows the difference in tilt between orthogonal plane-waves implied by Equation (3.11). It is noticeable in Figure 3.8B that these two lines are closer together for high wavenumbers than for low indicating again that the behaviour of singular vectors appears to be much closer to that of plane-waves at high wavenumbers than low wavenumbers. Since the initial tilt of the singular vectors varies less rapidly with singular vector index for high zonal wavenumbers, it would be expected that, due to the link between initial tilt and amplification, the singular values also vary less rapidly. To see if this is the case, we considered the normalised 'additive' amplification of the singular vectors. The normalised additive amplification is defined

$$\frac{\|L\boldsymbol{v}_i\| - \|\boldsymbol{v}_i\|}{\|L\boldsymbol{v}_1\| - \|\boldsymbol{v}_1\|} = \frac{\sigma_i - 1}{\sigma_1 - 1} \tag{3.13}$$

, and can be used to indicate the rapidity of descent of the singular value spectrum from the largest singular value $(\sigma_i - 1)/(\sigma_1 - 1) = 1$ to neutrality $(\sigma_i - 1)/(\sigma_1 - 1) = 0$. Figure 3.9A shows 'additive' amplification of the $12h$ singular vectors, as a function of singular vector index, for each zonal wavenumber (for reference Figure 3.10 shows the actual singular values). From Figure 3.9A it is clear that the magnitude singular values decay less rapidly at higher wavenumbers than at lower wavenumbers. As an example the blue line of Figure 3.9B shows the singular values for $n = 7$ and the black line shows amplification inferred by substituting the initial tilts of the singular vectors into the plane-wave amplification Equation (3.9). There is a striking similarity in the shape of the black and blue lines in Figure 3.9B indicating that the reduction in singular values with increasing 'i' is due to the increasing initial tilt.

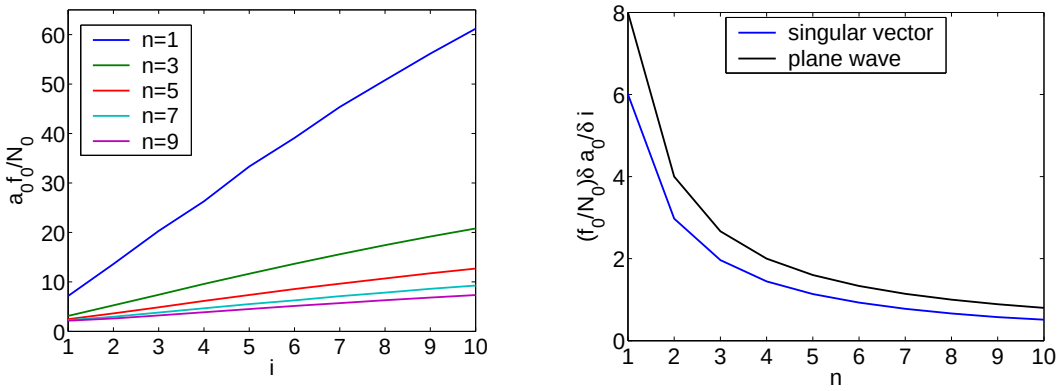

A B

Figure 3.8 *A: Variation of initial tilt (y-axis) of the $12h$ singular vectors, with singular vector index (x-axis); each line corresponds to a different zonal wavenumber. B: The blue line show the variation of the rate of change with respect to singular vector index (y-axis), with varying wavenumber (a-axis); i.e. the blue line shows the gradients of the lines in A; the black line shows the value inferred from the condition for orthogonality for plane-waves Equation (3.11).*

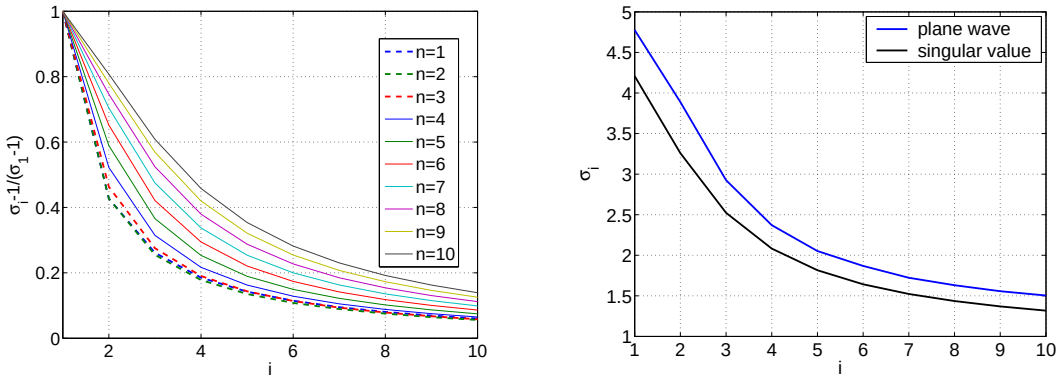

A B

Figure 3.9 *A: The normalised additive amplification of the singular vectors, as a function of singular value index, for a $12h$ integration. Each line represents a different zonal wavenumber. B: Black line shows the singular values for the first ten $n = 7$ singular vectors; blue line shows the amplification inferred by substituting the initial tilts of the singular vectors into the plane-wave amplification Equation (3.9).*

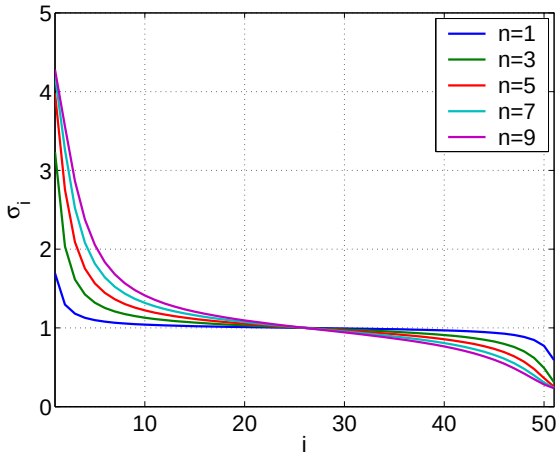

Figure 3.10 *The singular values for the $12h$ singular vectors; each line corresponds to a different wavenumber. For ease of viewing only the $n = 1, 3, 5, 7$ and 9 wavenumbers are shown.*

3.4.3 48h Singular Vectors

Figures 3.11A to 3.11F show the first three initial (right) and final (left) $n = 7$ singular vectors for the $48h$ integration. The structural pattern is somewhat similar to that of the $12h$ singular vectors. The first singular vector having one plane-wave structure, the second two plane-wave structures etc. Despite their similarities there are difference in the vertical structures of the two sets of singular vectors. From an untilting perspective the main difference lies in the increased tilt of the singular vectors. For the $48h$ singular vectors, modal masking has a much more significant effect on the structure of the singular vectors.

Unlike the $12h$ singular vectors, for the $48h$ singular vectors modal masking has become an important growth mechanism, causing significant differences between the vertical structure of the $12h$ and $48h$ singular vectors. Although the singular vectors still have tilted structure, tilting alone cannot be used to explain the amplification. To see this Figures 3.12A and 3.12B show the initial tilt and amplification of the leading singular vectors of each zonal wavenumber. As in Figures

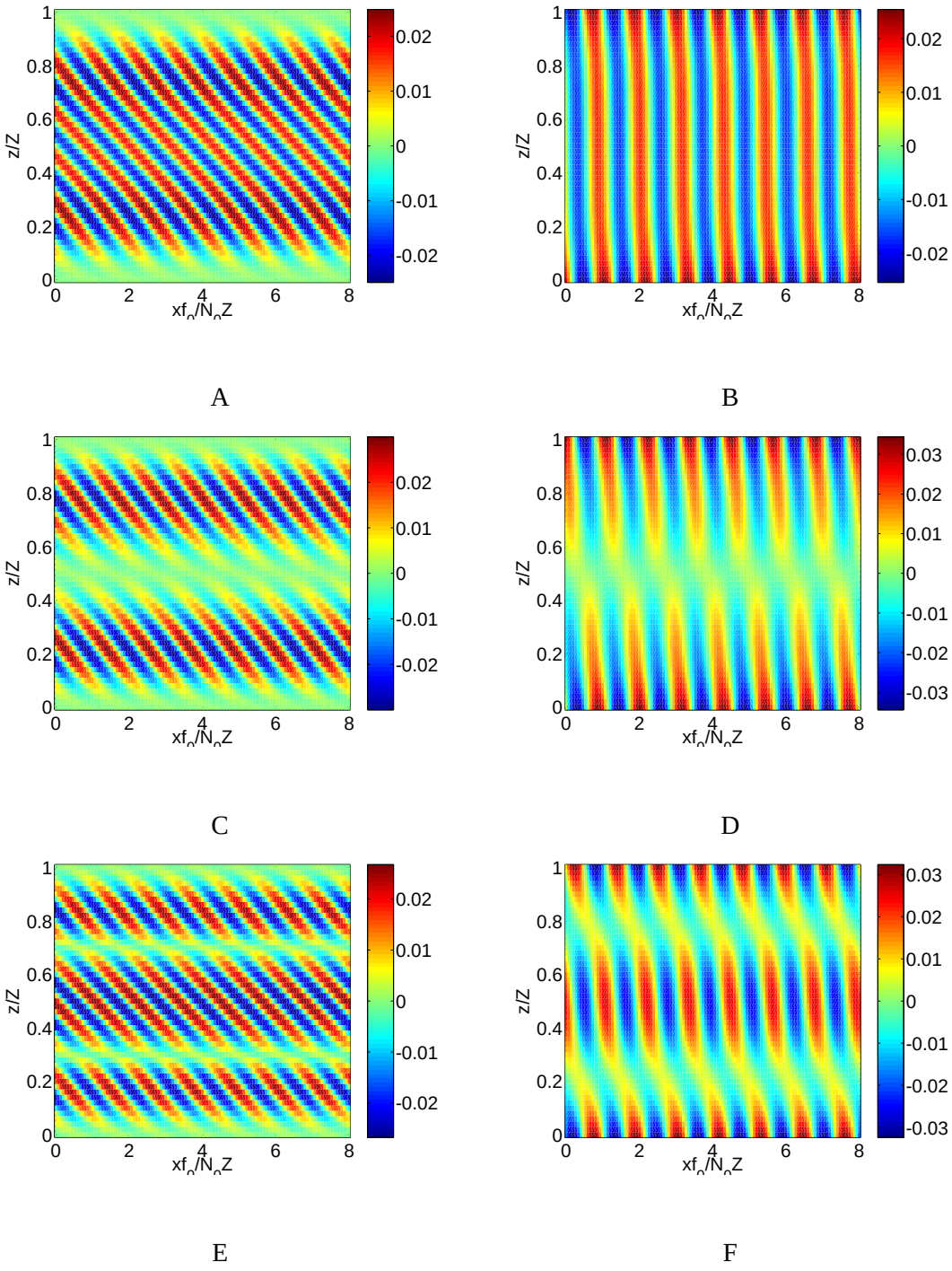

Figure 3.11 *The leading three right and left $48h$ singular vectors, for wavenumber index $n = 7$. A and B first right and left singular vector respectively. C and D second right and left singular vector respectively. E and F third right and left singular vector respectively.*

3.6A and 3.6B the black dashed and dotted lines give theoretical tilt and amplification values for the optimal initial tilt and the Orr initial tilt respectively. Since for the high wavenumbers the first singular vectors have two distinct tilted regions with differing tilts there are two blue lines plotted: the sold blue line refers to the tilt of the potential vorticity in the centre of the domain and the dash-dot line refers to the tilt of the maxima near optimal masking height. Looking first at Figure 3.12A it is noticeable that the initial tilts of the singular vectors both in the centre and at the optimal masking height (blue lines) are significantly smaller than that implied by the optimal and Orr initial tilts. In Figure 3.12B the blue lines denote the theoretical amplification obtained by plane waves with same initial tilts as the singular vectors. The black solid line of Figure 3.12B gives the actual amplification achieved by the singular vectors; i.e. the black solid line shows singular values. It is immediately apparent that the amplification of the singular vectors far exceeds that suggested by their initial tilts. However it must be emphasised that this does not imply that untilting makes no contribution to the overall amplification of the first singular vectors. After-all there is still a relatively large amplitude tilted structure in the centre of the domain which can have little impact on the evolution at the boundaries. What can be said however is that the untilting mechanism no longer has as significant an impact on the leading singular vector structure as was the case for the $12h$ singular vectors.

Figure 3.13 shows the vertical distribution of potential vorticity squared amplitude as a function of wavenumber for the leading singular vectors. The blue line shows the optimal masking height for upper and lower steering levels. In contrast to the $12h$ integration the optimal masking height for wavenumbers below the short-wave cutoff lies in the region which may lead to a large masking effect. For the first singular vectors below the short-wave cutoff the potential vorticity has maxima just below the upper boundary optimal masking height. For the lower boundary the potential vor-

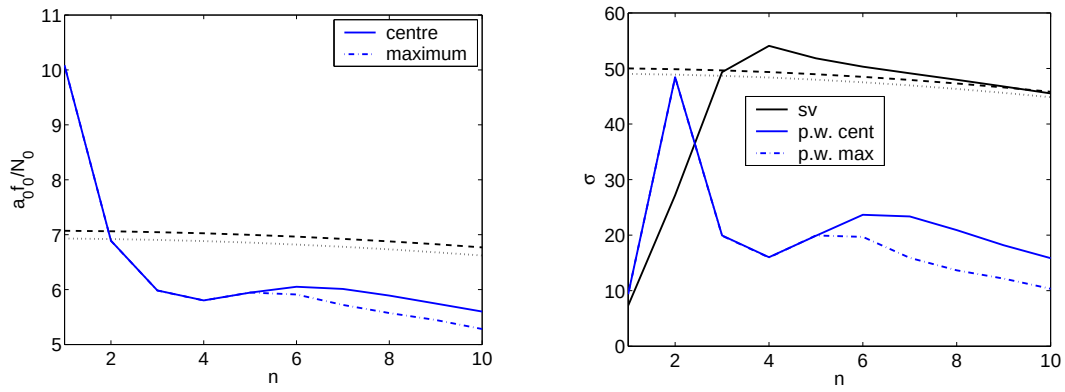

A B

Figure 3.12 *As in Figure 3.6, but for the* $48h$*singular vectors. A: blue line shows the initial tilt (y-axis) of the potential vorticity field associated with the first singular vectors against zonal wavenumber index (x-axis); the solid blue line shows the tilt in the centre of the domain, the dashed blue line shows the tilt at the height the potential vorticity is maximised. B: black solid line shows the leading singular values (y-axis) as a function of zonal wave-index (x-axis); the blue solid line shows the values obtained by substituting the singular vector initial tilt into the plane-wave amplification Equation (3.9). In both A and B, the dashed and doted lines indicate values associated with the optimal and Orr initial tilts, respectively.*

ticity maxima lies just above the optimal masking height. The link between modal masking and concentrations of Eady model singular vector potential vorticity near the steering level has been discussed previously by Morgan and Chen (2002). By contrast De Vries and Opsteegh (2005) stress the importance of neutral mode resonance since they find that the singular vector potential vorticity is always maximised nearer the steering level than the optimal masking height. What is evident from the work presented here is that the importance of modal masking is dependent on the relative sizes of the spatial scales and integration lengths considered. For example the potential vorticity structure of the leading $12h$ singular vectors (Figure 3.7C) does not have maxima near the optimal masking height. This lack of maxima is attributable to the fact that the optimal masking height lies too far from the steering level for there to be significant projection of the continuum modes associated with potential vorticity at that height onto the normal modes. The lack of such potential vorticity maxima does not mean that modal masking does not occur, only that its effects are not large enough to cause significant deviation of the leading singular vector's structure from that of untilting plane-waves concentrated in the centre of the domain. By contrast, the $48h$ integration is long enough that the optimal masking height lies sufficiently close to the steering level for the effects of modal masking on the leading singular vectors to be large. It must be pointed out that the optimal masking height is dependent on both time and wavenumber. The fact that strong effects of modal masking on leading singular vector structure are not seen for the $12h$ integration is in part attributable to the fact that only scales larger than $800km$ are contained in the spectrum. For smaller scales the optimal masking height will be (theoretically) closer to the steering level and modal masking may be significant even for short integration lengths.

Figures 3.14A and 3.14B show the normalised additive amplification of the leading ten singular vectors and the first twenty-five singular values for the $48h$ integration, respectively. For ease

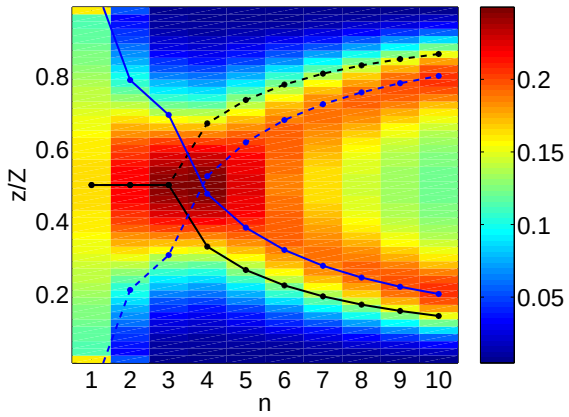

Figure 3.13 *The vertical distribution of potential vorticity squared-amplitude of the first singular $48h$ singular vectors. The y-axis shows height, the x-axis shows zonal wavenumber index. The black and blue lines show the steering level and optimal masking heights respectively.*

of viewing only the $n = 1$, $n = 3$, $n = 5$, $n = 7$ and $n = 9$ singular values are shown in Figure 3.14B. Several things are evident from these figures. Firstly, it can be seen in Figure 3.14A that the magnitude of the singular values descends less rapidly at high wavenumbers than low wavenumbers, as was the case for the $12h$ singular values (although the behaviour is slightly more complex for wavenumbers smaller than the short-wave cutoff value). However, from Figure 3.14B it can be seen that, unlike the $12h$ integration, the magnitude of the leading singular value is not largest in the smallest scales. There are two possible explanations for this change in the dependence of optimal amplification on zonal scale. Firstly this may be attributable to the limited vertical resolution of the model. Essentially since the model has limited vertical resolution the resolvable tilts are also limited and for small zonal wavenumbers the limitations on tilt are more severe; Mukougawa and Ikeda (1994). The fact that the optimal amplification is lower at the smallest scales may be attributable to a reduction in the amplification attributable to the untilting mechanism. A second explanation for this difference between optimal amplification over a $12h$ and $48h$ integration is the variation in the structure of the continuum and normal modes with

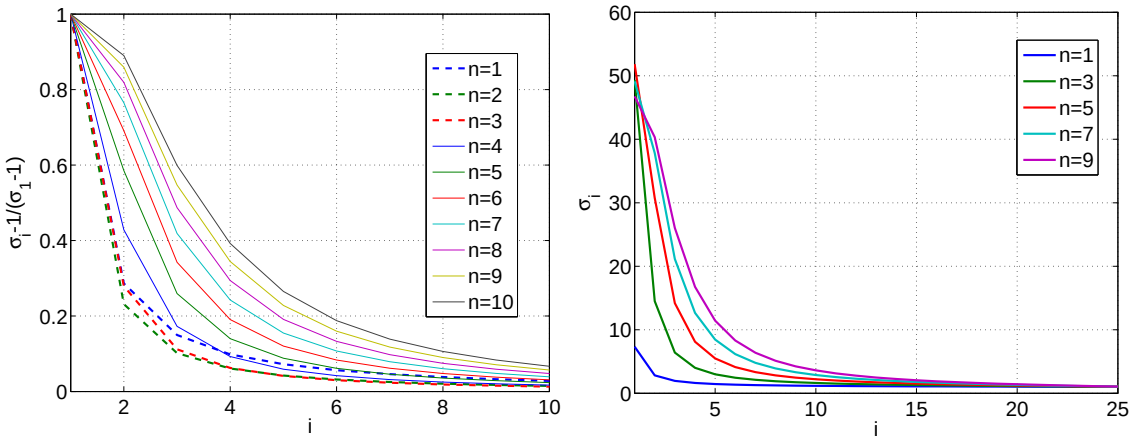

A B

Figure 3.14 *A: The normalised additive amplification of the singular vectors, as a function of singular value index, for a* $12h$ *integration. Each line represents a different zonal wavenumber. B: The* $48h$ *singular values. Each line corresponds to a different zonal wavenumber.*

zonal wavenumber. For high wavenumbers the normal and continuum modes are more confined in the vertical and therefore interact in a smaller region. By contrast at lower wavenumbers there structure is more 'spread out' in the vertical so interact over a larger part of the model domain. The limitation of the interaction at smaller scales to a smaller region of the domain may also lead to a limitation in the maximum amplification. Which, if either, of these explanations is correct will not be answered in the present work. What can be said however is that the difference in optimal amplification between the different wavenumbers (apart from the lowest) is small relative the magnitude of the amplification. Furthermore it shall be seen in the next chapter, that due to the less rapid decent of the singular values associated with small scale singular vectors the cumulative effect of all the singular vectors is still greater at smaller scales.

To gain further insight into the $48h$ growing singular vectors as a whole we shall look more closely at the $n = 7$ singular vectors. Figures 3.15A and 3.15B show the streamfunction squared ampli-

tude of the first ten initial (right) and final (left) singular vectors respectively. In Figure 3.15B the singular vectors have been weighted by the singular values. Several things are noticeable from Figures 3.15A and 3.15B. Firstly the leading few singular vectors are associated with a transfer of amplitude from below the steering level to the upper and lower boundaries. By contrast the streamfunction amplitude of the lower order singular vectors is similarly distributed throughout the domain at both initial and final time. Whilst the leading few singular vectors have large amplitude maxima in the region just below the steering level the lower order singular vectors show a slight weakening of amplitude in this region relative to the rest of the domain. For reference Figure 3.15C shows the potential vorticity squared amplitude. In Figure 3.15C it can also be seen that whilst the leading few singular vectors have large potential vorticity amplitude in the region associated with unmasking effects the lower order singular vectors have a weakening of potential vorticity in the 'unmasking region'. This difference structure in the unmasking region of the leading few and lower order singular suggests that the modal masking/unmasking mechanism leads to amplification in only the few leading singular vectors.

Figure 3.16A shows the initial tilts of the first ten $n = 7$ singular vectors. The 'behaviour' of the tilts differs from that of the $12h$ singular vectors in that the tilts do not increase linearly with the initial tilt of the first singular vector being close to the optimal initial tilt. The tilts of the first two singular vectors are similar and significantly smaller than the optimal initial tilt. After the first two singular vectors the initial tilt increases linearly with at a rate similar ($\sim 0.8 f_0/N_0$) to the $12h$, untilting dominated, singular vectors. Figure 3.16B shows the singular values and the value obtained from substituting the associated initial tilts of the singular vectors into the untilting amplification equation. For the leading few singular vectors the singular values differ radically from the amplification inferred from the untilting mechanism. For the lower order singular vectors

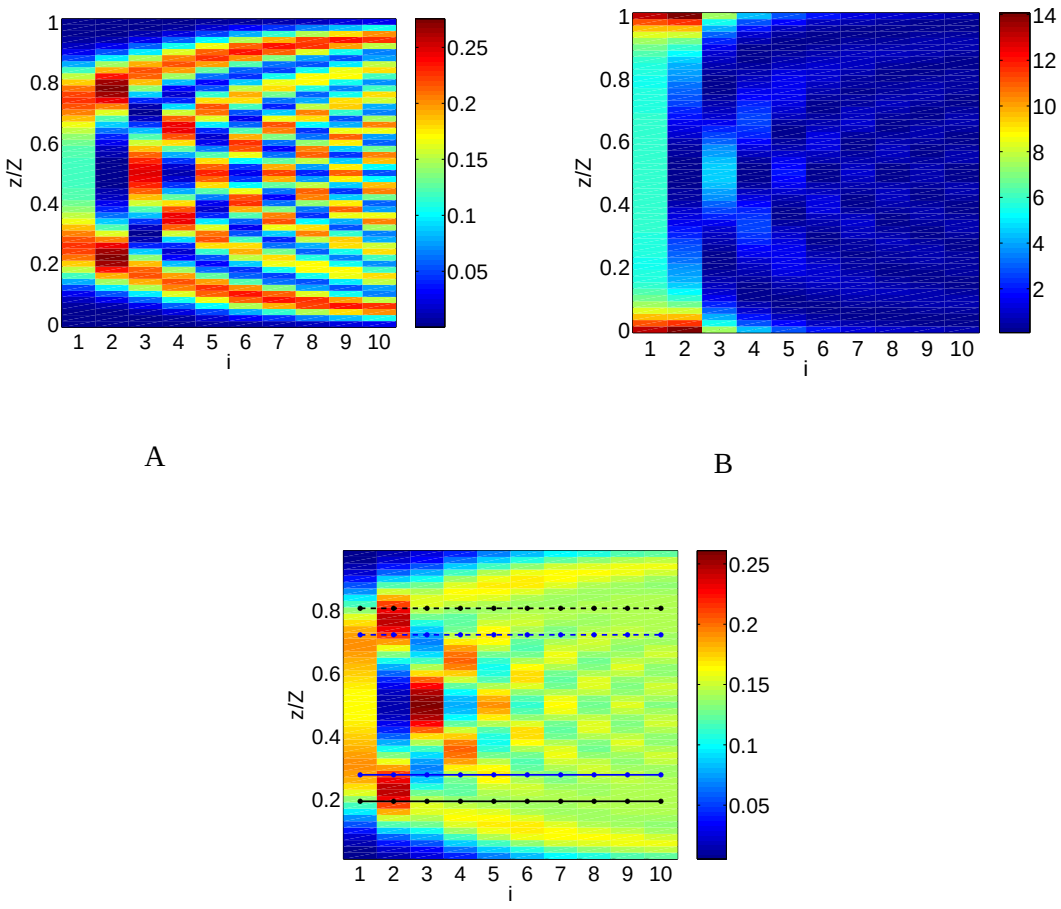

Figure 3.15 *A: The streamfunction squared-amplitude as a function of height (y-axis) for the first ten $n = 7$ right singular vectors. B: The streamfunction squared-amplitude as a function of height (y-axis) for the first ten $n = 7$ left singular vectors, weighted by singular value squared. C: The potential vorticity squared-amplitude as a function of height (y-axis) for the first ten $n = 7$ right singular vectors; blue and black lines show the locations of the optimal masking height and the steering level respectively.*

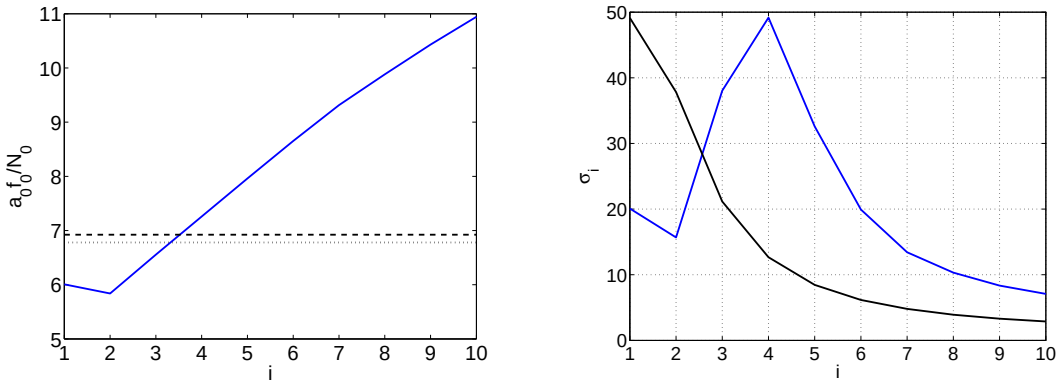

A B

Figure 3.16 *A: The initial tilts (y-axis) of the $48h$ $n = 7$ singular vectors; x-axis shows the singular vector index; the dotted and dashed black lines show the Orr and optimal initial tilts respectively. B: The black line shows the $48h$ $n = 7$ singular values, the blue line shows the amplification implied by substituting the initial tilts of the singular vectors into the plane-wave amplification Equation (3.9).*

the behaviour is qualitatively more similar to that suggested by the untilting mechanism. The fact that the lower order singular vectors do not lead to disproportionately large amplification on the boundaries and that aside from the leading few singular vectors the initial tilt follows a similar pattern to that of the $12h$ singular vectors suggests that modal unmasking does not play a significant role in any but the leading few singular vectors.

3.5 Summary

In this chapter we have examined the singular vectors of the 2D Eady model. Roughly speaking we can infer the existence of two dynamical regimes for singular vectors. For short integration lengths the untilting mechanism dominates the amplification. For the intermediate integration

lengths, the modal unmasking mechanism is the dominant cause of amplification. In the next chapter we shall discuss the implications of these two dynamical regimes to singular vector targeting, but first we shall summarise the main characteristics of the two regimes.

In the untilting regime, the properties of the singular vectors may be summarised thus. The maximum amplification occurs at the shortest wavelengths. Additionally, the rate with which the amplification decreases with increasing singular vector index is slower at smaller zonal wavelengths. The net result of this is that the 'average' amplification of smaller zonal scales is greater than longer scales. For the untilting mechanism both the initial and final amplitudes tend to concentrated in the central vertical levels of the domain.

During the modal unmasking regime, the maximum amplification is not necessarily achieved by the smallest zonal wavenumber. For singular vectors which amplify via modal unmasking the initial amplitude is concentrated near the steering level and the final amplitude is concentrated on the boundaries. The transition from an untilting to a modal masking regime occurs when the integration length is sufficient for a π phase change to occur in the relative phases of the normal modes and the continuum modes near the steering level. This requirement implies that modal unmasking will become significant more rapidly at small zonal scales than at large zonal scales. However, since the modal masking regime relies on the normal modes, it cannot explain the growth of more than a few singular vectors. Consequently even though modal unmasking is significant in determining the structure of the leading singular vectors, during the modal unmasking regime the untilting mechanism is still important to the singular vector amplification as a whole.

CHAPTER 4

Identification of the location of greatest sensitivity using Singular Vectors

4.1 Introduction

In the last chapter we discussed the dynamics of the singular vectors in the Eady model. In this chapter we shall examine the relationship between these singular vectors and the singular vector targeting method of Buizza and Montani (1999). The method of Buizza and Montani (1999) uses the singular vectors to identify regions which are deemed 'sensitive' to small changes in the atmospheric state. Essentially, these 'sensitive regions' are those in which small perturbations in the model state at an observation time, t_1, are likely to grow into large perturbations within a local 'verification region' at a later 'verification time', t_2. In singular vector targeting, sensitivity maps are produced. These sensitivity maps attribute numeric sensitivity values to each geographic location, and the observations are targeted to regions in which these numeric sensitivity values are large. The sensitivity maps are produced in 'plan view' by integrating the sensitivity in the vertical, to attribute a sensitivity value to each latitude-longitude location. In the present chapter, as well as looking at the vertically integrated sensitivity, we shall look at the zonally integrated sensitivity and sensitivity maps produced for the zonal-height and spectral-height planes; i.e. attributing each longitude-height location and each zonal wavenumber-height location a sensitivity value. Whilst singular vectors themselves have been considered in vertical cross-section [e.g.

Hoskins et al. (2000), Montani and Thorpe (2002)], the links between these singular vectors and the calculation of sensitive regions have not been explicitly considered. By considering the sensitivity in these different phase-planes we shall infer several points about the relationship between the singular vector dynamics and the sensitivity in different locations.

Here it is worth re-iterating that the streamfunction norm used to compute the singular vectors yields singular vectors identical to those that would result from a kinetic energy norm; Kim and Morgan (2002). Since the streamfunction and kinetic energy norms give rise to identical singular vectors all results in this chapter are consistent with either choice of norm; essentially by replacing the word streamfunction with the word velocity throughout the chapter one can read the equivalent analysis for kinetic energy. Since the structure of total energy and kinetic energy singular vectors are found to be very similar in both the Eady model [Kim and Morgan (2002)] and more complex models [Palmer et al. (1998)], it can be inferred that the streamfunction based sensitivity maps considered in this chapter are consistent (in terms of the norm) with the total energy singular vectors commonly employed in singular vector targeting.

As in the previous chapter, we shall constrain our discussions to only a $12h$ and $48h$ integration. We shall consider first sensitivity calculated for the non-locally projected singular vectors discussed in the previous chapter. We shall then turn our attention to sensitivity calculated for a local 'verification region', using locally projected singular vectors. We shall see that the difference in the dominant dynamical mechanisms of these two integrations leads to differences in the distribution of 'sensitivity' at the initial time. For the non-locally projected singular vectors, these difference manifest themselves in the vertical distribution of sensitivity. For the $12h$ integration which is dominated by untilting, the sensitivity is maximised in the central vertical levels of the domain. By contrast, for the modal unmasking dominated $48h$ integration, the sensitivity is max-

imised in two peaks close to the upper and lower boundary steering levels. In both cases however the sensitivity remains greatest at shorter wavelengths. For the locally projected singular vectors we shall see that the transition from the untilting regime to that modal unmasking regime is also associated with changes in the zonal distribution of sensitivity.

4.2 Sensitivity based targeting function

The use of singular vectors in targeting has usually been motivated from the perspective of sensitivity or instability of the dynamical model in a particular region. The motivation being that, by correcting the initial conditions in the region in which the subsequent forecast is most sensitive to random excitation, it is expected that the forecast error will be maximally reduced. To be more explicit the observations are deployed in regions where it is expected that randomly perturbing the initial conditions will cause the greatest difference between the 'perturbed' and 'unperturbed' forecasts. For clarity, the term random perturbation in this context refers to a vector who's elements are drawn from a symmetric statistical distribution with zero mean, and variance γ. In this section, we shall introduce a useful version of the 'typical' implementation of singular vector targeting which will be applied to the Eady singular vectors computed in the previous chapter. Here we use the word 'typical' since the implementation of 'singular vector targeting' varies somewhat between publications.

Given a localised random perturbation, $T_1\boldsymbol{\delta\chi}_1$, to the model state at t_1, we define the evolved perturbation to be

$$\boldsymbol{\delta\chi}_2(T_1) = MT_1\boldsymbol{\delta\chi}_1. \tag{4.1}$$

$\boldsymbol{\delta\chi}_1$ is a random vector whose elements are drawn from a zero mean symmetric statistical distribution with variance γ. The vector $T_1\boldsymbol{\delta\chi}_1$ has random elements in the region defined by the local projection T_1 and is zero outside this region. The evolved perturbation $\boldsymbol{\delta\chi}_2(T_1)$ is defined as a function of the local projection T_1 since it varies with T_1 although $\boldsymbol{\delta\chi}_1$ does not vary with T_1. With the above definitions the expected norm-squared amplitude of the perturbation $T_2\boldsymbol{\delta\chi}_2(T_1)$ is given by

$$\mathcal{E}\left[\|T_2\boldsymbol{\delta\chi}_2(T_1)\|^2_{E_2}\right] = \gamma\sum_{i=1}^{N_g}\sigma_i^2\boldsymbol{v}_i^T T_1\boldsymbol{v}_i, \tag{4.2}$$

where $\boldsymbol{v}_i$ and σ_i are the i^{th} right singular vector and singular value of $E_2^{\frac{1}{2}}T_2ME_1^{-\frac{1}{2}}$ respectively. Equation (4.2) is essentially a prediction of the response in the region defined by T_2 to randomly perturbing the initial conditions in the region defined by T_1. In singular vector targeting, the aim is to identify the local projection T_1 from some restricted set that maximises Equation (4.2). The use of such an expression to define a region for supplementary observations can be motivated by suggesting that, if the inner product at t_1 used to define the singular value decomposition is consistent with the initial condition errors, then Equation (4.2) is a prediction of the expected error variance in the region T_2 at t_2 that has its source in T_1 at t_1; Palmer et al. (1998). The idea being that by placing observations in the region for which $\mathcal{E}\left[\|T_2\boldsymbol{\delta\chi}_2(T_1)\|^2_{E_2}\right]$ is maximised, the reduction in the initial condition errors will lead to the greatest reduction in the forecast error variance in the verification region.

The singular vector targeting found in publications such as Buizza and Montani (1999) and Leutbecher et al. (2002) can be interpreted in terms of Equation (4.2). In these typical implementations of singular vector targeting T_1 is a projection onto all the grid points in the vertical column at a particular latitude-longitude location. The targeting method is implemented by first calculating

the values of Equation (4.2) for every such latitude-longitude location to produce a 'plan-view' map of the sensitivity. The targeting region is then defined to include all latitude-longitude locations for which Equation (4.2) is greater than a certain fraction of the maximum; Buizza and Montani (1999). One point to note is that the targeting described by Buizza and Montani (1999) and Leutbecher et al. (2002) does not conform precisely to Equation (4.2). For example in some cases Buizza and Montani (1999) define a sum the absolute amplitudes of the singular vectors in the region T_1; and Leutbecher et al. (2002) sum over the elements singular vectors transformed to 'total energy variables' regardless of the inner product used in the singular vector computation. Furthermore it must stated that whilst Equation (4.2) has a precise mathematical interpretation, it is not necessarily the case for the singular vector targeting as implemented in publications such as Buizza and Montani (1999) and Leutbecher et al. (2002). We have chosen to formulate the singular targeting method using Equation (4.2) because it has a precise mathematical meaning and enables a clear interpretation of the results of the idealised experiments contained in this work.

4.3 Sensitivity determined using non-locally-projected singular vectors

4.3.1 $12h$ integration

Firstly we consider the twelve hour integration. Figure 4.1 shows a sensitivity map for the height spectral phase plane. In order to produce this sensitivity map all the singular vectors were included in Equation (4.2). Several things are evident from Figure 4.1. Firstly high zonal wavenumbers have far greater sensitivity than low wavenumbers. This can be seen more clearly in Figure

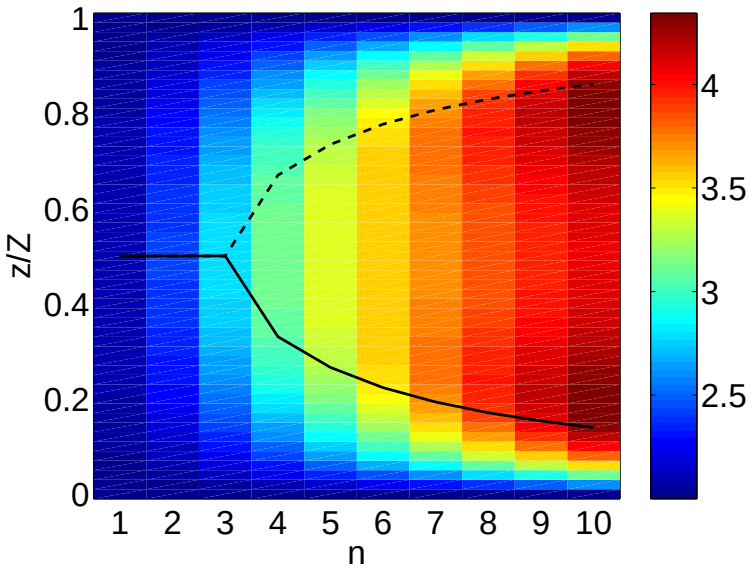

Figure 4.1 *The sensitivity plotted in the height-wavenumber phase plane, for the* $12h$ *integration.*

4.2A which shows the sensitivity map integrated in the vertical. This increased sensitivity in the smallest zonal scales can be interpreted in terms of the singular vectors discussed in Chapter 3.4.2. In terms of the singular vectors there are two contributing factors to the increased sensitivity at small zonal scales. The first is that the amplification of the optimally amplifying singular vector is larger for high wavenumbers than low wavenumbers. The second contributing factor is that the singular values decrease in amplitude less rapidly at smaller zonal scales. Both these points were highlighted in the previous chapter.

The second thing that is evident in Figure 4.1 is that the model is most sensitive in the region approximately bounded by the steering levels. Since the distance between the upper and lower boundary steering levels increases with wavenumber, for high wavenumbers the sensitive area is of greater vertical depth. Figure 4.2B shows the sensitivity as a function of height. From Figure 4.2B it can be seen that the sensitivity is maximised in a nearly uniform region spanning the central half of the domain.

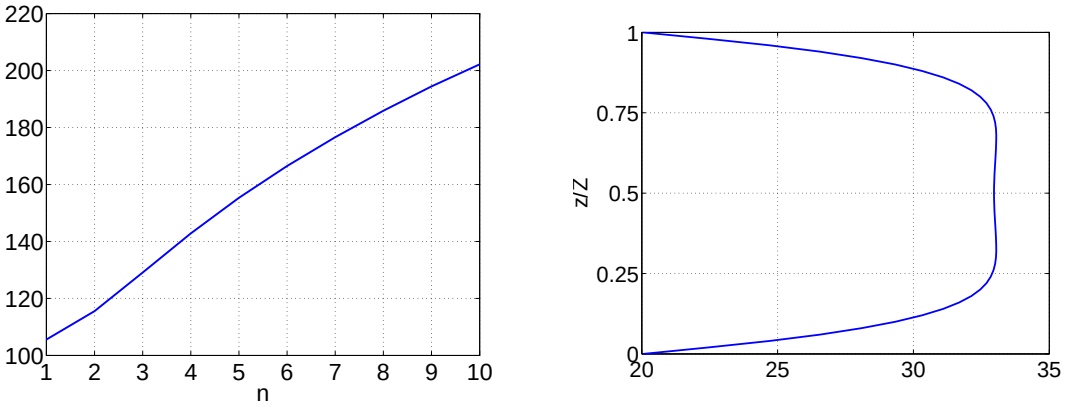

A B

Figure 4.2 *A: The sensitivity as a function of zonal wavenumber, for a* $12h$ *integration (the integral of Figure 4.1 with respect to height). B: The sensitivity as a function of height (the integral of Figure 4.1 with respect to n), for a* $12h$ *integration .*

4.3.2 $48h$ integration

Figure 4.3 shows the wavenumber-height sensitivity map for the $48h$ integration. The effects of modal masking on Figure 4.3 are clear. The fact that the sensitivity peaks in the region just below (above) the upper (lower) boundary steering levels can be understood in terms of the structure of the leading singular vectors. Since the steering level height varies with wavenumber, the zonal scale of perturbation to which the model is most sensitive varies with height. The central vertical levels are dominated by the intermediate scales, whereas the lower and upper levels are dominated by the small scales. Since the appearance of these areas of high sensitivity near the steering level is associated with unmasking of the normal modes, at the end of the integration period the variance resides predominantly at the upper and lower boundaries. However it must be noted that although the sensitivity is dominated by the modal unmasking mechanism, there is still significant sensitivity to high wavenumber perturbations on the central vertical levels of the domain. This sensitivity to high wavenumber perturbations in the centre of the domain indicates that untilting

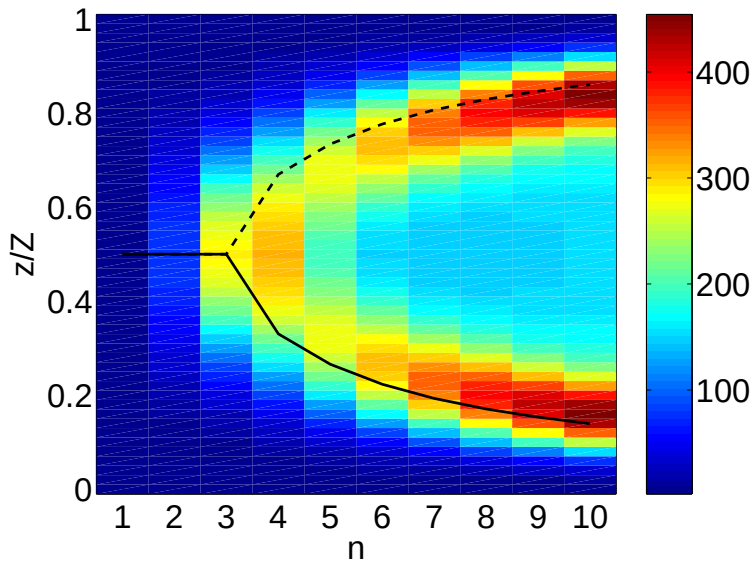

Figure 4.3 *The sensitivity plotted in the height-wavenumber phase plane, for the* $48h$ *integration.*

is still of significance. Whilst the sensitivity of the central vertical levels is peaked at the intermediate zonal scales, it must be noted that the cumulative contribution to the sensitivity in the centre of the domain from the untilting of small scales is of similar magnitude to that the intermediate scales.

Figures 4.4A and 4.4B show the sensitivity as a function of wavenumber and height respectively. From Figure 4.4A one can see that the sensitivity is peaked in the smallest zonal scales. From Figure 4.4B one can see that the result of the transition from an untilting regime to a modal unmasking regime is the appearance of two distinct peaks in the vertical sensitivity distribution. In the next section we shall see that for sensitivity computed using zonally localised singular vectors, this change in vertical sensitivity distribution, results in a change in the zonal sensitivity distribution.

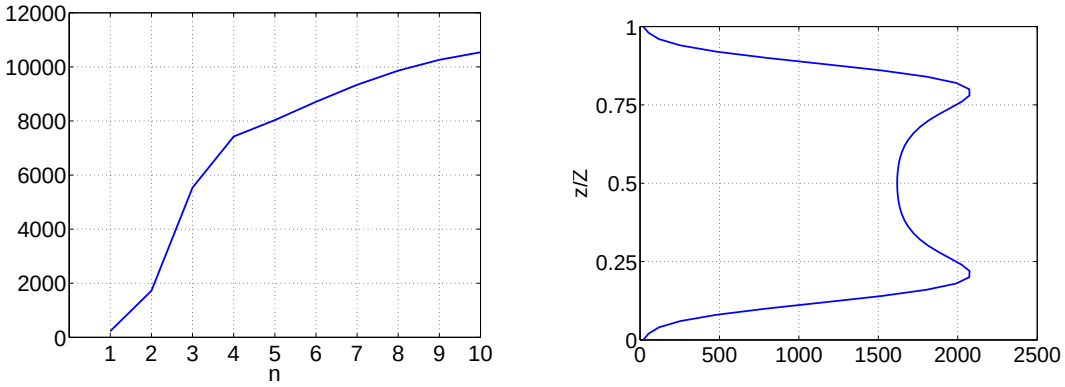

A B

Figure 4.4 *A: The sensitivity as a function of zonal wavenumber (the integral of Figure 4.3 with respect to height), for a $48h$ integration. B: The sensitivity as a function of height (the integral of Figure 4.3 with respect to n), for a $48h$ integration.*

4.4 Sensitivity determined using locally projected singular vectors

4.4.1 Singular value decomposition

Previously we have computed the singular value decomposition of the Eady model integral propagator without any local projection operator. In this section we shall be computing the singular vectors with a final time local projection operator. Our main purpose is to demonstrate the effect of the local projection on the sensitivity measure discussed earlier in the present chapter. However, prior to this we shall define the mathematical formalism of the singular value decomposition and discuss briefly the character of the computed singular vectors.

As with the non-locally projected singular vectors we shall use the matrix $L \in \mathbb{R}^{N_g \times N_g}$ to denote an the integral propagator of an initial *grid-point* streamfunction field to the corresponding final *grid-point* streamfunction field. The final time local projection is performed by the matrix $P \in \mathbb{R}^{N_r \times N_g}$. In addition to these two matrices, an additional initial time Fourier filter matrix

$F \in \mathbb{R}^{2N_k \times N_g}$ is used to prevent the inclusion of wavenumbers lower than $k_n = 10$. This additional matrix is necessary since the grid-point resolution of the model is higher than that implied by the spectral space spanned by the first ten wavenumbers. Whilst the unprojected singular vectors all contain a single zonal wavenumber, the locally projected singular vectors are comprised of multiple zonal wavenumbers. For the unprojected singular value decomposition the Fourier filter matrix was also used, however it made no difference to the structure the singular vectors, other than to set the singular values associated with shortwave singular vectors to zero. The locally projected singular vectors, however, have multiple zonal wavenumbers in individual vectors. Since the singular vectors contain multiple zonal wavenumbers, the structure of the singular vectors differs from those computed without the Fourier filter. Utilising both the initial Fourier filter and the final local projection singular value decomposition is defined

$$PLF^T F = \sum_{i=1}^{rank(PLF^T F)} \sigma_i \boldsymbol{u}_i \boldsymbol{v}_i^T. \tag{4.3}$$

Detailed discussion of the structure of the locally projected singular vectors will not be given. We shall however summarise the basic properties here. The local projection matrix is used to define the verification region. For all numerical experiments presented in this thesis the verification region shall be a region of zonal extent NZ/f_0 and height Z; i.e. a region of one Rossby radius zonally which occupies the full height of the domain. For reference, Figure 4.5A shows the first right locally projected singular vector for the $12h$ integration. The vertical black lines denote the boundaries of the verification region. Figure 4.5B shows the first right locally projected singular vector for the $48h$ integration. From Figures 4.5A and 4.5B the effects of the final local projection on the singular vector structure can be seen. The amplitude of the singular vectors are concentrated in a tilted region of similar width to the verification region. The tilt of the region

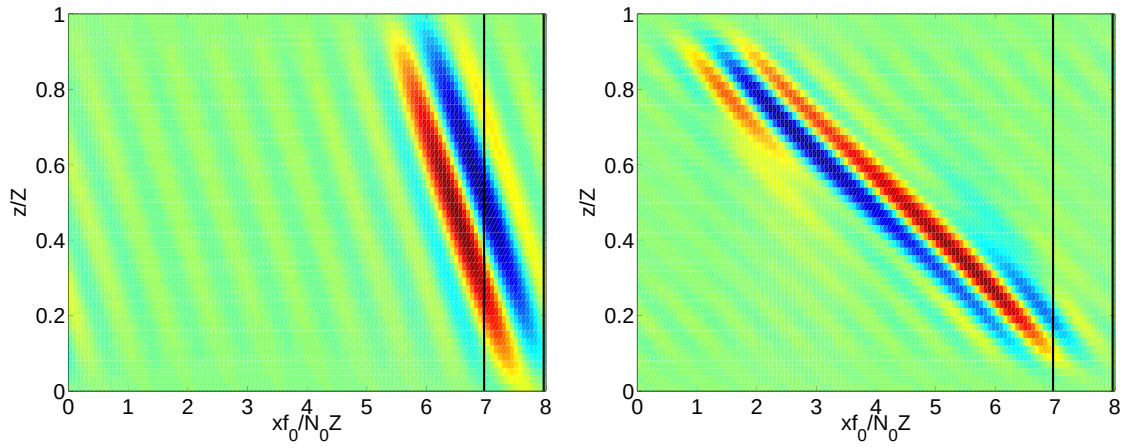

Figure 4.5 *Examples of first right locally projected Eady model singular vectors. Black vertical lines denote the boundaries of the verification region. A:* $12h$ *integration. B:* $48h$ *integration.*

is larger for longer integration lengths. From a dynamical point of view this is not particularly surprising since, as was seen in the previous chapter, the streamfunction field of the singular vectors is strongly connected to the potential vorticity field. Due to the conservative advection of the potential vorticity by the sheared mean zonal wind, the potential vorticity perturbations in the tilted region will be advected into the vicinity of the verification region by the end of the integration. Consequently the streamfunction field is also concentrated in the vicinity of the verification region at the end of the integration. Since for longer integration lengths the potential vorticity will travel further over the integration, the tilt of the region is larger. Another property of the locally projected singular vectors that differs from that of the unprojected singular vectors is that the locally projected singular vectors contain multiple zonal wavenumbers. As an example Figure 4.6A shows the streamfunction-squared amplitude of the first right $12h$ singular vector as a function height and wavenumbers.

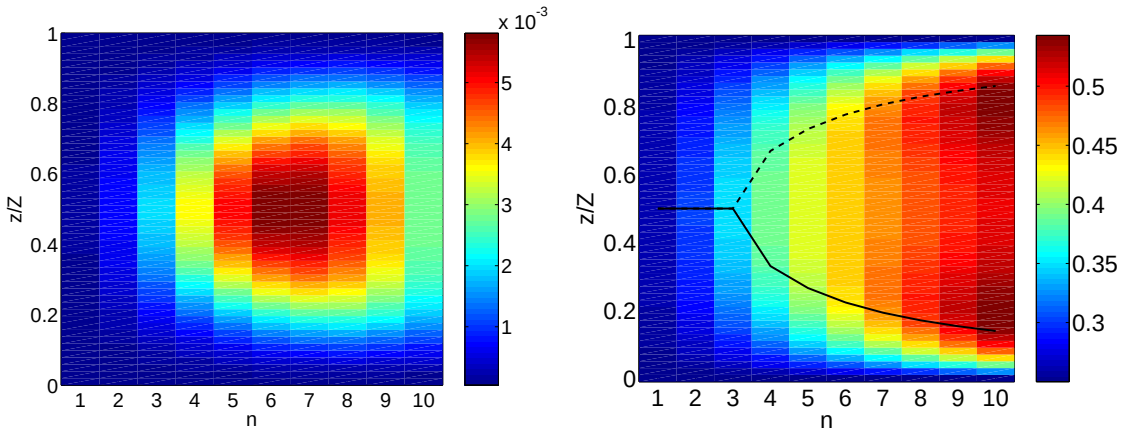

Figure 4.6 *A: The streamfunction squared-amplitude of the first right locally projected* $12h$ *singular vector. B: The sensitivity in the height-wavenumber phase plane computed from the* $12h$ *locally projected singular vectors.*

4.4.2 Invariance of the spectral-height phase-plane sensitivity, to zonal localisations

The local projection defined in the previous section localises only the zonal coordinate, and not the vertical coordinate. It has already been seen that the localisation changes the structure of the singular vectors. Despite the change in singular vector structure, zonal localisation does not alter the sensitivity of the model when viewed in the spectral-height phase plane. To illustrate this point, Figure 4.6B shows the sensitivity computed from the $12h$ locally projected singular vectors plotted in the spectral-height phase plane. Comparing Figure 4.6B to the equivalent computed with unprojected singular vectors (Figure 4.1) it is apparent that the two are identical up to a multiplicative constant. This multiplicative constant is related to the zonal extent (measured in grid-points) of the verification region, and is given by N_v/N_x, where N_v is the number of gridpoints in the verification region.

Since the locally projected singular vectors and non-locally projected singular vectors produce identical sensitivity patterns in the spectral-height plane, we can infer that the dynamical properties of these two singular vector spectra *as whole* are identical, even if individually the singular vectors differ in a appearance. Due to this similarity, when considering the dynamics from a wave perspective, we may utilise the analysis of the dynamical properties of Eady model singular vectors given in the previous chapter in discussions of the sensitivity patterns generated by the locally projected singular vectors. It should also be noted that when considering the sensitivity as a function of wavenumber, and as a function of height, the sensitivity pattern obtained with the locally projected singular vectors is also identical (up to a multiplicative constant) to those obtained using the unprojected singular vectors shown in Figures 4.2A and 4.2B respectively.

4.4.3 Introduction of height-zonal correlation by zonal localisation

In this section we shall look at the sensitivity computed using the locally projected singular vectors in zonal-height plane. Firstly we shall look at some of the general properties of the sensitivity patterns in the zonal-height plane. Figures 4.7A and 4.8A show the zonal-height plane sensitivity pattern, computed for a $12h$ and $48h$ integration respectively. For both integrations the sensitivity lies in a tilted region of width approximately equal to the width of the verification region. From a potential vorticity dynamics perspective, the sensitive region lies in the region from which the potential vorticity will have been advected into the verification region at the end of the integration. In a sense one could say that the sensitivity is 'untilted' over the integration length.

As a result of the tilted structure of the sensitive region different zonal locations are colocated with regions of sensitivity at different heights. For example looking at Figure 4.8A, one can say that at $xf_0/N_0H = 4$ the sensitivity occurs at the central height of the domain, whereas at

$xf_0/N_0H = 2$ the sensitivity occurs at $z/Z \sim 0.8$. In this way we can attribute zonal variations in sensitivity to vertical changes in the sensitivity, and hence attribute the sensitivity at different zonal locations to different growth mechanisms and zonal scales. Here it is worth emphasising that we use the term scale rather than wavelength/wavenumber since by definition the variations in sensitivity we are referring to must be constructed of multiple wavelengths. To illustrate this, Figures 4.7B and 4.8B show the sensitivity as a function of zonal coordinate for the $12h$ and $48h$ integrations respectively. For the $12h$ integration, there is a single peak corresponding to the sensitive region at the central height of the domain. The fact that the greatest sensitivity occurs in the centre of the domain is attributable to the fact that potential vorticity unshielding is the dominant growth mechanism for the singular vectors. By contrast, for the $48h$ integration (Figure 4.8B) there are two peaks. These two peaks correspond to the sensitive regions near the upper and lower boundary steering levels of the shortest wavelengths. The two peaks are therefore associated with the modal unmasking of the shortwave normal modes. To see this explicitly Figure 4.9 shows the sensitivity plotted with the shortwaves filtered out via a Fourier filter. Each line in Figure 4.9 gives the sensitivity calculated with the the scales smaller than wave index n filtered from the singular vectors; for example the $n = 1$ line contains only the longest wave, whereas the $n = 10$ line contains all ten wavenumbers and is identical to that shown in Figure 4.8B. From Figure 4.9 it can be seen that the longest zonal wavelengths are associated with sensitivity between the two peaks in Figure 4.8B and the double peak does not appear until the smaller scales are added to the sensitivity calculation. The implication is that the location of the peaks corresponds to a region where the verification region forecast is highly sensitive to changes in the small scales close to the upper and lower boundary steering level. Between the peaks the forecast in the verification region is less sensitive to changes in the small scales, but is however more sensitive to changes in the large scales than at the peaks.

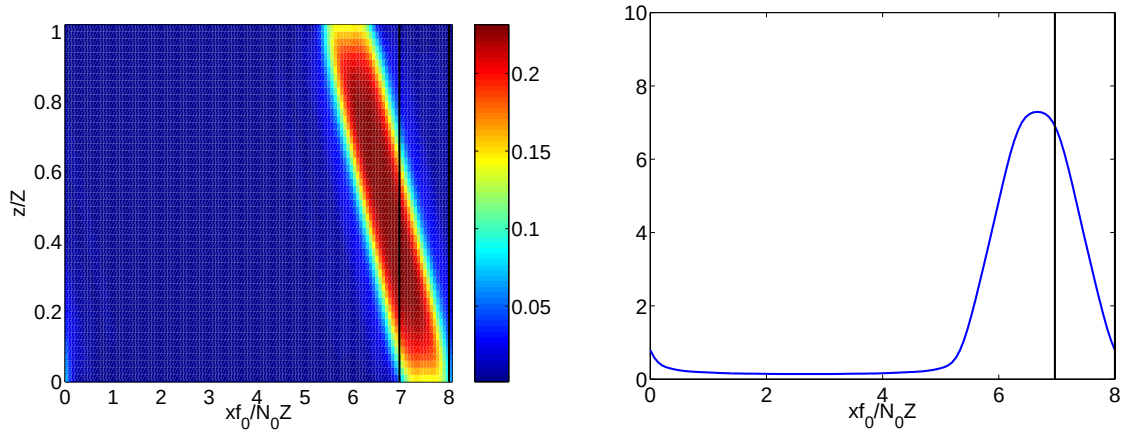

A B

Figure 4.7 *A: The sensitivity in the height zonal plane computed using the* $12h$ *locally projected singular vectors. B: The sensitivity as a function of the zonal coordinate, computed using the* $12h$ *locally projected singular vectors.*

Another noticeable feature of Figure 4.9 is that the peaks in sensitivity gradually separate as smaller and smaller scales are added to the sensitivity calculation. This separation is attributable to the fact that peak in sensitivity for each wavenumber resides close to the steering level. Since the separation between the two steering levels increases with wavenumber, so does the vertical separation of the sensitivity peaks. Due to the tilted structure of the sensitivity, these changes in vertical separation also lead to changes in zonal separation. This behaviour marks a difference between the untilting and modal unmasking regimes. For the untilting regime, since the sensitivity is maximum in roughly the central vertical levels, the zonal location of greatest sensitivity is roughly the same for all zonal scales. By contrast, the modal unmasking regime is characterised by variations in the zonal location of greatest sensitivity with zonal scale.

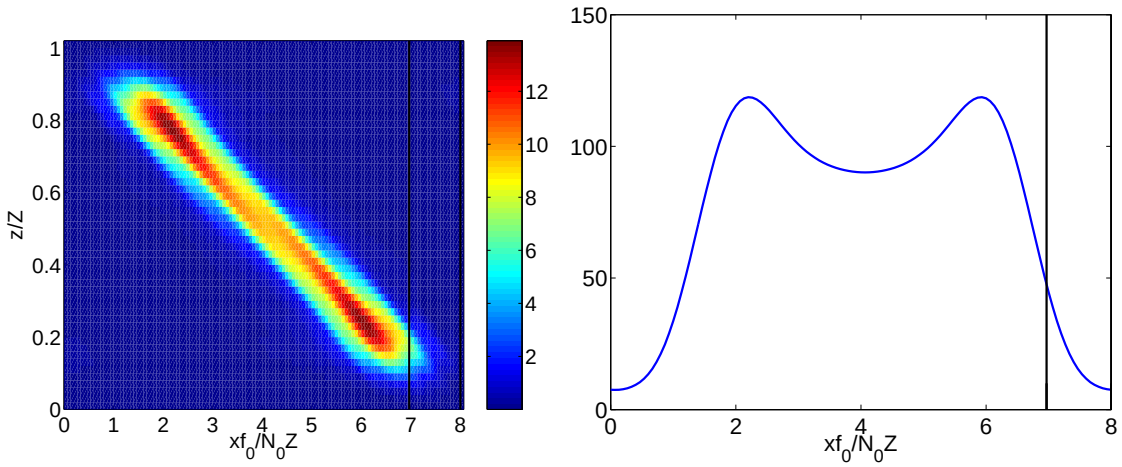

Figure 4.8 *A: The sensitivity in the height zonal plane computed using the* $48h$ *locally projected singular vectors. B: The sensitivity as a function of the zonal coordinate, computed using the* $48h$ *locally projected singular vectors.*

4.5 Summary

In this chapter we have considered the sensitivity based singular vector targeting function of Buizza and Montani (1999) in the context of the Eady model singular vectors computed in the previous chapter. In the next chapter we shall introduce an extension to the singular vector targeting method, that takes account of the data assimilation process, and the dynamical evolution of errors prior to the forecast initialisation time t_1. Firstly, we shall summarise the findings of the present chapter.

The difference between the dynamical regimes of the short $12h$ and intermediate $48h$ integrations leads to difference in the vertical distribution of sensitivity. In the case of the short integration, untilting is the dominant growth mechanism, and consequently the sensitivity is concentrated in the central vertical levels of the domain. By contrast for the intermediate integration the modal

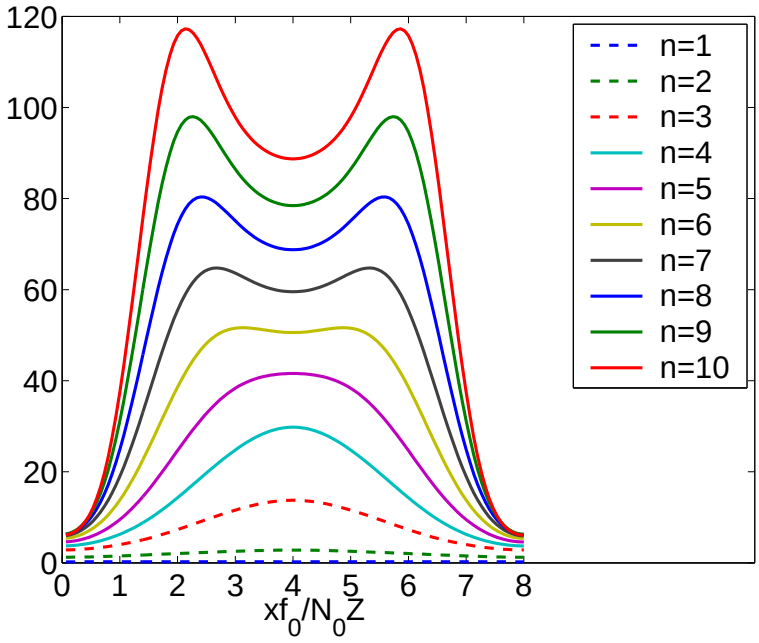

Figure 4.9 *The sensitivity as a function of the zonal coordinate, computed using the $48h$ locally projected singular vectors. The sensitivity is computed with the small zonal wavenumbers filtered out. Each line corresponds to a different level of filtering, so for example, the $n = 1$ line contains only the longest zonal wavelength and the $n = 10$ line contains all zonal wavelengths. N.B. the $n = 10$ line is identical to Figure 4.8B.*

unmasking is the dominant growth mechanism, and consequently the sensitivity is concentrated in two peaks near the upper and lower boundary steering levels of the shortest resolved zonal wavelengths.

When the sensitivity to initial perturbations of a zonally localised verification region is considered, the difference between the two dynamical regimes of the short and intermediate integration leads to differences in the zonal distribution of the sensitivity. These differences occur because the sensitivity at a particular zonal location corresponds to the sensitivity of a small number of vertical levels. Essentially this means that, when untilting is the dominant mechanism and the sensitivity is greatest in the central vertical levels, the sensitivity is greatest at the zonal location whose sensitivity depends the sensitivity of the central vertical levels. By contrast when the modal unmasking regime is entered, the sensitivity is greatest at zonal locations whose sensitivity depends the sensitivity of the vertical levels near to the upper and lower boundary steering levels. Consequently for the untilting regime there is a single peak, whereas, when the modal unmasking regime is entered, this peak separates into two zonally separated peaks.

CHAPTER 5

A singular vector targeting method that introduces dynamic estimates of the initial condition errors

In this chapter we shall define an A-optimal [Berliner et al. (1999)] targeting method which utilises singular vectors to obtain a reduced rank prediction of the observation locations that will be of greatest benefit to the accuracy of the subsequent forecast. Rather than rely on the initial normalising matrix E_1, (following Berliner et al. (1999)) we shall approximate the initial condition error statistics at time t_1 by a transformation of a dynamically evolved background error covariance matrix. Unlike Berliner et al. (1999), however, we shall define this transformation to be consistent with the operational data assimilation system, and not an ensemble Kalman filter. This difference in choice of transformation, leads to a significantly different final result.

By assuming an operational Kalman Filter, Berliner et al. (1999) arrive at a targeting function that models the response obtained if the operational data assimilation were able to spread information along the eigenvectors of the dynamically evolved background error covariance matrix. By contrast, in the analysis presented in this chapter, we shall assume that the data assimilation system contains a pre-specified model of the background error covariance which is not generally consistent with the estimated actual covariance matrix. Making this assumption we shall define a targeting function, the operation of which is summed up by Equation (5.18). The method essentially finds the difference between the predicted forecast error variance, with and without the observations, allowing for the fact that observations may increase or decrease the forecast error.

This work can be motivated by Bergot (2001), in which it is found that the impact of the targeted observations is highly dependent on the quality of the background field. It is important therefore that any targeting method should incorporate information about the background errors. Bergot (2001) also find that only in cases where the observations were collocated with regions in which the singular vectors used in targeting had non-negligible amplitude, do they have an effect on the forecast error. This requirement of collocation with the region spanned by the targeted singular vectors indicates that observations should not be placed outside this region. It is important to note however that requiring observations to be collocated with the targeted singular vectors is not the same as requiring that observations be located at the locations where the singular vectors have maximum amplitude; i.e. it is not a statement that the singular vector method described in the previous chapter is the best means of selecting observation locations. It is simply that regions where the singular vectors have negligible amplitude are dynamically disconnected from the verification region. Bergot (2001) also find that the effectiveness of targeted observations depends on the data assimilation system. It is therefore likely that consistency of the targeting method with the operational data assimilation system is important.

In this chapter we shall first outline the statistical formulation of the targeting method. We shall then consider how this targeting method may be approximated using singular vectors. Then we shall consider the means by which the targeting method may be made consistent with a hypothetical operational data assimilation system. In the final section of this chapter we shall demonstrate a simplified implementation of this targeting method in the Eady model, and discuss the connection between the target locations calculated and the dynamical analysis of the contained in the previous chapters.

5.1 Basic formulation of a targeting method

In this section we define the basis for a targeting method. To form the basis of the method we make the assumption that the expected background error covariance matrix at t_1 evolves from the identity matrix at an earlier time t_0, and that the error evolution from t_0 to t_2 is linear. With these assumptions a basic statistical formulation for the targeting method follows in a similar fashion to that of Berliner et al. (1999). There is one significant difference between the statistical formulation of Berliner et al. (1999) and that which we outline here. This difference is that whilst Berliner et al. (1999) make the assumption that the observations are assimilated using an (extended) Kalman filter, we make no such assumption. Rather than use the Kalman filter equations, we define a matrix which is assumed in some way to approximate the gain matrix (response function) of the operational data assimilation system.

We shall start our discussion by defining the background error covariance matrix at t_1. We make the assumption that the background error covariance matrix at t_1 is given by

$$B_1 = \hat{M} E_0^{-1} \hat{M}^T, \tag{5.1}$$

where $\hat{M}$ is the linear integral propagator for the interval t_0 to t_1, and E_0^{-1} is a normalising matrix. Assuming B_1 takes this form is equivalent to assuming that the background error covariance matrix evolves from a uniform, non-covariant, zero-mean distribution (with respect to the E_0 inner product) at t_0; Berliner et al. (1999). Whilst we have defined $\hat{M}$ to be simply the linear integral propagator, it is worth noting here that $\hat{M}$ could in theory incorporate additional periodic transformations to represent analysis cycles occurring between t_0 and t_1.

The second component required for the targeting method is a means of transforming the back-

ground error covariance matrix at t_1 into the analysis error covariance matrix due to the p^{th} possible deployment of observations. For this purpose we define the matrix G_p such that

$$A_1(G_p) = G_p B_1 G_p^T = G_p \hat{M} E_0^{-1} \hat{M}^T G_p^T. \tag{5.2}$$

The matrix G_p is some approximation to the gain matrix (response function) of the data assimilation system. The properties of G_p will be discussed in Section 5.3, but it is worth noting here that in this definition of A_1 we have pre-emptively assumed that the effects of observation errors on the analysis errors are small enough to be neglected.

Finally we require a means of evolving the analysis error covariance matrix at t_1 to the covariance matrix of forecast errors in the verification region defined by the local projection operator T_2, at t_2. To produce this evolved covariance matrix we employ the matrix $T_2 M$, where M is the linear integral propagator for the interval t_1 to t_2. The locally projected forecast error covariances are then given by

$$T_2 B_2(G_p) T_2 = T_2 M G_p B_1 G_p^T M^T T_2 = T_2 M G_p \hat{M} E_0^{-1} \hat{M}^T G_p^T M^T T_2, \tag{5.3}$$

where

$$B_2(G_p) = M A_1(G_p) M^T \tag{5.4}$$

is the predicted forecast error covariance matrices at t_2 for the p^{th} deployment of observations.

Having defined the expected background errors due to the p^{th} deployment of observations, the next step is to define the metric by which the favourability of the deployment may be determined. For this purpose we use the A-optimal measure of the expected forecast error variance at t_2 as

measured with the norm induced by the E_2 inner product. Following Berliner et al. (1999) we note that the expected forecast error variance at t_2 is equal to the trace (sum of the elements on the main diagonal) of the forecast error covariance normalised by $E_2^{\frac{1}{2}}$. The expected reduction in forecast error variance due to the p^{th} possible deployment of observations at t_1 is then given by the reduction in the trace of the background error covariance matrix; i.e.

$$\mathcal{E}\left[\|T_2\boldsymbol{\epsilon}_2\|_{E_2}^2 - \|T_2\boldsymbol{\epsilon}_2(G_p)\|_{E_2}^2\right] = trace\{E^{\frac{1}{2}}T_2B_2(I)T_2E^{\frac{1}{2}}\} - trace\{E^{\frac{1}{2}}T_2B_2(G_p)T_2E^{\frac{1}{2}}\} \tag{5.5}$$

where $\boldsymbol{\epsilon}_2(G_p)$ and $\boldsymbol{\epsilon}_2$ denote the vector of forecast errors at t_2 obtained with the p^{th} possible deployment of observations and with no observations, respectively, and

$$B_2(I) = MB_1M^T \tag{5.6}$$

denotes the forecast error covariance matrix at t_2 when no observations are taken at t_1; i.e. if $G_p = I$.

Here we have written the background error variance as the expected E_2-norm-squared amplitude to facilitate comparison with the singular vector targeting criterion given in Equation (4.2) of Chapter 4. As we shall see later, if $t_0 = t_1$ (i.e. $\hat{M} = I$) and if a particularly simple choice of the form of G_p is made, Equation (5.5) reduces to Equation (4.2).

Equation (5.5) defines the basis of the targeting method, however due to the high dimension of the matrices involved, direct calculation of $\mathcal{E}\left[\|T_2\boldsymbol{\epsilon}_2\|_{E_2}^2 - \|T_2\boldsymbol{\epsilon}_2(G_p)\|_{E_2}^2\right]$ for a single G_p is computationally expensive. The computational expense of calculating $\mathcal{E}\left[\|T_2\boldsymbol{\epsilon}_2\|_{E_2}^2 - \|T_2\boldsymbol{\epsilon}_2(G_p)\|_{E_2}^2\right]$ for multiple G_p would be extreme. Evidently Equation (5.5) requires significant simplification before it may be used in practical targeting applications. In the next section we discuss the reduc-

tion of the dimension of the problem using singular vectors. In Section 5.3 we shall discuss the properties of the matrix G_p.

5.2 Using singular vectors to reduce the rank of the targeting problem

In the previous section we defined the basis of our A-optimal targeting method. The method requires several high dimensional matrix operations to be performed recursively for different observational deployments. Such recursive calculations incur a vast computational expense, therefore a means of reducing the 'size' of the problem is required. In this section we shall demonstrate how singular vectors may be used to approximate the dynamical evolution of the errors leading, to a large reduction in the computational cost.

We shall start by substituting into the definition of $E_2^{\frac{1}{2}} T_2 B_2(G_p) T_2 E_2^{\frac{1}{2}}$, the singular value decomposition

$$E_2^{\frac{1}{2}} T_2 M E_1^{-\frac{1}{2}} = U \Sigma V^T, \tag{5.7}$$

where U, V and Σ are matrices containing the left and right singular vectors and the singular values respectively. With this substitution $B_2(G_p)$ becomes

$$E_2^{\frac{1}{2}} T_2 B_2(G_p) T_2 E_2^{\frac{1}{2}} = U \Sigma V^T E_1^{\frac{1}{2}} A_1(G_p) E_1^{\frac{1}{2}} V \Sigma U^T \tag{5.8}$$

We are however not interested in computation of $E_2^{\frac{1}{2}} T_2 B_2(G_p) T_2 E_2^{\frac{1}{2}}$. We are only interested in calculation of the trace of $E_2^{\frac{1}{2}} T_2 B_2(G_p) T_2 E_2^{\frac{1}{2}}$. We can make use of the fact that the trace of a

matrix is invariant to similarity transformations (Golub and Van Loan (1983)) and write the trace of $E_2^{\frac{1}{2}} T_2 B_2(G_p) T_2 E_2^{\frac{1}{2}}$ as

$$trace\{E_2^{\frac{1}{2}} T_2 B_2(G_p) T_2 E_2^{\frac{1}{2}}\} = trace\{\Sigma V^T E_1^{\frac{1}{2}} A_1(G_p) E_1^{\frac{1}{2}} V \Sigma\}. \tag{5.9}$$

Here we have made use of the fact that since U is an orthogonal matrix (Golub and Van Loan (1983)), $U^{-1} = U^T$, and hence pre and post multiplication by U and U^T respectively is a similarity transformation. Writing the trace as the summation over the diagonal elements of $\Sigma V^T E_1^{\frac{1}{2}} A_1(G_p) E_1^{\frac{1}{2}} V \Sigma$ and using index notation for the matrix multiplications yields

$$\begin{aligned} trace\{E_2^{\frac{1}{2}} T_2 B_2(G_p) T_2 E_2^{\frac{1}{2}}\} &= \sum_{i=1}^{N_g} [\Sigma V^T E_1^{\frac{1}{2}} A_1(G_p) E_1^{\frac{1}{2}} V \Sigma]_{i,i} \\ &= \sum_{i=1}^{N_g} \sum_{j=1}^{N_g} \sum_{k=1}^{N_g} [\Sigma V^T]_{i,j} [E_1^{\frac{1}{2}} A_1(G_p) E_1^{\frac{1}{2}}]_{j,k} [V\Sigma]_{k,i} \end{aligned}, \tag{5.10}$$

where the notation $[A]_{j,k}$ denotes the j^{th} element of the k^{th} column of the matrix A. Noting that the i^{th} row (column) of ΣV^T ($V\Sigma$) is $\sigma_i \boldsymbol{v}_i^T$ ($\sigma_i \boldsymbol{v}_i$), we replace the summations over j and k with matrix vector multiplications yielding

$$trace\{E_2^{\frac{1}{2}} T_2 B_2(G_p) T_2 E_2^{\frac{1}{2}}\} = \sum_{i=1}^{r} \sigma_i^2 \boldsymbol{v}_i^T E_1^{\frac{1}{2}} A_1(G_p) E_1^{\frac{1}{2}} \boldsymbol{v}_i, \tag{5.11}$$

where $r = rank\{E_2^{\frac{1}{2}} T_2 M E_1^{-\frac{1}{2}}\}$

The next step is to simplify $A_1(G_p)$. We start by noting that components of $A_1(G_p)$ which lie in the null-space (Golub and Van Loan (1983)) of $T_2 E_2^{\frac{1}{2}} M$ make no contribution to the trace of $E_2^{\frac{1}{2}} T_2 B_2(G_p) T_2 E_2^{\frac{1}{2}}$. Essentially this means that in regions which lie far from, or are 'dynamically disconnected' from the region T_2 at t_1, can be removed from the search for the optimal observation locations. We define the local projection operator $\hat{T}_1$ to contain all the geographical locations

which are to be included in the search. $\hat{T}_1$ is defined such that

$$T_2 M G_p \hat{T}_1 \hat{M} = T_2 M G_p \hat{M}, \tag{5.12}$$

for all potential G_p and consequently the trace of $E_2^{\frac{1}{2}} T_2 B_2(G_p) T_2 E_2^{\frac{1}{2}}$ is unaffected by the presence of $\hat{T}_1$; i.e.

$$\begin{aligned} trace\{E_2^{\frac{1}{2}} T_2 B_2(G_p) T_2 E_2^{\frac{1}{2}}\} &= trace\{E_2^{\frac{1}{2}} T_2 M G_p \hat{M} E_0^{-1} \hat{M}^T G_p^T M^T T_2 M E_2^{\frac{1}{2}} T_2\} \\ &= trace\{E_2^{\frac{1}{2}} T_2 M G_p \hat{T}_1 \hat{M} E_0^{-1} \hat{M}^T \hat{T}_1 G_p^T M^T T_2 M E_2^{\frac{1}{2}} T_2\} \end{aligned} \tag{5.13}$$

With this in mind we define the singular value decomposition

$$E_1^{\frac{1}{2}} \hat{T}_1 \hat{M} E_0^{-\frac{1}{2}} = \sum_{j=1}^{\hat{r}} \hat{\sigma}_j \hat{\boldsymbol{u}}_j \hat{\boldsymbol{v}}_j^T, \tag{5.14}$$

where $\hat{r} = rank\{\hat{T}_1 E_1^{\frac{1}{2}} \hat{M} E_0^{-\frac{1}{2}}\}$.

Making use of the orthogonality of the right singular vectors we may write

$$E_1^{\frac{1}{2}} \hat{T}_2 \hat{M} E_0^{-1} \hat{M}^T \hat{T}_2 E_1^{\frac{1}{2}} = \sum_{j=1}^{\hat{r}} \sum_{k=1}^{\hat{r}} \hat{\sigma}_j \hat{\sigma}_k \hat{\boldsymbol{u}}_j \hat{\boldsymbol{v}}_j^T \hat{\boldsymbol{v}}_k \hat{\boldsymbol{u}}_k^T = \sum_{j=1}^{\hat{r}} \hat{\sigma}_j^2 \hat{\boldsymbol{u}}_j \hat{\boldsymbol{u}}_j^T. \tag{5.15}$$

Substituting the above into the trace of $E_2^{\frac{1}{2}} T_2 B_2(G_p) T_2 E_2^{\frac{1}{2}}$ yields the expression

$$trace\{E_2^{\frac{1}{2}} T_2 B_2(G_p) T_2 E_2^{\frac{1}{2}}\} = \sum_{i=1}^{r} \sum_{j=1}^{\hat{r}} \sigma_i^2 \hat{\sigma}_j^2 \boldsymbol{v}_i^T E_1^{\frac{1}{2}} G_p E_1^{-\frac{1}{2}} \hat{\boldsymbol{u}}_j \hat{\boldsymbol{u}}_j^T E_1^{-\frac{1}{2}} G_p^T E_1^{\frac{1}{2}} \boldsymbol{v}_i. \tag{5.16}$$

Noting that this expression is the product of two identical inner products, we may write the trace

of $E_2^{\frac{1}{2}} T_2 B_2(G_p) T_2 E_2^{\frac{1}{2}}$ as

$$trace\{E_2^{\frac{1}{2}} T_2 B_2(G_p) T_2 E_2^{\frac{1}{2}}\} = \sum_{i=1}^{r} \sum_{j=1}^{\hat{r}} \sigma_i^2 \hat{\sigma}_j^2 (\boldsymbol{v}_i^T E_1^{\frac{1}{2}} G_p E_1^{-\frac{1}{2}} \hat{\boldsymbol{u}}_j)^2. \tag{5.17}$$

Finally, using Equation (5.17), we may write $\mathcal{E}\left[\|T_2\boldsymbol{\epsilon}_2\|_{E_2}^2 - \|T_2\boldsymbol{\epsilon}_2(G_p)\|_{E_2}^2\right]$ in terms of the singular vectors as

$$\mathcal{E}\left[\|T_2\boldsymbol{\epsilon}_2\|_{E_2}^2 - \|T_2\boldsymbol{\epsilon}_2(G_p)\|_{E_2}^2\right] = \sum_{i=1}^{r} \sum_{j=1}^{\hat{r}} \sigma_i^2 \hat{\sigma}_j^2 \left[(\boldsymbol{v}_i^T \hat{\boldsymbol{u}}_j)^2 - (\boldsymbol{v}_i^T E_1^{\frac{1}{2}} G_p E_1^{-\frac{1}{2}} \hat{\boldsymbol{u}}_j)^2\right]. \tag{5.18}$$

The $(\boldsymbol{v}_i^T \hat{\boldsymbol{u}}_j)^2$ term comes about by noting that in the absence of observations $G_p = I$. By rewriting in terms of the singular vectors we have reduced the computation expense to that of $r \times \hat{r}$ inner products for each possible deployment of observations. However the computational expense will be reduced even further if Equation (5.18) is computed only approximately using fewer than r and $\hat{r}$ singular vectors. By computing Equation (5.18) with fewer singular vectors we also reduce significantly the initial expense of computing the singular vectors.

We can interpret Equation (5.18) by considering the meanings of the two terms in the square bracket. The first term, $(\boldsymbol{v}_i^T \hat{\boldsymbol{u}}_j)^2$, is a measure of the projection of the errors in the background field onto the 'growing phase-space' of the forecast error. It is by reducing this projection that the assimilation of observations is expected to reduce the forecast error. The second term, $(\boldsymbol{v}_i^T E_1^{\frac{1}{2}} G_p E_1^{-\frac{1}{2}} \hat{\boldsymbol{u}}_j)^2$ is a measure of the projection of the analysis errors associated with the p^{th} deployment of observations onto the growing phase-space of the forecast trajectory. If the first term is larger than the second, then the Equation (5.18) is positive and p^{th} deployment of observations is expected to be beneficial to the forecast accuracy. Conversely, if the second term is larger, then Equation (5.18) is negative and the additional observations are likely to be detrimental to the

forecast accuracy. The idea that adding additional observational data will be detrimental to the forecast may seem a little counterintuitive, but if one considers that reducing the errors in a *local* region acts as a rotation of the *global* error structure in phase-space rather than a simple global reduction in error amplitude, it makes more sense. As a crude example one could consider simply correcting the background error to the observation without any smoothing. Whilst this simple correction procedure may reduce the initial condition error amplitude, it is likely create a 'jagged' error structure which may lead to greater error amplification than occurs in the uncorrected field. It is the belief that the data assimilation process 'rotates' the initial condition errors towards smaller scales that in part motivates the type of singular vector based observation targeting described in the previous chapter; Palmer et al. (1998). For our purposes, it is partly the possibility of observations causing 'unfavourable' phase-space rotation of the errors that motivates both the desire for G_p to be an approximation to the gain matrix of the operational data assimilation system, in the evaluation of Equation (5.18). We shall show that this increase in forecast error would not be predictable if the targeting method assumed the existence of an operational Kalman filter, as is the case in methods such as the ensemble transform Kalman filter method. The desired properties of G_p will be discussed more fully in the next section.

5.3 Approximation of the data assimilation response

In the previous sections of the current chapter we proposed a methodology for observation targeting, and demonstrated how the computational expense of the method may be reduced. One component of the methodology is the matrix G_p, which is a transformation of the estimated background error covariance at t_1 to the predicted analysis error covariance matrix at t_1 due to the p^{th}

possible deployment of observations. We have so far said very little about the desired properties of G_p other than the fact it should approximate the response of the operational data assimilation system. Bergot (2001) find that the efficiency of targeted observations depends on the assimilation scheme, noting several cases where the assimilation of targeted observations by the 3D-Var and 4D-Var schemes lead to significant differences in the change in accuracy of the subsequent forecast. Bergot (2001) find that in some cases assimilation of observations with 4D-Var leads to forecast improvement, whereas if 3D-Var is used, the assimilation of the same observations degrades the accuracy of the subsequent forecast. The targeting methodologies of Bishop and Toth (1999) and Hamill and Snyder (2002a) define the target region which would be beneficial to forecast systems utilising ensemble Kalman filter based assimilation systems. At present meteorological centres typically employ 3D-Var and 4D-Var assimilation systems. The underlying assumption of the existence of a Kalman filter may lead to miscalculations in the expected forecast correction obtained from a given deployment of observations. Such mis-calculations have been noted by Majumdar et al. (2001) who find the benefits of targeted observations are overestimated by the Ensemble Transform Kalman Filter.

How G_p should be defined so that it is consistent with the operational data assimilation scheme is a complex question. This question is further complicated by the requirement that the generation of multiple G_p and the subsequent calculation of the inner products in Equation (5.18) be computationally inexpensive. We shall not attempt to tackle this question in full within this thesis. We shall instead demonstrate an inexpensive G_p for a simple 3D-Var assimilation system. But prior to this we shall discuss some of the potential similarities and differences between the effects of different assimilation schemes. We shall discuss first the properties of the 3D-Var and 4D-Var assimilation schemes that are used operationally in weather forecasting centres. We shall

also discuss the Kalman Filter. Although the Kalman Filter is not used operationally, Kalman Filter theory is of particular importance to the targeting methods such as the Ensemble Transform Kalman Filter.

In the 3D-Var assimilation scheme all observations within a pre-specified finite time period (assimilation window) are assumed to have been made at a single point in time. For example, if we generate an analysis of the atmospheric state at the analysis time t_a, in 3D-Var we treat all observations made within a few hours of t_a as if they were made at t_a. The cost function

$$\mathscr{J}(\boldsymbol{\chi}) = \frac{1}{2}\left(\boldsymbol{\chi}^b - \boldsymbol{\chi}^a\right)^T B^{-1}\left(\boldsymbol{\chi}^b - \boldsymbol{\chi}^a\right) + \frac{1}{2}\left(\boldsymbol{y} - H\boldsymbol{\chi}\right)^T R^{-1}\left(\boldsymbol{y} - H\boldsymbol{\chi}\right), \tag{5.19}$$

which was introduced in Chapter 1[1] is then minimised (usually approximately) using an iterative algorithm. In 3D-Var analysis schemes, the background error covariances are usually modelled as separable in the horizontal and vertical directions, with the horizontal correlations assumed to be homogeneous. The correlations between the errors in different variables and different horizontal wavenumbers are often neglected. Due to the simplicity of the assumed background error statistics, the 3D-Var assimilation scheme is effectively blind to the day to day variations in the accuracy of the background field. In particular due to the homogeneity of the modelled background error covariance 3D-Var 'spreads' observational information evenly in all directions regardless of any asymmetries in the correlations in the background error statistics.

The 4D-Var analysis scheme differs from the 3D-Var in that a linear integral propagator is incorporated into the definition of the forward model so that H is replaced by $H\tilde{M}(t_a, t_o)$ where $\tilde{M}(t_a, t_o)$ is the linear integral propagator from the analysis time, t_a, to the observation time, t_o. In the 4D-Var scheme the background error covariance matrix, B, is usually contains simi-

[1]For the definition in this chapter we have assumed that the observation operator/forward model is linear

lar approximations to those used in 3D-Var schemes. In 4D-Var, however, the inclusion of the linear integral propagator means that observational information is spread in a manner more consistent with the current atmospheric flow. In particular, due to the iterative solution methods used to approximately minimise the cost function, 4D-Var preferentially adjusts the background field along the leading singular singular vectors of the matrix $\tilde{M}(t_a, t_o)$. Essentially this means that the change in the background field induced by observations is expected to effect the structures which amplify the most over the time interval t_a to t_o. This picture is not so clear-cut, however, since the degree to which the current dynamics affect the spreading of observational information is dependent on the time interval t_a to t_o. If the observations are made close to the analysis time then the influence of the dynamics will be much lower than if the observations are made far from the analysis time. For the former case, that of observations being made close to t_a, the differences between the response of a 4D-Var and a 3D-Var assimilation scheme with identical B matrices may be small.

In contrast to the 3D-Var and 4D-Var assimilation schemes, the Kalman Filter scheme does not make assumptions of homogeneity of the B matrix. In the Kalman Filter scheme the B matrix is continually evolved using the linearised dynamical model. Due to this continuous evolution of the error statistics the Kalman Filter assimilation scheme takes account of large scale inhomogeneous statistical correlations in the background errors which accumulate over time intervals longer than the analysis windows used in 3D-Var and 4D-Var. For example the Kalman Filter may spread information along dynamical features such as fronts and cyclones; Majumdar et al. (2001). 3D-Var and 4D-Var are only aware of these long range correlations in so much as they have been incorporated into the homogeneous model background error covariance matrix. Whilst the Kalman Filter assimilation scheme is at present too expensive to be used in operational weather forecasting it is

still relevant to targeted observations. This relevance is due to the fact that targeting methods such as the Ensemble Transform Kalman Filter and the ensemble method of Hamill and Snyder (2002a) predict the forecast correction that would be obtained if the observations were assimilated using Kalman Filter based data assimilation schemes. Essentially, these Kalman filter based methods have the underlying assumption that the data assimilation scheme is 'aware' of long range dynamical correlations specific to the current flow regime, when in actual fact the operational data assimilation scheme may well be unable to account of such information. It is important to note here that the fact the data assimilation scheme does not utilise information about long range dynamical error correlations does not mean such correlations don't exist, merely that they do not effect the 'spreading' of observational information during the assimilation process. A targeting method that does not make use of Kalman Filter theory may therefore give a more accurate picture of the response to the placement of observations in a given location. A targeting method that assumes a 3D-Var or 4D-Var assimilation system may give a more accurate prediction of the optimal observation locations. Consistency with the 3D-Var assimilation scheme may be more easily achievable than consistency with the more complex 4D-Var scheme, but as has been noted when the observation time is close to the analysis time these two assimilation systems may be relatively similar in their response. In the remainder of this section we shall define a G_p which is both consistent with a simple 3D-Var type assimilation scheme and computationally inexpensive.

We shall commence our definition of G_p by defining the analysis, χ^a, as the zero point of the Jacobian (first derivative with respect to $\boldsymbol{\chi}$) of the cost function Equation (5.19). Taking the first derivative and equating to zero yields

$$\frac{\partial}{\partial \boldsymbol{\chi}} \mathscr{J}(\boldsymbol{\chi}_a) = \frac{1}{2} B^{-1} \left(\boldsymbol{\chi}^b - \boldsymbol{\chi}^a \right) + \frac{1}{2} H^T R^{-1} (\boldsymbol{y} - H\boldsymbol{\chi}_a) \equiv 0. \tag{5.20}$$

We define the analysis, observation and background errors to be the vector deviations $\boldsymbol{\epsilon}^a = \boldsymbol{\chi}^t - \boldsymbol{\chi}^a$, $\boldsymbol{\epsilon}^o = H\boldsymbol{\chi}^t - \boldsymbol{y}$ and $\boldsymbol{\epsilon}^b = \boldsymbol{\chi}^t - \boldsymbol{\chi}^b$ from the an imaginary perfect analysis (or 'truth') $\boldsymbol{\chi}^t$. Substituting these error definitions into Equation (5.20) and rearranging, we can write the analysis errors

$$\boldsymbol{\epsilon}^a = (B^{-1} + H^T R^{-1} H)^{-1}(B^{-1}\boldsymbol{\epsilon}^b + H^T R^{-1}\boldsymbol{\epsilon}^o). \tag{5.21}$$

From the above equation, we can see that the analysis errors are the sum of matrix transformations of the background and observation errors. If the observations are to be taken in regions with large background errors, it is reasonable to assume that the amplitude of the background errors will be larger than the observation errors, so we may simplify Equation (5.21) by letting $\boldsymbol{\epsilon}^o = 0$. The effect of observation errors on the target selection could be included by adding an additional term to the target selection Equation (5.18), however, for concision, discussion of this term will not be included in this thesis. With this small observation error approximation, the analysis errors are simply defined as a matrix transformation of the background errors. We can define the transformation associated with the p^{th} deployment of observations as

$$G_p = (B^{-1} + H_p^T R_p^{-1} H_p)^{-1} B^{-1}, \tag{5.22}$$

where H_p and R_p are the observation operator and observation error covariance matrix associated with the p^{th} deployment of observations. It is worth reminding the reader that the matrices R_p^{-1} and B^{-1} are the error covariances assumed by the data assimilation system and are not necessarily the same as the 'actual' error covariance. Using the *Sherman-Woodbury-Morrison formula*

(Golub and Van Loan (1983)) we may rewrite G_p as

$$\begin{aligned} G_p &= (B - BH_p^T R_p^{-\frac{1}{2}}(I + R_p^{-\frac{1}{2}} H_p B H_p^T R_p^{-\frac{1}{2}})^{-1} R_p^{-\frac{1}{2}} H_p B) B^{-1} \\ &= I - BH_p^T R_p^{-\frac{1}{2}}(I + R_p^{-\frac{1}{2}} H_p B H_p^T R_p^{-\frac{1}{2}})^{-1} R_p^{-\frac{1}{2}} H_p \\ &= I - BH_p^T (R + H_p B H_p^T)^{-1} H_p \\ &= I - G'_p, \end{aligned} \tag{5.23}$$

where

$$G'_p = BH_p^T (R + H_p B H_p^T)^{-1} H_p. \tag{5.24}$$

Substituting the above definition of G_p into the targeting criteria given in Equation (5.18) and rearranging, yields

$$\begin{aligned} &\mathcal{E}\left[\|T_2 \boldsymbol{\epsilon}_2\|_{E_2}^2 - \|T_2 \boldsymbol{\epsilon}_2(G_p)\|_{E_2}^2\right] \simeq \\ &\qquad \simeq \sum_{i=1}^{N_v \leq r} \sum_{j=1}^{N_{\hat{u}} \leq \hat{r}} \sigma_i^2 \hat{\sigma}_j^2 \left[2(\boldsymbol{v}_i^T \hat{\boldsymbol{u}}_j)(\boldsymbol{v}_i^T E_1^{\frac{1}{2}} G'_p E_1^{-\frac{1}{2}} \hat{\boldsymbol{u}}_j) - (\boldsymbol{v}_i^T E_1^{\frac{1}{2}} G'_p E_1^{-\frac{1}{2}} \hat{\boldsymbol{u}}_j)^2\right]. \end{aligned} \tag{5.25}$$

If $N_v = r$ and $N_u = \hat{r}$, then this is exactly equal to Equation (5.18), but if fewer than $N_v = r$ and $N_u = \hat{r}$ singular vectors are used then the two equations are only approximately equal. After the initial outlay of the singular vector computation, the computation of the target region requires a *single* computation of the $N_v \times N_{\hat{u}}$ inner products, $\boldsymbol{v}_i^T \hat{\boldsymbol{u}}_j$, plus the computation of $N_v \times N_{\hat{u}}$ inner products, $\boldsymbol{v}_i^T E^{-\frac{1}{2}} G'_p E^{\frac{1}{2}} \hat{\boldsymbol{u}}_j$, for every observational deployment to be tested. The expense of the inner products $\boldsymbol{v}_i^T E^{-\frac{1}{2}} G'_p E^{\frac{1}{2}} \hat{\boldsymbol{u}}_j$ may be significantly reduced by exploiting the structure of the matrix products which define G'_p. For example the matrices BH_p^T and $H_p^T H_p$ have the same number of columns as there are observations. The number of non-zero elements in each column will depend on the manner in which the observational information is spread by the data assimila-

tion system and the relationship between the observations and the control vector. In the simplest case, if the control and observed variable are identical and the background and observation error covariance matrices are diagonal, then G'_p have only one non-zero element per observation. By contrast, if the background and observation error covariance matrices are dense and the control variable has a complicated relationship with the observed variable then G'_p will have a large number of non-zero elements. The complexity of G'_p determines the computational expense incurred when testing each possible observational deployment. The simpler G'_p the greater number of observational deployments that can be tested in a given time period. In the next Section we shall define a simple data assimilation system to be used in the Eady model and the corresponding G'_p.

5.4 Implementation of the targeting method in the Eady model

5.4.1 A simple definition of G_p

In this section we shall define a simple data assimilation system for the Eady model. We shall then show the form of the corresponding G_p based on the assumption that the observation errors are small. We shall start by defining the control vector for the data assimilation system. We shall define the control vector to be

$$\boldsymbol{\chi} = \tilde{\boldsymbol{\psi}} = F\boldsymbol{\psi}, \tag{5.26}$$

where F is the reduced rank Fourier transform introduced in the Chapter 3, and $\tilde{\boldsymbol{\psi}}$ is the spectral-space representation of the streamfunction field. Here is should be stressed that defining the control vector in this way restricts the analysis increments to only contain the first ten zonal wavenumbers. We shall further assume that all observations are of streamfunction and collocate

with model grid[2]. The observation operator is then defined as the inverse Fourier transformation, $F^T \in \mathbb{R}^{N_g \times 2N_k}$, from the spectral control-space to the grid point space followed by a projection, $Q \in \mathbb{R}^{N_o \times N_g}$ onto the grid points at which observations are located; i.e.

$$H = QF^T. \tag{5.27}$$

Following the conventions of 3D-Var we shall define the data assimilation system's background error covariance matrix such that the zonal and vertical correlations are separable, the zonal correlations are homogeneous and isotropic and there are no correlations between different zonal wavenumbers. With these assumptions, the background error covariance matrix consists of an $N_z \times N_z$ block for each zonal wave component. For the time being we shall not discuss the properties of the vertical correlations. Finally we shall make the assumption that the errors in different observations are not correlated. Without correlations between observations the observation error covariance matrix $R \in \mathbb{R}^{N_o \times N_o}$ is diagonal. From Equation (5.21) the analysis errors for the Eady model data assimilation system are defined as

$$\boldsymbol{\epsilon}^a = (B^{-1} + FQ^T R^{-1} QF^T)^{-1} B^{-1} \boldsymbol{\epsilon}^b + FQ^T R^{-1} \boldsymbol{\epsilon}^o, \tag{5.28}$$

and it follows that G'_p may be written

$$G'_p = BFQ_p^T (R_p + Q_p F^T BFQ_p^T)^{-1} Q_p F^T. \tag{5.29}$$

[2]N.B. the reader is reminded that since F is not full rank, the model grid is of higher dimension than the Fourier space associated with the first ten zonal wavenumbers

5.4.2 Simplification of G_p

Once the singular vectors have been computed, the only significant computational expense comes from the inversion of the bracketed term $(R_p + Q_p F^T B F Q_p^T)$ for multiple possible deployments of observational deployments. Making use of the following: the observation errors vary with height only; the background error covariance matrix is zonally homogeneous and isotropic; and by neglecting the vertical background error correlations within the bracketed term, we may write G_p'

$$G_p' \simeq B F Q_p^T D(z) Q_p F^T, \tag{5.30}$$

where $D(z)$ is a diagonal matrix whose elements depend on the height of the observation. Proof of Equation (5.30) is given in Appendix C. Since, both $(Q F^T B F Q^T)_{i,i}$ and depend on height and not the zonal location, the diagonal elements of D depend only on the height of the corresponding observation. The extent to which this approximation is valid depends on how close to being diagonal B actually is. Interestingly in 'typical' 3/4d-Var assimilation schemes the vertical correlations in B are strongest at low wavenumbers and on the upper and lower boundaries. By contrast, as we shall see, the low wavenumbers and the upper and lower boundaries play only a minor role in the selection of the target region using the method outlined above. Essentially this means that, for typical assimilation schemes, the approximation of B by its diagonal in the bracketed term is likely to be most inaccurate in the regions of phase-space which are of least importance for the target selection. That is not to say, however, that this in general a good approximation, merely that the greatest inaccuracy occurs in the least significant regions.

At an even greater level of approximation, if B and R are taken as uniform diagonal matrices (i.e.

constant multiples of the identity matrix) throughout G'_p then we may write

$$G'_p \simeq cH_p^T H_p = cFQ_p^T Q_p F^T = cT_p \tag{5.31}$$

where c is a constant and T_p is a local projection operator that sets the model state to zero everywhere except at the observation locations. For this particularly simple definition of G'_p, when $t_1 - t_0 = 0$, the targeting criteria given in Equation (5.25) reduces to the same mathematical formulation of the targeting criteria given in Equation (4.2). However when $t_1 - t_0$ is not equal to zero then Equation (5.25) and Equation (4.2) are not of the same mathematical form. For this simple choice of G_p, the targeting criteria given in Equation (5.25) can be interpreted as an extension to Equation (4.2) in which the effect of the evolution of the errors prior to the observation time is taken into account. In the next section we shall demonstrate a simple implementation of Equation (5.25) in which $G'_p = cT_p$ and discuss the relationship to the results shown in the previous chapter.

5.4.3 Computing the singular vectors

In this section we shall describe the implementation of the targeting method in the Eady model. Firstly we need to define the singular vectors that will be used to compute the target region. As in the previous chapter we shall define the singular value decomposition over the forecast period from t_1 to t_2 thus,

$$P_2 L F^T = \sum_{i=1} \sigma_i \boldsymbol{u}_i \boldsymbol{v}_i. \tag{5.32}$$

For this first set of singular vectors the local projection is a projection onto the verification region. For all calculations in this section the verification region is selected to be the same as that used in the previous chapter.

The second set of singular vectors are defined, over the interval t_0 to t_1 as

$$P_1 \hat{L} F^T = \sum_{i=1} \hat{\sigma}_i \hat{\boldsymbol{u}}_i \hat{\boldsymbol{v}}_i, \tag{5.33}$$

where $\hat{L}$ is the integral dynamical propagator for the interval t_0 to t_1, and P_1 is a local projection. The local projection P_1 is defined to include all grid locations in which the 'sensitivity' as identified by using the singular vector method of Buizza and Montani (1999) has non-negligible amplitude.

5.4.4 Examination and dynamical interpretation of the optimal observation location

In this section we consider the dynamical effects which determine the target regions calculated in the Eady model using the new targeting method. We shall consider how the target regions vary as the time interval t_0 to t_1 is increased from zero. Since the target calculation for $t_1 - t_0 = 0$ yields the same results as the targeting method of Buizza and Montani (1999), we may use the results to compare the targets calculated with the new method to those which would be computed using that of Buizza and Montani (1999). The main aim of this section is to demonstrate how the use of an additional set of singular vectors to approximate the statistics of initial condition errors affects the location of the target region, and how this relates to the dynamics of the Eady model. We shall consider two observing scenarios. These two scenarios are that a single vertical column

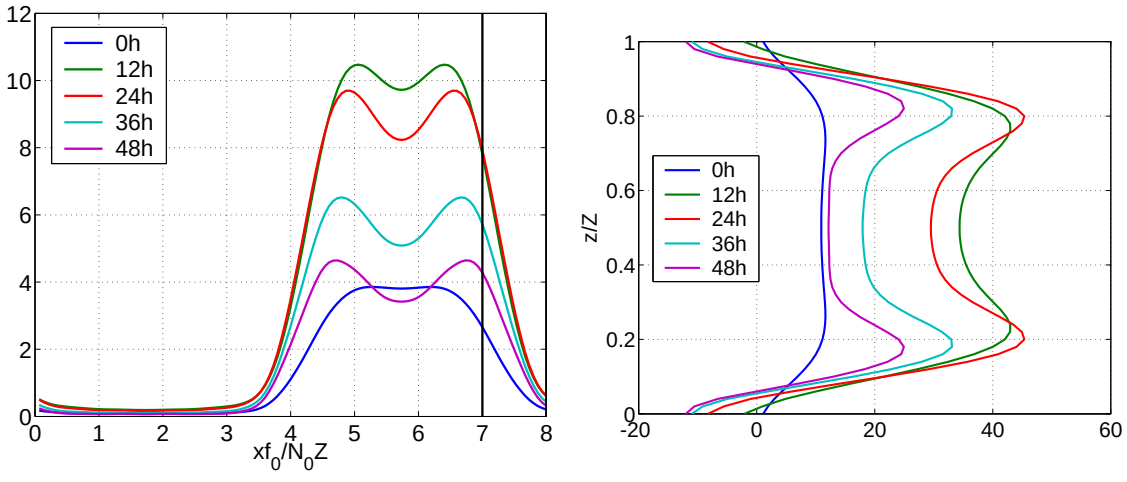

A B

Figure 5.1 *Predicted reduction in forecast error variance for a $24h$ forecast as a function of (A) zonal location, (B) height, for different values of $t_1 - t_0$.*

is observed and that single vertical level is observed.

Figures 5.1A and 5.1B show the targets calculated for a $24h$ forecast. Figure 5.1A shows the variation in the predicted reduction of forecast error variance obtained by observing in a single vertical column, with the zonal location of the column. Figure 5.1B shows the same but for a single vertical level. The different coloured lines refer to the different values of $t_1 - t_0$. For $t_1 - t_0 = 0$ (blue line) the results are proportional to those that would be obtained using the targeting method discussed in Chapter 4.

Two things are noticeable in Figure 5.1. Firstly, as $t_1 - t_0$ increases, two peaks occur in both Figures 5.1A and 5.1B. Secondly, as the time interval $t_1 - t_0$ is increased, the expected correction in forecast error variance first increases, then decreases.

The fact that, as $t_1 - t_0$ increases, two peaks occur in both Figures 5.1A and 5.1B is consistent with the transition from the 'untilting/unshielding regime' to the 'modal unmasking regime' discussed

in the previous chapter. For values of $t_1 - t_0$ of order one to two days it may be inferred that the effect of dynamical evolution of the errors is to push the initial condition errors further into the modal unmasking regime. One can infer from this, that as was the case in the previous chapter, the two peaks are associated with the smaller zonal scales close to the upper and lower boundary steering levels, and that the area between the peaks is associated with the untilting of smaller scales and the modal unmasking of the larger scales.

For the $12h$ forecast the dynamical effect of evolved initial condition errors is greater, than for the $24h$ forecast. However this effect only leads to a double peak when observing for observing different vertical levels; i.e. equivalent to Figure 5.1B, not shown. When observing a single column, the location of the peak does not vary significantly. To understand this lack of variation in the location of the peak for the $12h$ forecast, one can consider that the tilt of the sensitive region (see Figure 4.7A) is small, and consequently the regions associated with modal unmasking and those associated with untilting/unshielding are in roughly the same zonal location. The result of the coincidence of the regions associated with different growth mechanisms is that transition from the untilting/unshielding regime to the modal unmasking technique does not significantly effect the zonal location of the target region. For longer forecasts (e.g. $48h$), since the transition from the unshielding to modal masking regime has largely occurred, the effect of changing $t_1 - t_0$ on the location of the peaks is small. To see this explicitly, Figure 5.2B shows the variation in the predicted reduction of forecast error variance obtained by observing in a single vertical column, with the zonal location of the column. In Figure 5.2B one can see that there is a small increase in the distance between the peaks as $t_1 - t_0$ is increased. This lack of zonal variation in the location of the optimal observation location, for $12h$ and $48h$ forecasts indicates that there is a 'window' of forecasts durations, somewhere around $24h$, during which the zonal location of the target region

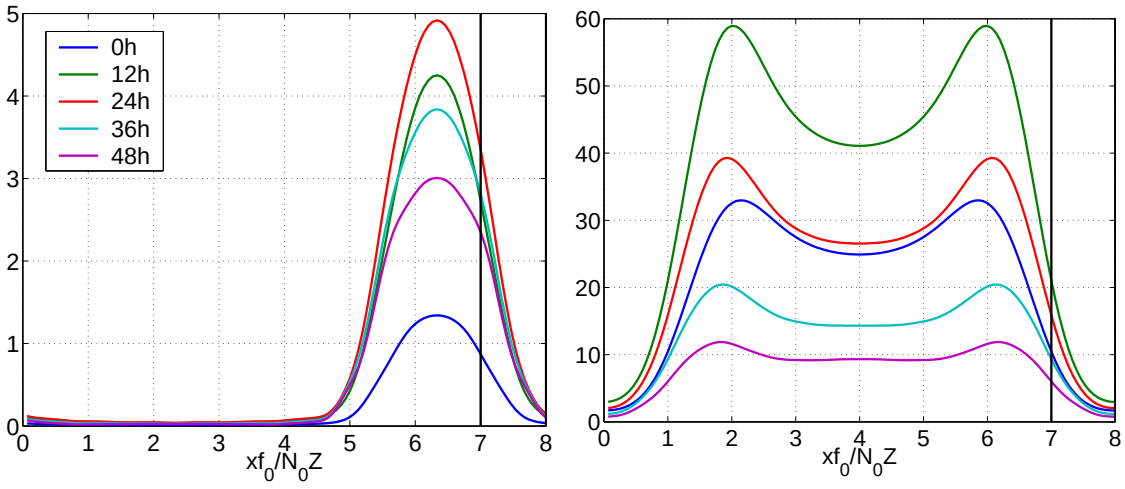

A B

Figure 5.2 *Predicted reduction in forecast error variance as a function of height for (A) a* $12h$ *forecast, (B) a* $48h$ *forecast, for different values of* $t_1 - t_0$.

is sensitive to short term dynamically evolved perturbations. However this statement must be qualified by the fact that the Eady model background state lacks the inhomogeneities present in the dynamics of models linearised about time evolving forecasts trajectories. These inhomogeneities may well lead to greater spatial variations in the optimal observation location with differing $t_1 - t_0$. Results from other authors [e.g. Snyder et al. (2003), Hamill and Snyder (2002b)] suggest that the effects of inhomogeneities in the background state can have a significant impact on the structure of linearly evolving covariances, over short time periods. Further investigation into the effect of such spatial inhomogeneities on this simplified dynamical picture of targeting is required.

The second thing that is noticeable in Figures 5.1A and 5.1B is that, as the time interval $t_1 - t_0$ is increased, the expected correction in forecast error variance first increases, then decreases. This behaviour is also seen in Figures 5.2A and 5.2B. Here the reader is reminded that the target is normalised by the trace of the predicted back ground error covariance matrix at t_1, so that the spatially averaged initial error variance is the same for each value of $t_1 - t_0$. The implication of

this increasing then decreasing expected reduction in error variance is that targeted observations will be most effective if they correct errors that are dynamically evolved structures, but correcting errors which are 'too dynamically evolved' will have lesser impact. The implication is that there is a value of $t_1 - t_0$ for which the impact of observations will be greatest. This value is likely to vary with forecast length, so in order to make more general comments we have to consider different forecast lengths. For this purpose, the dashed line of Figure 5.3 shows integral under the curve (y-axis) of Figure 5.1A as a function of $t_1 - t_0$ (x-axis). The solid, dotted and dot-dashed lines show the equivalent for $12h$ $36h$ and $48h$ forecasts respectively. Interestingly for all forecast integrations, this increasing and decreasing effectiveness of observations with increasing $t_1 - t_0$ is observed. For longer forecasts the peak effectiveness occurs at smaller values of $t_1 - t_0$, but for all forecast lengths shown the peak occurs at a value of $t_1 - t_0$ greater than zero. Conversely, for large $t_1 - t_0$ the effect of observations is smaller than for small $t_1 - t_0$, implying that correction of the long term evolved components of the forecast error may have lesser impact, than correcting error components which are closer to random. However we must stress that this result comes about because we have normalised the covariance at t_1. If we had normalised the error statistics at t_0, then the average error variance at t_1 would be larger for larger $t_1 - t_0$, and the predicted effectiveness of observations would increase with increased $t_1 - t_0$.

5.5 Summary

In this chapter we have introduced a new singular vector targeting method and examined targets produced using this new method using the Eady model singular vectors. This targeting method gives a prediction of the reduction in forecast error variance that would be obtained from a given

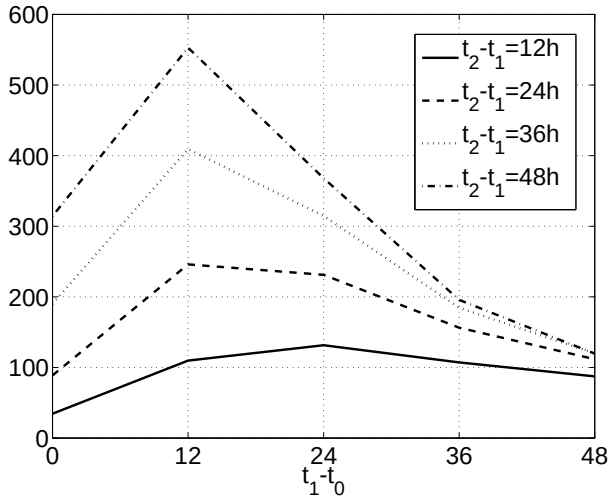

Figure 5.3 *The variation of the predicted reduction in forecast error variance obtained by observing every location, as a function of the value of* $t_1 - t_0$*. Each line corresponds to a different forecast length* $t_2 - t_1$*. For ease of viewing the values for the* $24h$*,* $36h$ *and* $48h$ *forecasts have been rescaled by factors* $1/2$*,* $1/4$*, and* $1/8$ *respectively.*

deployment of observations. The essential differences between this new method and previous methods are that, it uses singular vectors to produce a dynamically determined estimate of the initial condition errors, and that it utilises a linear transformation that can be made consistent with the operational data assimilation system to approximate the effect of observations on the initial condition errors.

In a simplified setting, the new targeting method is seen to coincide with the singular vector targeting of Buizza and Montani (1999). In this sense the new method can be interpreted as an extension to 'traditional' singular vector targeting. In this chapter we examined the effect of including dynamically evolved initial condition error estimates into the singular vector targeting method. The effect of including these evolved initial condition errors can be interpreted dynamically as moving the error evolution further into the modal unmasking regime. In a similar fashion to increasing

the forecast length in traditional singular vector targeting (see Chapter 4), increasing the length of the dynamical evolution of the initial condition errors, leads to the appearance of double peaks in the zonal and vertical sensitivity distribution. Furthermore it is found that the effectiveness of observations is increased if they correct errors that have evolved over a short time period. If this time period is increased or reduced, then the effectiveness of observations is reduced.

CHAPTER 6

Conclusions

This thesis is a contribution to the subjects of mid-latitude dynamics and targeted observations. For the first time the full spectrum of singular vectors of the Eady model are considered. The importance and implications of the unshielding and modal unmasking mechanisms, to the computed singular vectors are discussed. The computed singular vectors are used to analyse the singular vector targeting function commonly used in observation targeting, in a vertical cross-section. Through comparison of this vertical cross-section to the dynamics of singular vectors, inferences about the scale and qualitative behaviour of the perturbations to which particular regions are 'sensitive' are made. In the final section of the thesis, a new targeting method is introduced. This new targeting method utilises a set of evolved singular vectors to approximate the background errors within the region identified by a set of targeted singular vectors as dynamically connected to the verification region. The two sets of singular vectors can then be used as a computationally inexpensive means of predicting the reduction of forecast error variance that will be obtained from a given deployment of observations. In this final chapter we shall summarise the main results and conclusions of the work in the thesis, as well as motivating future work which may follow from that contained within the thesis.

In Chapter 3 we examined the properties of the full spectrum of singular vectors in the Eady model. The results and conclusions of this chapter can be summarised as follows. Roughly speaking we can partition the dynamics of the Eady singular vectors into two regimes. These two

regimes are the untilting regime and the modal unmasking regime. For short integration lengths it is found that untilting of potential vorticity is the dominant mechanism for singular vector growth. As the integration length increases then modal unmasking increases in importance, eventually becoming the dominant growth mechanism. Whilst the importance of both these mechanisms to singular vector growth has already been established by other authors, what has not been established is the implications for these mechanisms for singular vectors other than the first, and the significance of zonal wavenumber in setting the time-scale for the transition between the two regimes.

For the untilting regime, it is found that the requirement for orthogonality between untilting structures means that at higher zonal wavenumbers the second, third etc singular vectors will have an initial tilt closer to that of the first. This similarity of tilt means that the second, third etc short wavelength singular vectors will have singular values closer to that of the first singular vector, than would the equivalent longer wavelength singular vectors. Furthermore, it is found that for short integrations the singular values at smaller zonal scales are closer to that suggested by the untilting mechanism, whereas at longer scales they are significantly smaller. This discrepancy is attributed to the fact that at the smaller scales the normal modes are shallower so the interaction between the potential vorticity dynamics and that of the normal modes is lower than in the larger scales, allowing for the untilting of potential vorticity to occur in the smaller scales more freely at smaller scales. Taking into account both these scale selective effects, it may therefore be said that, for the untilting regime, the smaller scales dominate the singular vector spectrum because their maximum growth is larger, and because there are a larger number of singular vectors which achieve large amplification.

It is found that the modal masking regime which is characterised by concentrations of singular

vector amplitude near the steering level allows for amplification which can exceed the maximum amplification possible via untilting. The transition from the untilting to the modal masking regime is shown to occur more rapidly at the smaller zonal scales than the larger zonal scales. The time-scale for the transition is found that to depend approximately on the relative phase speeds of the normal modes and the potential vorticity in the region in which there is a strong interaction between potential vorticity and the normal modes. For short integrations this phase difference is too small to lead to a significant change in the phase of the normal and continuum mode. As the integration length increases the difference in phase speed between the normal modes and the potential vorticity waves which interact with them is sufficient to allow a 'half-period' phase change to occur. The integration length required for this requirement to be met is inversely proportional to the wavenumber, therefore the smaller zonal scales will make the transition from the untilting to the modal masking regime at a shorter integration length than the larger scales. An interesting result of the scale selectivity of this transition is the fact that for models with very high resolution one would expect that the smallest scales will have entered the modal masking regime even at very short integration lengths, leading to singular vectors with the amplitude of the smallest scales concentrated at the steering level.

In Chapter 4 we examine the singular vector targeting method in the context of the Eady model singular vectors. By examining the 'sensitivity' as identified in the zonal-height plane we are able to make the following links between the singular vector dynamics and the sensitivity at different longitudes. During the untilting regime, there is only a single peak in sensitivity which corresponds to untilting perturbations on the central vertical levels of the model. Since the singular vectors amplify via untilting, the peak in sensitivity is associated with the most sensitive region for all zonal scales. As the integration length increases and the dominant growth mecha-

nism tends to modal unmasking, then the zonal location of sensitivity of smaller scales diverges from that of larger scales. The sensitivity to smaller scales occurs at two peaks 'near too' and 'far from' the verification region. These two peaks are associated with unmasking the normal modes on the lower and upper boundaries, respectively. The sensitivity at longitudes between these peaks is associated with the unmasking of the longer-wave normal modes and the untilting of shorter wavelengths. The association of different locations with different scales/growth mechanisms is of particular significance to singular vector targeting of this kind, as whilst the targeting method identifies target regions, it does not yield information on how to deploy observations in these regions. Knowledge of the perturbation scales and structures to which these 'sensitive regions' are sensitive may increase the ability to make informed choices about actual observational deployment, within the context of the established singular vector method.

In Chapter 5 we introduce a new singular vector targeting method. This targeting method differs from previous singular vector targeting methods, in that it utilises a dynamical estimate of the initial condition errors, rather than assuming that these errors are random with respect to a chosen inner product. It differs from the Ensemble Transform Kalman Filter (ETKF) in that it utilises singular vectors that are computed to only contain information dynamically relevant to the verification region, rather than a non-linear evolved ensemble, which potentially contains little information relevant to the verification region. Also unlike the ETKF, the validity of method also does not require the user to assume the presence of an operational Ensemble Kalman Filter, but rather allows the user to utilise any desired level of approximation to the operational data assimilation system in the estimate of the forecast error variance reduction. One further difference between the method and both the singular vector and ETKF methods, is that it explicitly predicts the reduction in forecast error variance as the difference between the forecast error variance with

and without the targeted observations. This additional feature introduces the potential for the prediction of instances where adding observations is likely to lead to an *increase* in the forecast error variance in the verification region.

The targets identified using the new targeting method in the Eady model with simplified data assimilation system are calculated. The target region is found to always reside somewhere within the sensitive region identified by the traditional singular vector methods, however the location of the best observation varies when the time-scale of dynamically evolved initial condition error estimate is varied. As with the 'traditional' singular vector targeting method discussed in Chapter 4, the changes in the optimal observation location are induced by the transition from the untilting to the modal unmasking regime. However unlike the traditional singular vector targeting method, in the new method the transition from the untilting to the modal unmasking regime occurs through evolution of the initial condition errors prior to the forecast initialisation time, rather than due an increase in the duration of the forecast. It is also found that the forecast error is more sensitive to corrections in initial condition errors that have evolved over a short time interval, than those which have not evolved or those which have evolved over a longer time interval. This result is based on the assumption that in each case the initial condition errors have the same average variance.

The work in this thesis has concentrated on the analysis of perturbation amplification and targeting observations within the context of the Eady model. Whilst the simplicity of the Eady model facilitates analysis, it is of interest to see how the results can be extended to more complex models. Of particular interest is the relationship between the two dynamical regimes of the Eady model singular vectors and the dynamical regimes identified in the ECMWF model singular vectors by Hoskins et al. (2000). A further consideration is the relationship between the targets identified using the Eady singular vectors and those computed using singular vectors obtained from a time

varying background state.

Another area in which this work could be extended is that of data assimilation. The targeting method defined in Chapter 5 utilises a linear transformation to approximate the effect of data assimilation on the initial condition errors. Whilst in principle this transformation could be highly representative of the data assimilation system, in our results we have reduced it to a simple local projection. One question that remains unanswered is, how similar does this transformation have to be to the operational data assimilation system for the targeting method to be successful, and furthermore how significant will the difference between the targets calculated with the new method be to those calculated using a Kalman filter based targeting method.

APPENDIX A

The Numerical Eady Model

A.1 Non-Dimensionalisation and Co-Ordinate Change

For the purpose of numerical accuracy, the Eady Equations outlined in Chapter 2 are non-dimensionalised. The zonal, vertical and temporal coordinates (x, z and t) are rescaled by divisors $L_R = N_0 Z/f_0$, Z and $N_0/f_0\Lambda$, respectively. A summary of the resultant rescaling applied to different variables is given in Table $A.1$. In non-dimensional form Eady Equations are

$$\frac{\partial \hat{q}'}{\partial \hat{t}} = -\hat{\bar{u}}_g \frac{\partial \hat{q}'}{\partial \hat{x}}, \quad \begin{cases} \hat{x} \in [0, \hat{X}] \\ \\ \hat{z} \in (0, \hat{Z}) \end{cases}, \tag{A.1}$$

$$\frac{\partial \hat{b}'}{\partial \hat{t}} = -\hat{\bar{u}}_g \frac{\partial \hat{b}'}{\partial \hat{x}} + \hat{v}', \quad \begin{cases} \hat{x} \in [0, \hat{X}] \\ \\ \hat{z} = 0, \hat{z} = \hat{Z} \end{cases}, \tag{A.2}$$

where

$$\hat{q}' = \frac{\partial^2 \hat{\psi}'}{\partial \hat{x}^2} + \frac{\partial^2 \hat{\psi}'}{\partial \hat{z}^2} \quad \begin{cases} \hat{x} \in [0, \hat{X}] \\ \\ \hat{z} \in (0, \hat{Z}) \end{cases}, \tag{A.3}$$

where

$$\hat{b}' = \frac{\partial \hat{\psi}'}{\partial \hat{z}} \tag{A.4}$$

and

$$\int_0^{\hat{X}} \hat{\psi}' d\hat{x} = 0, \;\; z \in [0, \hat{Z}], \tag{A.5}$$

where the hat denotes the non-dimensional variables. To minimise the variation in the magnitude of the mean zonal wind over the domain the zero point is moved to the centre of the domain. The mean zonal wind field may therefore be written

$$\hat{\bar{u}}_g = \hat{z} - \frac{\hat{Z}}{2}. \tag{A.6}$$

This change to the zonal wind is equivalent to placing the model in a frame of reference moving in the positive $\hat{x}$ direction with speed $\hat{Z}/2$; i.e.

$$\hat{x} = \hat{x}_0 + \frac{1}{2}\hat{t}, \tag{A.7}$$

where $\hat{x}_0$ the zonal coordinate at $t = 0$. The use of this moving coordinate frame acts only to translate evolving perturbations in the zonal direction by a factor $\hat{t}/2$ relative to the coordinate $\hat{x}_0$.

In the next section we shall discussion the descritisation of the Equations (A.1) to (A.5). The hats and dashes will be neglected and all quantities assumed to be in non-dimensional form.

A.2 The Discrete Equations and Numerical Model

For time integration of Equations (A.1) to (A.5) by a computer several processes are implemented at each discrete time-step. The exact numerical schemes used for these processes will be discussed in this section. Prior to this the nature and order of these processes will be summarised. Firstly

the potential vorticity, Equation (A.3) is inverted, subject to Equations (A.4) and (A.5), to obtain the stream-function field. Secondly the meridional perturbation velocity on the upper and lower boundaries is computed from the stream-function. Thirdly Equations (A.1) and (A.2) are solved to find the potential vorticity and upper and lower boundary buoyancy at the next time-step. In what follows the hats and dashes will be omitted from our notation; however all variables are identical to those used in Equations Equations (A.1) to (A.5).

The time dimension is discretised into intervals of length Δt. The spatial domain is discretised into an N_x by N_z grid with grid spacing Δx and Δz in the zonal and vertical directions respectively. The discrete and continuous spatial and time coordinates are related via

$$x = i\Delta x, \;\; i \in [1, 2, \ldots, N_x], \tag{A.8}$$

$$z = (j-1)\Delta z, \;\; j \in [1, 2, \ldots, N_z], \tag{A.9}$$

$$t = n\Delta t, \;\; n \in [1, 2, \ldots, \infty]. \tag{A.10}$$

Due to the periodic boundaries $N_x\Delta x$ is equivalent to both $x = X$ and $x = 0$.

In this discrete representation a five-point scheme is used to approximate the Poisson Equation (A.3) for potential vorticity. With this scheme the discrete potential vorticity is defined

$$q^n_{i,j} = \frac{\psi^n_{i+1,j} - 2\psi^n_{i,j} + \psi^n_{i-1,j}}{\Delta x^2} + \frac{\psi^n_{i,j+1} - 2\psi^n_{i,j} + \psi^n_{i,j-1}}{\Delta z^2}. \tag{A.11}$$

At the periodic boundaries the boundary conditions

$$\psi^n_{0,j} = \psi^n_{N_x,j} \tag{A.12}$$

and

$$\psi^n_{N_x+1,j} = \psi^n_{1,j} \tag{A.13}$$

are used. The derivative upper and lower boundary conditions are approximated using one-sided difference approximations. The discrete boundary conditions are defined as

$$b^n_{i,1} = \frac{\psi^n_{i,2} - \psi^n_{i,1}}{\Delta z}, \tag{A.14}$$

and

$$b^n_{i,N_z} = \frac{\psi^n_{i,N_z} - \psi^n_{i,N_z-1}}{\Delta z}, \tag{A.15}$$

on the top and bottom boundaries respectively. The use of a first order accurate one-sided difference scheme on the upper and lower boundaries rather than the second order accurate centred difference scheme is motivated by the fact that the use of a centred difference scheme on the boundary was found to lead to 'non-physical' singular vector structure. Tests of the accuracy of the streamfunction field obtained from the potential vorticity inversion scheme outlined above reveal that the accuracy is second order in the centre of the domain and first order at the upper and lower boundaries.

The Constraint Equation (A.5) is written for the discrete model as

$$\sum_{i=1}^{Nx} \left(\psi^n_{i,j}\right)^2 = 0, \;\; j \in [1, 2, \ldots, Nz]. \tag{A.16}$$

Equations (A.11) to (A.16) for a discrete elliptic integral problem, which can be solved to uniquely determine the stream-function field. Empirical convergence tests have shown that the solution to

this integral problem has first order accuracy on the upper and lower boundaries and second order accuracy in the central vertical level of the domain.

The time evolution of buoyancy and potential vorticity is computed by solving the discrete equations

$$\frac{q_{i,j}^{n+1} - q_{i,j}^{n-1}}{2\Delta t} = -\bar{u}_j \frac{q_{i+1,j}^{n} - q_{i-1}^{n}}{2\Delta x}, \;\; j \in [2, 3, \ldots, Nz-1]; \tag{A.17}$$

and

$$\frac{b_{i,j}^{n+1} - b_{i,j}^{n-1}}{2\Delta t} = -\bar{u}_j \frac{b_{i+1,j}^{n} - b_{i-1}^{n}}{2\Delta x} + v_{i,j}^{n}, \;\; j = 1, j = Nz; \tag{A.18}$$

for $q_{i,j}^{n+1}$ and $b_{i,j}^{n+1}$ respectively. In Equation (A.18) discrete meridional velocity $v_{i,j}^{n}$ is obtained from the stream-function field using

$$v_{i,j}^{n} = \frac{\psi_{i+1,j}^{n} - \psi_{i-1,j}^{n}}{2\Delta x}. \tag{A.19}$$

The Centred Time Centred Space advection scheme used in these equations gives second order accuracy in both space and time. This scheme remains numerically stable as long as the Courant number, $\bar{u}_j \Delta t / \Delta x$, remains strictly less than zero for all j. However, the scheme requires knowledge of the state at two time-points (n and $n-1$) in order to find the $n+1^{th}$ state. Since the initial condition gives the state at only one time-point, an initial forward time centred space step is taken for the initial time-step of the integration. This initial step is taken by solving the equations

$$\frac{q_{i,j}^{n+1} - q_{i,j}^{n}}{\Delta t} = -\bar{u}_j \frac{q_{i+1,j}^{n} - q_{i-1}^{n}}{2\Delta x}, \;\; j \in [2, 3, \ldots, Nz-1]; \tag{A.20}$$

and

$$\frac{b_{i,j}^{n+1} - b_{i,j}^{n}}{\Delta t} = -\bar{u}_j \frac{b_{i+1,j}^{n} - b_{i-1}^{n}}{2\Delta x} + v_{i,j}^{n}, \;\; j = 1, j = Nz, \tag{A.21}$$

for $q_{i,j}^{n+1}$ and $b_{i,j}^{n+1}$ respectively.

A.3 The Effect of Courant Number on the Accuracy of Solution

The Eady background state is characterised by a constant zonal wind speed that is a linearly increasing function of height. It is the rate of increase of the zonal wind-speed (relative to a fixed domain height) that determines the stability properties of the model. The stronger the wind-shear the greater the store of potential energy in the background flow and hence the greater the instability in the system. Due to errors in the phase speed errors inherent in the Centred Time Centred Space Advection scheme, the implied vertical profile of the of the mean zonal wind in the discrete Eady model differs from that specified in the continuous Eady model. In this section the nature of this discrepancy and its relationship with the Courant number will be discussed.

The dynamics in the interior of the model domain are governed by the conservative zonal advection of potential vorticity perturbations. On the upper and lower boundaries the zonal advection of potential temperature perturbations is augmented by the implicit meridional advection of potential temperature along the background meridional temperature gradient. In the continuous Eady Equations all potential vorticity anomalies travel with phase speed $\hat{\bar{u}}(\hat{z})$, which is a function of height only. However, in the numerical Eady model the phase speed is a function of both height and the anomaly's horizontal wave-number. The numerical phase speed of each wavenumber, $\hat{k}$,

is given by

$$\bar{u}_{num}(\hat{z},\hat{k}) = \frac{1}{\hat{k}\Delta t}\sin^{-1}\left[c(\hat{z})\sin\left(\hat{k}\Delta x\right)\right]; \tag{A.22}$$

where the Courant number, c, is defined

$$c(\hat{z}) = \hat{\bar{u}}(\hat{z})\frac{\Delta t}{\Delta x}. \tag{A.23}$$

It is clear from inspection of Equation (A.22) $c \to 1$ then $\bar{u}_{num} \to \Delta t/\Delta x$, which from Equation (A.23) implies that $\bar{u}_{num} \to \hat{\bar{u}}$; the numerical phase speed tends to that specified in the continuous equations. The exact phase speed however is unobtainable since for numerical stability the magnitude of Courant number is restricted to remain strictly less unity. However, for Courant numbers with magnitude close to one the numerical phase speed is a good approximation to the true phase speed at all wavenumbers. Seemingly keeping the Courant number close to one will minimise the effect of phase speed errors. In reality two problems with this idea occur. Firstly having high Courant number causes the magnitude of oscillations associated with the computational mode to be high and degrades the accuracy of the instantaneous solution. Secondly, since the phase speed $\bar{u}$ is a function of height the Courant number can not be uniform throughout the model domain. This lack of uniformity means that the accuracy of the solution varies with height.

Vertical variations in phase speed accuracy in the Eady model have important consequences for the vertically sheared wind field. The Eady model background state is characterised by a uniformly sheared wind field. In the non-dimensionalised equations, the magnitude of this shear is given by the non-dimensional wind-shear parameter $\hat{\Lambda} \equiv 1$. Differentiating the numerical phase

speed Equation (A.22) with respect to the height we obtain the numerical wind-shear parameter

$$\Lambda_{num}\left(\hat{z},\hat{k}\right) = \frac{\sin\left(\hat{k}\Delta x\right)}{\hat{k}\Delta x}\left\{1 - c^2(\hat{z})\sin^2\left(\hat{k}\Delta x\right)\right\}\hat{\Lambda}. \tag{A.24}$$

The Courant number varies linearly with height and its magnitude is bounded by the values on the upper and lower boundaries. If the magnitude of the Courant number ranges between values $\sim \pm 1$ then the numerical wind-shear parameter becomes a non-linear function of height, thereby contradicting the constant wind-shear assumed in the continuous Eady model. If however the Courant number remains bounded by values of magnitude much less than one, then the numerical phase speed may be written

$$\Lambda_{num} \approx \frac{\sin\left(\hat{k}\Delta\hat{x}\right)}{\hat{k}\Delta\hat{x}}\hat{\Lambda}, \tag{A.25}$$

and so depends on wave-number only. Since the wind-shear parameter no longer depends on height the properties of the zonal wind-field are consistent with the linearly increasing wind assumed in the continuous Eady Equations; albeit with each wavenumber experiencing a slightly different wind-shear.

Quantity	*Symbol*	*Factor*	*Value*
vertical coordinate	z	Z	$10^4 m$
zonal coordinate	x	$L_R = N_0 Z / f_0$	$10^6 m$
time	t	$N_0 / f_0 \Lambda$	$2.5 \times 10^4 s$
stream-function	ψ'	$L_R Z \Lambda$	$4 \times 10^7 m^2 s^{-1}$
horizontal velocity	$\bar{u}'_g, v'_g$	$Z\Lambda$	$40 m s^{-1}$
buoyancy	b'	$N_0 Z \Lambda$	$4 \times 10^{-1} m s^{-2}$
potential vorticity	q'	$f_0 \Lambda / N_0$	$4 \times 10^{-5} s^{-1}$

Table A.1 *Non Dimensionalisation factors.*

APPENDIX B

Orthogonality between plane-waves

In this appendix we shall derive the condition for orthogonality between plane-waves of the same zonal wavenumber. We shall start by defining two plane waves with the same zonal wavenumber k_n, but differing vertical wavenumbers m_1 and m_2. These two plane-waves are

$$\psi_1 = cos\left(k_n x + m_1 z\right), \tag{B.1}$$

$$\psi_2 = cos\left(k_n x + m_2 z\right), \tag{B.2}$$

where $m_1 \neq m_2$. Here it is worth reminding the reader that the tilt is related to the vertical wavenumber by $a = m/k$. The two plane-waves are orthogonal if the integral of their product over the domain is equal to zero; i.e.

$$\int_0^X \int_{z_1}^{z_2} \psi_1 \psi_2 dz dx = 0. \tag{B.3}$$

We shall start by rearranging the product

$$\psi_1 \psi_2 = cos\left(k_n x + m_1 z\right) cos\left(k_n x + m_2 z\right). \tag{B.4}$$

Using the trigonometric identity $cos(\theta)cos(\phi) = \frac{1}{2}(cos(\theta+\phi) + cos(\theta-\phi))$, we obtain

$$\psi_1 \psi_2 = \frac{1}{2}\left\{cos\left(2k_n x + [m_1 + m_2]z\right) + cos\left([m_1 - m_2]z\right)\right\}. \tag{B.5}$$

Using the further trigonometric identity $cos(\theta + \phi) = cos(\theta)cos(\phi) - sin(\theta)sin(\phi)$, we obtain

$$\psi_1\psi_2 = \frac{1}{2}\left\{cos\left(2k_n x\right) cos\left([m_1 + m_2]z\right) - sin\left(2k_n x\right) sin\left([m_1 + m_2]z\right) + cos\left([m_1 - m_2]z\right)\right\}. \tag{B.6}$$

Next we shall integrate the rearranged product with respect to x and z. Firstly we note that the integral with respect to x of the wave terms $cos(2K_n x)$ and $sin(2k_n x)$ will vanish, since we are integrating over whole periods of the wave. Integrating with respect to x and applying the limits we obtain

$$\int_0^X \int_{z_1}^{z_2} \psi_1\psi_2 dz dx = \int_{z_1}^{z_2} X cos\left([m_1 - m_2]z\right) dz. \tag{B.7}$$

Integrating with respect to z we obtain

$$\int_0^X \int_{z_1}^{z_2} \psi_1\psi_2 dz dx = \left[\frac{X}{m_1 - m_2} sin\left([m_1 - m_2]z\right)\right]_{z_1}^{z_2}. \tag{B.8}$$

From this expression, it is evident that ψ_1 and ψ_2 will be orthogonal if $sin\left([m_1 - m_2]z_1\right) = sin\left([m_1 - m_2]z_2\right)$. This will occur for arbitrary z_1 and z_2 only if

$$(m_1 - m_2)z_1 = (m_1 - m_2)z_2 \pm 2\phi\pi, \tag{B.9}$$

where $\phi \neq 0$ is an integer. Rearranging this condition and writing in terms of the tilt $a = m/k_n$, we arrive at the condition that is imposed on the tilt to guarantee orthogonality between the plane waves

$$\delta a = a_1 - a_2 = \frac{m_1 - m_2}{k_n} = \pm\frac{2\phi\pi}{k_n(z_2 - z_1)}. \tag{B.10}$$

APPENDIX C

The relationship between a simple data assimilation system and a local projection operator

The aim of this appendix is to show that, if we neglect vertical correlations in B and R and variations in B with zonal wavenumber and assuming the observations are colocated with model height levels, then we may write

$$FQ^T(R_p + Q_pF^TBFQ_p^T)^{-1}QF^T = FQ_p^TDQ_pF^T, \tag{C.1}$$

where D is a diagonal matrix.Each diagonal element in D corresponds to an observation location and is given

$$c(z) = \frac{r(z)}{r(z) + b(z)} \tag{C.2}$$

where $r(z)$ and $b(z)$ are diagonal elements of R and B respectively and z is the height of the observation.

To begin with we note that, in the absence of vertical correlations in R and B, G_p becomes block diagonal with each invertible block, $\tilde{G}_p$, corresponding to a single vertical level. For this reason we may treat each diagonal separately. If we assume that the observation error varies with height only, then for a single block

$$\tilde{R}(z) = r(z)I, \tag{C.3}$$

and likewise for B,

$$\tilde{B}(z) = b(z)I, \tag{C.4}$$

We can define the inverse equation for a single block

$$(\tilde{R}(z) + \tilde{Q}_p\tilde{F}^T\tilde{B}(z)\tilde{F}\tilde{Q}_p^T)^{-1} = (r(z)I + b(z)\tilde{Q}_p\tilde{F}^T\tilde{F}\tilde{Q}_p^T)^{-1}. \tag{C.5}$$

For simplicity we shall drop the subscript p for the rest of this appendix.

As in Bishop et al. (2001) we can make use of the fact that since it is symmetric, the eigenvectors of Q^TFF^TQ are form a complete orthonormal basis. We shall write the eigenvalue decomposition

$$\tilde{Q}F^TF\tilde{Q}^T = \Phi\Gamma\Phi^T \tag{C.6}$$

where Γ is diagonal and Φ is orthonormal. Since Φ is orthonormal, it satisfies $I = \Phi\Phi^T$, therefore we may write

$$(r(z)I + b(z)\tilde{Q}F^TF\tilde{Q}^T)^{-1} = (r(z)\Phi\Phi^T + b(z)\Phi\Gamma\Phi^T)^{-1} = \Phi(r(z)I + b(z)\Gamma)^{-1}\Phi^T. \tag{C.7}$$

We can also note that the eigenvectors and eigenvalues of $\tilde{Q}^T\tilde{F}\tilde{F}^T\tilde{Q}$ are the right singular vectors and singular values squared of $\tilde{F}^T\tilde{Q}$ respectively. Assuming may define the singular value decomposition of $\tilde{F}^T\tilde{Q}$ as

$$\tilde{F}\tilde{Q}^T = \Omega\Upsilon\Phi^T, \tag{C.8}$$

where Ω is a matrix containing the left singular vectors and Υ is a possibly non-square diagonal

matrix that satisfies $\Upsilon^T\Upsilon = \Gamma$. Using this singular value decomposition we may write

$$\tilde{F}\tilde{Q}^T\Phi(r(z)I + b(z)\Gamma)^{-1}\Phi^T\tilde{Q}\tilde{F}^T = \Omega\Upsilon\Phi^T\Phi(r(z)I + b(z)\Gamma)^{-1}\Phi^T\Phi\Upsilon^T\Omega^T, \tag{C.9}$$

and the fact that $\Phi^T\Phi = I$ we write

$$\tilde{F}\tilde{Q}^T\Phi(r(z)I + b(z)\Gamma)^{-1}\Phi^T\tilde{Q}\tilde{F}^T = \Omega\Upsilon(r(z)I + b(z)\Gamma)^{-1}\Upsilon^T\Omega^T. \tag{C.10}$$

Now we shall consider the form of $\Upsilon(r(z)I + b(z)\Gamma)^{-1}\Upsilon^T$. The matrix $(r(z)I + b(z)\Gamma)^{-1}$ is a diagonal matrix with the i^{th} diagonal element given by $1/(r(z) + b(z)(\Gamma)_{i,i})$. It is worth emphasising here that even if $(\Gamma)_{i,i}$ is zero, $1/(r(z) + b(z)(\Gamma)_{i,i})$ may not be. However, $(\Upsilon(r(z)I + b(z)\Gamma)^{-1}\Upsilon^T)_{i,i} = (\Gamma)_{i,i}/(r(z) + b(z)(\Gamma)_{i,i})$ and therefore *is* equal to zero if $(\Gamma)_{i,i} = 0$. Furthermore if all the non-zero elements of Γ have the same value γ, we may write

$$\tilde{F}\tilde{Q}^T\Phi(r(z)I + b(z)\Gamma)^{-1}\Phi^T\tilde{Q}\tilde{F}^T = c(\tilde{Q})\Omega\Upsilon\Upsilon^T\Omega^T, \tag{C.11}$$

where $c(\tilde{Q}) = \gamma/(r(z) + \gamma b(z))$ is a scalar that depends on depends observation distribution $\tilde{Q}$. Here it is worth noting that non-zero elements of Γ will only have the same value for specific choices of $\tilde{Q}$. We shall discuss these choices of $\tilde{Q}$ a little further on. First however we note that, from the definition of the singular value decomposition Equation (C.8)

$$c(\tilde{Q})\Omega\Upsilon\Upsilon^T\Omega^T = c(\tilde{Q})\tilde{F}\tilde{Q}^T\tilde{Q}\tilde{F}^T \equiv c(\tilde{Q})\tilde{T}_1(z), \tag{C.12}$$

where $\tilde{T}_1(z)$ is a diagonal block of the local projection operator T_1 corresponding to a single vertical level. For single a single observation on a vertical level and for an observation at every grid-point on that level Equation (C.11) and ,consequently, Equation (C.12) are found to be

generally true. This result was obtained empirically, by comparing the matrices eigen-spectra of $(R+\tilde{Q}\tilde{F}^T B\tilde{F}\tilde{Q})$ and $\tilde{T}_1$. This relationship was also found to hold exactly and approximately for many cases, but for concision further discussion will be neglected.

APPENDIX D

Mathematical Symbols

A^T : Transpose of general matrix A

A^{-1} : Inverse of general matrix A or A to the power -1

A^+ : Psuedo-inverse of general matrix A

$(A)_{i,j}$: i^{th}, j^{th} element of a general matrix A

$(\boldsymbol{b})_i$: element i^{th} of a general vector $\boldsymbol{b}$

A_i : The i^{th} matrix A

$\boldsymbol{b}_i$: The i^{th} vector $\boldsymbol{b}$

$\|\boldsymbol{b}\|_2 = \boldsymbol{b}^T\boldsymbol{b}$: Vector 2-norm of general vector $\boldsymbol{b}$

$\|\boldsymbol{b}\|_E = \boldsymbol{b}^T E\boldsymbol{b}$: Vector E-norm of general vector $\boldsymbol{b}$

I : Identity matrix

$\boldsymbol{u}$: Left singular vector

U : Matrix of left singular vectors

$\boldsymbol{v}$: Right singular vector

V : Matrix of right singular vectors

σ : Singular values

Σ : Matrix of singular values

$\mathscr{M}$: Non-linear numerical weather prediction model

M : Linear perturbation weather prediction model

$\boldsymbol{\chi}$: Weather forecast model state

$\boldsymbol{\delta\chi}$: Perturbation to weather forecast model state

$\mathscr{J}$: Data assimilation cost function

$\mathscr{H}$: Non-linear observation operator or foreward model

H : Linear observation operator or foreward model

R : Observation error covariance matrix

B : Background error covariance matrix

T : Local projection operator

E : E-Norm defining inner-product matrix

x : Zonal spatial coordinate

y : Meridional spatial coordinate

z : Vertical spatial coordinate

t : Time

$\boldsymbol{i}$: Zonally directed unit vector

$\boldsymbol{j}$: Meridionally directed unit vector

$\boldsymbol{k}$: Vertically directed unit vector

k : Zonal wavenumber

l : Meridional wavenumber

m : Vertical wavenumber

ψ : Quasi-geostrophic sreamfunction

q : Quasi-geostrophic potential vorticity

b : Scaled potential temperature perturbation (buoyancy)

u : Magnitude of zonal velocity

v : Magnitude of meridional velocity

w : Magnitude of vertical velocity

$\boldsymbol{u} = u\boldsymbol{i} + v\boldsymbol{j} + w\boldsymbol{k}$: Velocity

$\boldsymbol{v} = u\boldsymbol{i} + v\boldsymbol{j}$: Horizontal velocity

f : Coriolis parameter

N : Static stability parameter

Λ : Eady model wind-shear parameter

X : Zonal extent of model domain

Z : Height of model domain

Ro : Rossby number

Bibliography

Badger, J., and B. J. Hoskins, 2001: Simple Initial Value Problems and Mechanisms for Baroclinic Growth. *J. Atmos. Sci.*, **58**, 38–49.

Barkmeijer, J., M. Van Gijzen, and F. Bouttier, 1998: Singular vectors and estimates of the analysis-error covariance metric. *Quart. J. Roy. Meteor. Soc*, **124**(549), 1695–1713.

Bergot, T., 2001: Influence of the assimilation scheme on the efficiency of adaptive observations. *Quart. J. Roy. Meteor. Soc*, **127**, 635–660.

Bergot, T., G. Hello, A. Joly, and S. Malardel, May, 1999: Adaptive observations: a feasibility study. *Mon. Wea. Rev.*, **127**, 743–765.

Berliner, L. M., Z. Q. Lu, and C. Snyder, August, 1999: Statistical design for adaptive weather observations. *J. Atmos. Sci.*, **56**, 2536–2552.

Bishop, C. H., B. J. Etherton, and S. J. Majumbdar, March, 2001: Adaptive sampling with the ensemble transform kalman filter. Part I: theoretical aspects. *Mon. Wea. Rev.*, **129**(3), 420–436.

Bishop, C. H., and A. J. Thorpe, 1994: Potential vorticity and the electrostatics analogy: Quasi-geostrophic theory. *Quart. J. Roy. Meteor. Soc*, **120**, 713–731.

Bishop, C. H., and Z. Toth, June, 1999: Ensemble transformation and adaptive observations. *J. Atmos. Sci.*, **56**(11), 1748–1765.

Buizza, R., 1994: Localisation of optimal perturbations using a projection operator. *Quart. J. Roy. Meteor. Soc*, **120**, 1647–1682.

Buizza, R., 1997: *The singular vector approach to the analysis of perturbation growth in the atmosphere.* PhD thesis, University College London.

Buizza, R., and A. Montani, 1999: Targeting Observations Using Singular Vectors. *J. Atmos. Sci.*, **56**(17), 2965–2985.

Buizza, R., J. Tribbia, F. Molteni, and T. Palmer, 1993: Computation of optimal unstable structures for a numerical weather prediction model. *Tellus*, **45A**(5), 388–407.

Chang, E. K. M., December, 1992: Resonating neutral modes of the Eady Model. *J. Atmos. Sci.*, **49**(24), 2452–2463.

De Vries, H., and J. D. Opsteegh, 2005: Optimal perturbations in the eady model: resonance versus PV unshielding. *J. Atmos. Sci.*, **62**, 492–505.

Eady, E. T., 1949: Long Waves and Cyclone Waves. *Tellus*, **1**, 32–52.

Ehrendorfer, M., 2000: The total energy norm in a quasigeostrophic model. *J. Atmos. Sci.*, **57**, 3443–3451.

Emanuel, K., D. Raymond, A. Betts, L. Bosart, C. Bretherton, K. Droegemeier, B. Farrell, J. M. Fritsch, R. Houze, M. Lemone, D. Lilly, R. Rotunno, M. Shapiro, R. Smith, and A. Thorpe, 1995: Report on the first prospectus development team of the u.s. weather research-program to NOAA and the NSF. *Bull. Amer. Meteor. Soc.*, **76**(7), 1194–1208.

Errico, R. M., T. Vukicevic, and K. Raeder, 1993: Examination of the accuracy of a tangent linear model. *Tellus*, **45A**, 462–477.

Farrell, B., 1984: Modal and non-modal baroclinic waves. *J. Atmos. Sci.*, **41**(4), 668–673.

Farrell, B., 1989: Optimal excitation of baroclinic waves. *J. Atmos. Sci.*, **46**(9), 1193–1206.

Farrell, B. F., October, 1990: Small error dynamics and the predictability of atmospheric flows. *J. Atmos. Sci.*, **47**(20), 2409–2416.

Farrell, B.F., and P. J. Ioannou, 1996: Generalized stability theory. part I: Autonomous operators. *J. Atmos. Sci.*, **53**(14), 2025–2040.

Fischer, C., 1998: Linear amplification and error growth in the 2d eady problem with uniform potential vorticity. *J. Atmos. Sci.*, **55**, 3363–3380.

Frame, T., N. K. Nichols, and A. J. Thorpe, 2005: Structure and evolution of singular vectors in the Eady model. *Int. J. Numer. Meth. Fluids*, **47**, 1003–1009.

Gilmour, I., A. Leonard, and R. Buizza, 2001: Linear regime duration: Is 24 hours a long time in synoptic weather forecasting. *J. Atmos. Sci.*, **58**(22), 3525–3539.

Golub, G. H., and C. F. Van Loan, 1983: *Matrix Computations*. John Hopkins University Press.

Green, J. S. A., 1960: A problem in baroclinic stability. *Quart. J. Roy. Meteor. Soc*, **86**, 237–251.

Hamill, T. H., and C. Snyder, 2002: Using improved background-error covariances from an Ensemble Kalman Filter for adaptive observations. *Mon. Wea. Rev.*, **130**, 1552–1572.

Hamill, T. M., and C. Snyder, 2002: Analysis-error statistics of a quasigeostrophic model using three-dimensional variational assimilation. *Mon. Wea. Rev.*, **130**, 2777–2790.

Holton, J. R., 1992: *An introduction to dynamic meteorology*, third ed. Academic Press.

Hoskins, B. J., R. Buizza, and J. Badger, 2000: The nature of singular vector growth and structure. *Quart. J. Roy. Meteor. Soc*, **126**, 1565–1580.

Hoskins, B. J., M. E. Mcintyre, and A.W. Robertson, 1985: On the use and significance of isentropic potential vorticity maps. *Quart. J. Roy. Meteor. Soc*, **111**(470), 877–946.

Kim, Hyun Mee, and Michael C. Morgan, 2002: Dependence of sigular vector structure and evolution on the choice of norm. *J. Atmos. Sci.*, **59**, 3099–3116.

Kim, Hyun Mee, Michael C. Morgan, and Rebecca E. Morss, 2004: Evolution of analysis error and adjoint-based sensitivities: Implications for adaptive observations. *J. Atmos. Sci.*, **61**, 795–812.

Leutbecher, M., March, 2003: A reduced rank estimate of forecast error variance changes due to intermittent modifications of the observation network. *J. Atmos. Sci.*, **742**(5), 729.

Leutbecher, M., J. Barkmeijer, T. N. Palmer, and A. J. Thorpe, 2002: Potential improvement to forecasts of two severe storms using targeted observations. *Quart. J. Roy. Meteor. Soc*, **128**, 1641–1670.

LI, Zhi Jin, I. M. Navon, and M. Y. Hussaini, 2005: Analysis of the singular vectors of the full-physics florida state university global spectral model. *Tellus*, **57**(4), 560–574.

Lorenz, E. N., March, 1963: Determinisitc nonperiodic flow. *J. Atmos. Sci.*, **20**, 130–141.

Lorenz, E. N., 1965: A study of the predictability of a 28-variable atmospheric model. *Tellus*, **17**(3), 321–333.

Lorenz, E. N., and K. E. Emanuel, 1998: Optimal sites for supplementary observations: Simulations with a small model. *J. Atmos. Sci.*, **55**, 399–414.

Majumdar, S. J., C. H. Bishop, and B. J. Etherton, May, 2002: Adaptive sampling with the Ensemble Transform Kalman Filter. Part II field program implementation. *Mon. Wea. Rev.*, **130**, 1356–1369.

Majumdar, S. J., C. H. Bishop, B. J. Etherton, I. Szunyogh, and Z. Toth, October, 2001: Can an ensemble transform kalman filter predict the reduction in forecast-error variance produced by targeted observations? *Quart. J. Roy. Meteor. Soc*, **127**(578), 2803–2820.

Molteni, F., , R. Buizza, T. N. Palmer, and T. Petroliagis, 1996: The new ECMWF ensemble prediction system: methodology and validation. *Quart. J. Roy. Meteor. Soc*, **119**(47), 73–119.

Montani, A., 1998: *Targeting of observations to improve forecasts of cyclogenisis*. PhD thesis, Dept. of Meteorology, University of Reading.

Montani, A., and A. J. Thorpe, 2002: Mechanisms leading to singular-vector growth for FASTEX cyclones. *Quart. J. Roy. Meteor. Soc*, **128**(579), 131–148.

Morgan, M. C., September, 2001: A potential vorticity and wave activity diagnosis of optimal perturbation evolution. *J. Atmos. Sci.*, **58**, 2518–2544.

Morgan, M. C., and C. C. Chen, January, 2002: Diagnosis of optimal perturbation evolution in the eady model. *J. Atmos. Sci.*, **59**(2), 169–185.

Morss, R. E., K. A. Emanuel, and C. Snyder, January, 2001: Idealised adaptive observation strategies for improving numerical weather prediction. *J. Atmos. Sci.*, **58**, 210–232.

Mukougawa, H., and T. Ikeda, 1994: Optimal excitation of baroclinic waves in the eady model. *J. Meteor. Soc. Japan*, **72**(4), 499–513.

Orr, W. McF., 1907: Stability or instability of the steady-motions of a perfect liquid. *Proc. Roy. Irish Acad.*, **27**, 9–69.

Palmer, T. N., R. Gelaro, J. Barkmeijer, and R. Buizza, 1998: Singular Vectors, Metrics and Adaptive observations. *J. Atmos. Sci.*, **55**, 633–653.

Pedlosky, J., 1964: An initial value problem in the theory of baroclinic instability. *Tellus*, **16**(1), 12–17.

Pedlosky, J., 1979: *Geophysical fluid dynamics*, second ed. springer.

Pu, Z. X., E. Kalnay, J. Sela, and I. Szunyogh, 1997: Sensitivity of forecast errors to intial conditions with a quasi-inverse linear method. *Mon. Wea. Rev.*, **125**, 2479–2503.

Pu, Z. X., S. J. Lord, and E. Kalnay, 1998: Forecast sensitivity with dropwindsonde data and targeted observations. *Tellus*, **50A**, 391–410.

Rabier, F., and P. Courtier, 1992: Four-dimensional assimilation in the presence of baroclinic instability. *Quart. J. Roy. Meteor. Soc*, **118**, 649–672.

Snyder, C., T. M. Hamill, and S. B. Trier, 2003: Linear evolution of error covariances in a quasiqeostrophic model. *Mon. Wea. Rev.*, **131**, 189–205.

Strang, 1988: *Linear Algebra and its Applications*. Brooks, Cole.

Thompson, P. D., 1957: Uncertainty of initial state as a factor in the predictability of large scale atmospheric flow patterns. *Tellus*, **9**(3), 275–295.

Thorncroft, C. D., and B. J. Hoskins, October, 1990: Frontal cyclogenesis. *J. Atmos. Sci.*, **47**(19), 2317–2336.

Toth, Z, and E Kalnay, 1997: Ensemble forecasting at ncep and the breeding method. *Mon. Wea. Rev.*, **125**(12), 3297–3319.

Vukicevic, T, 1991: Non-linear and linear evolution of initial forecast errors. *Mon. Wea. Rev.*, **199**, 1602–1611.